Coherent Diffractive Imaging Near the Spatio-Temporal Limit with High-Harmonic Sources

by

Dennis Floyd Gardner Jr.

B.A., University of Colorado, 2010

M.S., University of Colorado, 2013

A thesis submitted to the

Faculty of the Graduate School of the

University of Colorado in partial fulfillment

of the requirements for the degree of

Doctor of Philosophy

Department of Physics

2017

This thesis entitled:
Coherent Diffractive Imaging Near the Spatio-Temporal Limit with High-Harmonic Sources
written by Dennis Floyd Gardner Jr.
has been approved for the Department of Physics

_____

Prof. Margaret M. Murnane

_____

Prof. Henry C. Kapteyn

Date _____

The final copy of this thesis has been examined by the signatories, and we find that both the
content and the form meet acceptable presentation standards of scholarly work in the above
mentioned discipline.

Gardner Jr., Dennis Floyd (Ph.D., Physics)

Coherent Diffractive Imaging Near the Spatio-Temporal Limit with High-Harmonic Sources

Thesis directed by Prof. Margaret M. Murnane and Prof. Henry C. Kapteyn

This thesis discusses methods for high-resolution static and stroboscopic microscopy using tabletop coherent extreme ultraviolet (EUV) radiation from tabletop high-harmonic generation (HHG) sources. These coherent short wavelength light sources are combined with a lensless, computational, phase and amplitude-contrast technique called ptychographic Coherent Diffractive Imaging (CDI). While ptychographic CDI techniques are currently widespread for visible, EUV and X-ray microscopy, no previous work has been able to achieve at-wavelength resolution of extended samples, especially in a reflection geometry, nor has previous work been able to image periodic samples with high-fidelity. In this work, a combination of experimental methods for high-numerical aperture imaging and novel computational algorithms enabled the highest resolution-to-wavelength demonstrations using any CDI technique. These algorithms include tilted plane correction, which enables high-resolution imaging of surfaces in a reflection geometry, and a powerful technique termed modulus enforced probe, which enables both imaging of periodic objects and convergence of the ptychographic CDI algorithm in fewer iterations. Furthermore, the ultrafast pulse duration of the high-harmonic radiation is harnessed to demonstrate proof-of-principle pump-probe imaging of nanostructures, capturing thermal transport processes in nanostructures with an axial resolution of 3 angstroms. Stroboscopic imaging with nanoscale resolution is a critical tool for the investigation of nanoscale heat flow and magnetic switching for the advancement of next generation nano-electronics, data storage, and nano-engineered systems.

Dedication

For my parents, Myriam and Dennis Gardner Sr.

For my partner, Corinne Beier.

Acknowledgements

Contents

Tables

Table

Figures

Figure

Chapter 1

Introduction

Understanding the structure and evolution of materials at greater spatial and temporal resolutions is central for discovery and innovation in science and technology, accelerating advances in materials and energy science, as well as nano-electronics and medicine. Many systems of interest have features on the order of nanometers (10^{-9} s) with dynamics occurring at picosecond (10^{-12} s) to femtosecond (10^{-15} s) time scales. For example, heat transport of closely packed nanoscale structures or the ultrafast switching of magnetic materials; both have important technologically impacts in current and next-generation nano-electronics devices and data storage systems.

A stroboscopic microscope using coherent extreme ultraviolet (EUV) radiation from high-harmonic generation sources is an ideal tool to investigate ultrafast nanoscale phenomena, because the short wavelengths allow nanoscale resolution and short pulses can capture the fastest dynamics.

Imaging with EUV has been challenging due to the lack of refractive-lenses and because most EUV optics are costly, imperfect, lossy, and cannot reach diffraction-limited spatial resolution. Fortunately, coherent diffractive imaging (CDI) has overcome this limitation by replacing image forming optics with computation. In CDI, the diffracted light from the sample is recorded, and using iterative phase retrieval algorithms, the diffracted light is back propagated to reconstruct a complex-valued image of the sample. The resolution in CDI is not limited by optics, instead it is only limited by the wavelength of illumination and the numerical aperture of the recorded diffraction pattern.

While CDI techniques are widely used for visible, EUV, and X-ray microscopy, no previous

work has been able to achieve at-wavelength resolution of extended samples, especially in a reflection geometry, nor has previous work been able to image periodic samples with high-fidelity. The ability to image in a reflection geometry is important for investigation of nano-patterned structures on substrates, substrates too thick for transmission imaging, and the ability to image periodic structures is especially important for industrial applications.

In this work, a combination of experimental methods for high-numerical aperture imaging and novel computational algorithms, enabled the highest resolution-to-wavelength demonstrations using any CDI technique in the EUV and x-ray spectral regions. These algorithms include tilted plane correction, which enables high-resolution imaging of surfaces in a reflection geometry, and a powerful technique termed modulus enforced probe, which enables quantitative imaging of periodic objects and convergence of the ptychographic algorithm in fewer iterations. In reflection, 40nm resolution was obtained with 30nm EUV, and in transmission, 12.6 nm resolution was obtained on a quasi-periodic sample using the technologically relevant wavelength of 13.5 nm.

Furthermore, the ultrafast pulses from high-harmonic generation were harnessed in the construction of a novel stroboscopic EUV microscope. Proof-of-principle pump-probe imaging of nanostructures is demonstrated, capturing thermal transport processes in nanostructures with an axial resolution of 3 angstroms.

This thesis is organized as follows. An overview of microscopy, with attention to nanoscale and dynamic imaging capabilities, is given in Ch. 2. Due to their short wavelengths, sources of extreme ultraviolet and x-rays are ideal for nanoscale imaging. The generation of EUV and x-rays is the subject of Ch. 3 with emphasis on coherent sources capable of producing ultrafast pulses. Following the overview on sources, Ch. 4 is devoted specifically to high-harmonic generation.

Given the lack of conventional refractive lenses, many techniques have been developed to image in the EUV and x-ray spectral regions and is the topic of Ch. 5. Chapter 6, is dedicated to coherent diffractive imaging, including ptychography.

The bulk of this thesis is contained in the following three chapters. In Ch. 7, methods, including tilted-plane correction, are discussed for reflection geometry CDI. The powerful modulus

enforced probe methodology, which enables both imaging of periodic objects and faster convergence of the ptychographic CDI algorithm, is presented in Ch. 8. And in Ch. 9, the ultrafast pulse durations of the high-harmonic source were harnessed to demonstrate proof-of-principle pump-probe imaging of nanostructures capturing thermal transport processes. This thesis concludes with a discussion of ongoing and future work in Ch. 10.

Chapter 2

A Tour of Microscopy

Since the first scientific publication using a microscope in 1665 by Robert Hooke [1], microscopy has led to many discoveries impacting just about every aspect of our lives.[1]   In 1873, Ernst Abbe, developed a criteria for the fundamental resolution limit of a microscope,

$$\Delta r \;=\; \frac{\lambda}{2n\sin\theta} \tag{2.1}$$

where Δr is the resolution, λ is the wavelength of light, n is the refractive index, and θ is the half-angle of the light collected by the imaging lens (see Fig. 2.1). The term $n\sin\theta$ is defined as the numerical aperture, NA, of the imaging system, allowing the fundamental resolution limit to be written as,

$$\Delta r \;=\; \frac{\lambda}{2\ NA}. \tag{2.2}$$

In modern microscopes, oil is used between the sample and the imaging lens to increase the NA by increasing the index of refraction n. Using oil immersion lenses the NA can be increased to values around 1.4, leading to resolutions around 180 nm using visible wavelengths (500 nm).

Many strategies have been developed to beat the diffraction limit, such as multiphoton excitation, near-field imaging, and super-resolution techniques. Multiphoton techniques use two, or more, IR photons to excite fluorescent molecules. Multiphoton microscopy can achieve higher resolution than the diffraction limit, around 100nm [4, 5], because only a localized spot within the focus of the illumination reaches sufficient intensity for the excitation of the dye molecules. The

---

[1] A review of visible microcopy is given in Ref. [2].
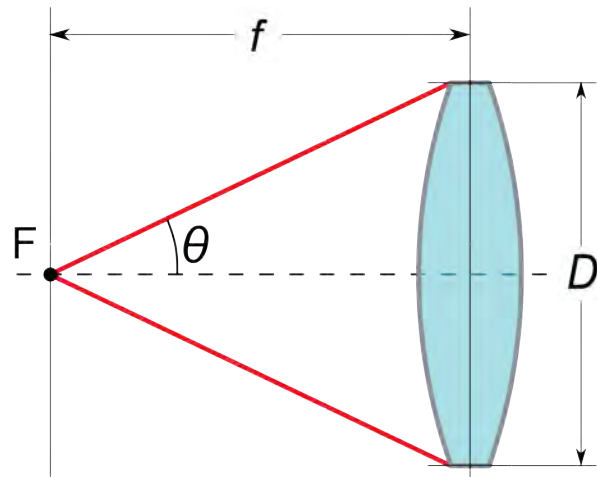
Figure 2.1: **Numerical Aperture** The diffraction limited resolution of an imaging system is dependent the numerical aperture (NA). The lens, shown in blue, is characterized by its pupil diameter, D, and its focal length f. Figure adapted from [3].

multiphoton approach, can also be applied without dyes, using a technique known as Coherent anti-Stokes Raman scattering (CARS) [6], in which the multiple photons map the sample's vibrational states. However, the improvements in resolution that multiphoton techniques achieved are not sufficient to resolve nanoscale structures.

Another strategy, Nearfield Scanning Optical Microscopy (NSOM) [7, 8], theoretically discussed in 1928 [9], and then experimentally demonstrated in the microwave region with resolution $60\times$ smaller than the illumination wavelength [10] in 1972. In NSOM, an aperture with a diameter smaller than the illuminating wavelength is brought near the sample and evanescent waves are recorded near the sample. The limit on resolution in no longer dependent on the wavelength of illumination, but instead is dependent on the size of the aperture, and demonstrations have achieved spatial resolution on the order of 10's of nm using optical wavelengths [11]. Furthermore, pulsed lasers have been applied to this technique for ultrafast temporal resolution on the order of 100's of femtoseconds [12].

The 2014 Noble prize in chemistry was awarded to pioneers of super-resolution techniques now widely used in biology [2]. These methods use fluorophores and are commonly referred to by their acronyms STED, PALM, and STORM. In Stimulated emission depletion (STED) microcopy, the emission area of the fluorescent spot is reduced by using doughnut beams created with diffractive optical elements [13, 14]. The doughnut beams are tuned to suppress emission of the dyes except for a nanometer sized volume at the center, which is stimulated with another laser.

Photoactivated localization microscopy (PALM) and stochastic optical reconstruction microscopy (STORM), use the stochastic blinking of the fluorophores [15, 16]. With sparse emitting fluorophores, computation models can pinpoint the location of the emitters with nanometer precision [17]. While the resolution of STED, PALM, and STORM are impressive, on the order of 10 nm, they are not suitable for ultrafast dynamic investigations because the excitation and emission of the dye molecules is on the order of nanoseconds, and is too slow to capture the picosecond to femtosecond dynamics of many scientifically relevant systems.

Instead of super resolution techniques with optical wavelengths to achieve nanometer reso-

lution, another strategy is to decrease the wavelength of illumination. Due to the wave-particle duality of nature, fast electrons can be described as waves given by de Broglie's equation [18]

$$\lambda \; = \; \frac{h}{p} \tag{2.3}$$

where λ is the wavelength, h is Plank's constant, and p is the momentum. The momentum is mass times velocity, with the velocity of electron's typically described by its kinetic energy in electron volts (eV). A modest energy for a modern electron source is 100keV, corresponding to an electron wavelength of approximately 3 picometers (pm), orders of magnitude smaller the visible light waves. Knoll and Ruska harnessed these short wavelengths and developed the first electron microscope in 1931 [19].[2] Theoretically, electron microscopes should have been able to obtain atomic resolution from their inception, but atomic resolution was not demonstrated for decades due to aberrations in electron lenses [22]. Currently, pulsed laser sources are being combined with electron sources to create ultrafast electron microscopes [23, 24]. It is a promising technique, but still has many challenges to overcome, such as space charge effects in the electron packets, which spread the pulse widths to about 100 femtoseconds [25].

Half of the 1986 Nobel Prize in physics went to Ruska for the invention of the electron microscope, the other half of the prize went to Rohrer and Binnig for point-scanning microscopy. In point-scanning microscopy, the resolution is not dependent on wavelength, but instead on the sharpness of a tip. The first demonstration is the scanning tunneling microscope in 1981 [26], followed by the atomic force microscope in 1986 [27]. In a scanning tunneling microscope, a charged tip is brought very near the surface such that electrons tunnel from the surface into the tip enabling atomic sensitivity. The atomic force microscope (AFM), is not quite as sensitive, but it is commonly used to profile nanoscale features with angstrom axial resolution [27]. In the AFM, a tip is mounted on the end of a cantilever and the cantilever is raster-scanned across the sample. If there are changes in sample height, the tip is attracted or repelled by atomic forces and deflections of the cantilevers are monitored to from a detailed profile of the surface. These point scanning methods

---

[2] A history of electron microscopy is given in Refs. [20, 21].

are powerful nanoscale techniques, and have been combined with pulsed optical lasers for dynamic experiments [28, 29].

Complementary to the techniques described previously, coherent extreme ultraviolet (EUV) and x-rays are well suited for nanoscale imaging because of their short wavelengths. The wavelengths of EUV range from 100 nm to 10 nm, and x-rays range from 10 nm to 0.01 nm (see Fig. 2.2). As the Abbe resolution criterion scales with wavelength, Eq. 2.1, these sources are theoretically capable of achieving nanometer scale resolution, without any super resolution techniques. Furthermore, depending on the source, coherent EUV and x-rays are capable of capturing the fastest of dynamics with pulses in the picosecond, femtosecond, or even attosecond regime [30]. The generation of coherent EUV and x-rays is the topic of the next chapter.
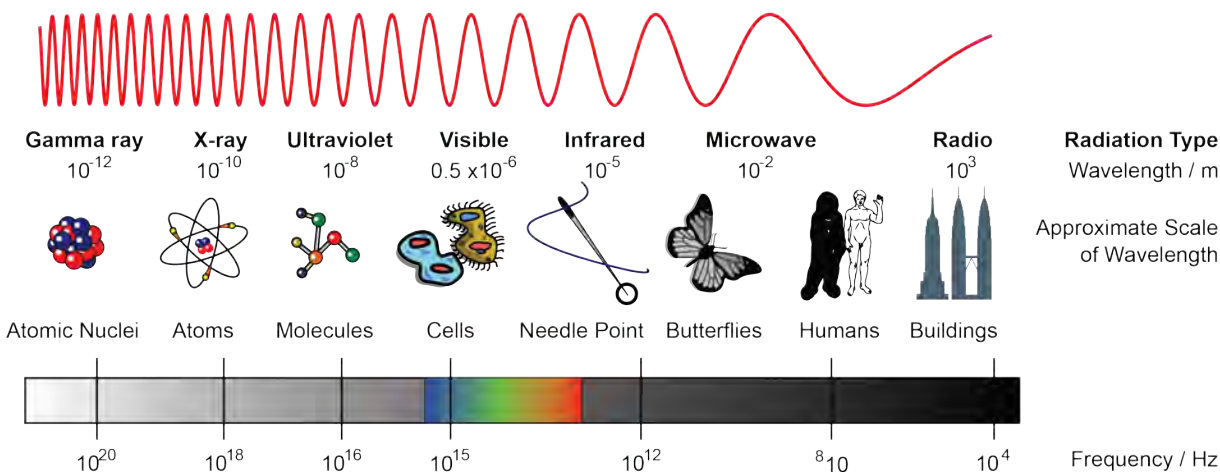
Figure 2.2: **Electromagnetic Spectrum** Most microscopes today employ wavelengths in the visible region of the spectrum. The microscopes developed during this thesis use extreme ultraviolet radiation, which lies between the ultraviolet and x-ray regions, for high resolution microscopy. Figure adapted from [31].

Chapter 3

Coherent Sources of EUV and X-rays

Sources of coherent EUV and x-rays can be divided into two categories: large and small scale sources. Large scale sources harness the radiation emitted by relativistic electrons and require a large accelerator facility. Small scale sources, on the other hand, do not require particle accelerators, drastically reducing their cost and size.

3.1   Large Scale Facilities

Large scale facilities can be further divided into synchrotrons and free-electron lasers (FEL). In both facilities electrons are accelerated with radio waves to nearly the speed of light. Electrons are used, instead of protons, because their lighter mass allows for greater speeds given the same energy input. As discussed below, the faster the electrons, the harder and brighter the source.

3.1.1   Synchrotrons

In a synchrotron, relativistic electrons are kept on a closed path using bending magnetics with a burst of radiation produced at each bending magnet. First generation synchrotrons operated parasitically off pre-existing electron storage rings used for particle physics. Second generation facilities were built as dedicated facilities for EUV and x-ray experiments with bending magnetics all around the facility. These facilities were optimized to keep the electrons circulating for 5-100 hours, allowing time for measurements [32]. Modern third generation synchrotrons employ additional magnets, wigglers and undulators, to generate harder and brighter radiation. [33]
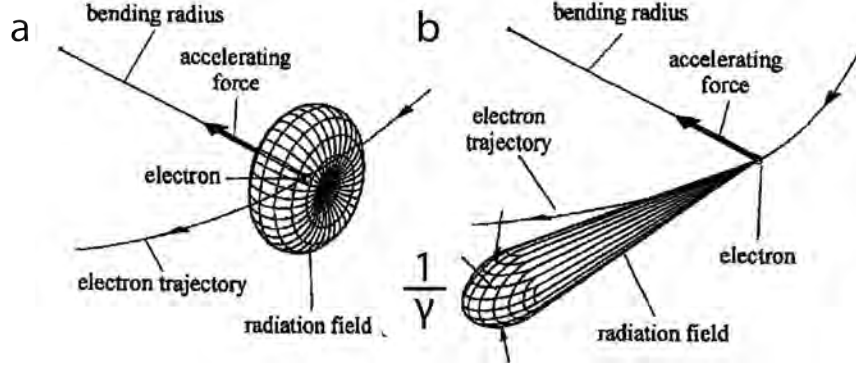
Figure 3.1: **Radiation from a Relativistic Electron** a) Slow moving electrons produce dipole-like radiation patterns. b) In the laboratory frame, electrons traveling at relativistic speeds emit radiation in a narrow, 'searchlight' type pattern. Figure adapted from Ref. [36].

When the velocity of a charged particle is small compared to the speed of light, the power radiated per unit solid angle has the characteristic $\sin^2(\theta)$ dependence given by

$$\frac{dP}{d\Omega} = \frac{e^2}{4\pi c^3} a^2 \sin^2(\theta),$$ (3.1)

where e is the electron charge, c is the speed of light, a is the acceleration, and θ is the angle between the acceleration and the velocity. This dipole-like radiation is shown in Fig. 3.1a. When the velocity of the electron approaches the speed-of-light, the radiation pattern is altered due to relativistic effects. The dipole-like radiation, Eq. 3.1, can be generalized for arbitrary velocities using the appropriate Lorentz transformations [34]. When generalized and adapted for acceleration perpendicular to the electron's velocity the radiation distribution is given by,

$$\frac{dP}{d\Omega} = \frac{e^2}{4\pi c^3} \frac{a^2}{(1 - \beta cos(\theta))^3} [\ 1 - \frac{sin^2(\theta)cos^2(\phi)}{\gamma^2(1 - \beta cos(\theta))^2}]$$ (3.2)

where $\beta \equiv v/c$ and $\gamma \equiv \sqrt{1 - \beta^2}$ [34, 35]. This radiation is sharply peaked in the forward direction and the divergence angle is approximately $1/\gamma$ as illustrated in Fig. 3.1b.

The synchrotron source is not continuous, instead the electrons are bunched into packets at the nodes of the accelerating radio-frequency field. For example, at the Advanced Light source in Berkeley, the electron pack is about 35 ps and circulates at 55 MHz [37]. To achieve shorter electron pulses, ultrafast optical lasers have been used to modulate the energy of a small slice of

the electron packet [38]. The modulated electrons can then be spatially separated using bending magnetics and apertures, resulting in pulse widths of 100's of femtoseconds [39].

3.1.2   X-ray Free-Electron Lasers

In most laser gain media, the electrons are bound to atoms or molecules which limits typical gain media to the infrared, visible, and ultraviolet regions of the electromagnetic spectrum (Fig. 2.2). The Free-Electron Laser (FEL) is unlike typical gain media because the electrons are unbounded allowing great tunability from microwave to x-ray wavelengths. In a FEL, relativistic electrons are passed through a series of magnetics, an undulator (see Fig. 3.2), which cause the electrons to oscillate because of the Lorentz force. The oscillating relativistic electrons can emit microwave to x-ray radiation. [1]

The first theoretical consideration of radiation from relativistic electrons in a oscillating magnetic field was done my H. Motz in 1951 [47]. Shortly after this theoretical prediction, in 1953, the first demonstration of radiation from an undulator was demonstrated [48]. However, this demonstration emitted incoherent light and thus could not be called a laser (it was also before the invention of the laser so the term "laser" would not have been used anyway). The modern idea of a FEL, as well as the term FEL, first appeared in a theoretical paper in 1971 by J.M.J. Madey [49]. J.M.J. Madey et *al.* realized the first observation of gain with an undulator structure in 1976 and then the first FEL in 1977 [50, 51].

The key to producing short wavelengths is electrons traveling at nearly the speed of light. When relativistic electrons pass through the undulator with a period of λ_u, the electrons "see a Lorentz contracted undulator period $\lambda'_u = \lambda_u/\gamma$, where γ is the relativistic factor given by

$$\gamma = \frac{1}{\sqrt{1 - v^2/c^2}} \tag{3.3}$$

with v the velocity of the electrons in the lab frame and c the speed of light. The prime designates a frame moving with the electrons. The Lorentz contraction is just one effect from the relativistic

---

[1] For further Refs. see [40–46]

speeds, another is the Doppler shift. In the lab frame, the light is blue shifted

$$\omega = \gamma\omega'(1 + v/c) \tag{3.4}$$

where ω is the angular frequency in the lab frame. At this point a calculation can show, to first order, how short wavelengths of light can be generated from FELs. To begin, the undulator period in the electrons frame is converted into angular frequency.

$$\omega' = 2\pi\frac{c}{\lambda'_u} \tag{3.5}$$

From here the Lorentz contracted undulator period, λ'_u, is transformed into the lab frame, λ_u.

$$\omega' = 2\pi\frac{c\gamma}{\lambda_u} \tag{3.6}$$

The angular frequency of radiation in the lab frame is given by,

$$\omega = 2\pi\frac{c\gamma^2}{\lambda'_u}(1 + v/c). \tag{3.7}$$

Changing the angular frequency to wavelength leads to,

$$\lambda_l = \frac{\lambda_u}{\gamma^2(1 + v/c)}, \tag{3.8}$$

where λ_l is the wavelength of emitted radiation as seen in the lab frame. Approximating $v/c \approx 1$ because the electrons travel at nearly the speed of light results in

$$\lambda_l = \frac{\lambda_u}{2\gamma^2}. \tag{3.9}$$

a first order approximation of the wavelength emitted by an FEL. Plugging in modest parameters for the LCLS facility in California, with as an undulator period of 3cm and a γ of 7800, the FEL can produce 2.5 Å radiation [52].

3.2   Tabletop Sources

The large scale sources are impressive facilities but they are very expensive (100's of millions USD) and are limited to a few users at a time. Tabletop sources can complement large scale facilitates because they are much smaller and cheaper ($\approx$ 100-1000k USD) allowing table top sources to be more available to university and industry laboratories.
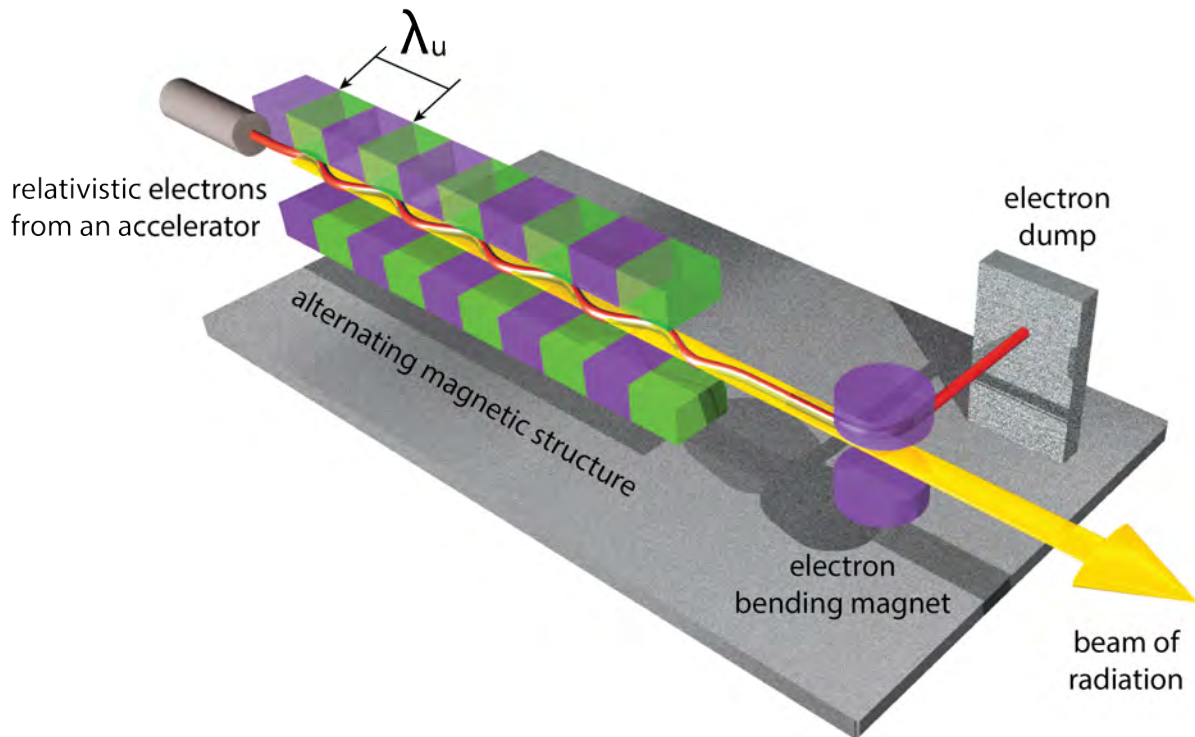
Figure 3.2: **Free-Electron Laser** Relativistic electrons are passed through an area of alternating magnetic fields. The magnetic fields cause the electrons to wiggle and as they wiggle they emit radiation. The electrons are removed from the beam of radiation using a bending magnetic. Figure adapted from Ref. [53].

3.2.1   EUV Lasers

The principle behind EUV lasers, just like optical lasers, is stimulated emission between atomic levels. The first demonstration of EUV lasing, performed at the large-scale Novette laser facility at Lawrence Livermore National Lab, used the transition between $2p^53p$ and $2p^53s$ in neon-like selenium [54]. Using a high-powered optical laser at 532 nm with $5 \times 10^{13}W//cm^2$, the target is ionized by a line focus. Some of the emission from the excited selenium target travels along the long-axis of the plasma created by the line focus. The spontaneous emission simulates more emission as is propagates along the plasma creating Amplified Stimulated Emission (ASE). In a typical optical laser, the ASE will pass through the gain medium several times in a cavity configuration resulting in large gains and high-coherence. However, due to the short lifetimes of the excited states required for EUV lasing, multiple passes is not possible. Instead, EUV lasers use a single or double pass, thus resulting in lower coherence than cavity type lasers [55].

It was almost a decade until the first demonstration of tabletop EUV lasing because of the unfavorable pump density scaling. It takes a lot of pumping to create the exited states for EUV lasing with the pump density, P, scaling as $P \propto \frac{1}{\lambda^5}$. The first tabletop demonstration did not use optical pumping, but instead an electrical discharge of 40kA in Argon gas [56]. Work has continued to make the tabletop sources smaller and with faster repetition rates [57]. And today, even with the unfavorable scaling, wavelengths as short as 8nm have been demonstrated using optical lasers as the pump with picosecond pulse durations [58].

3.2.2   High-Harmonic Generation

The high-harmonic generation (HHG) process is a highly non-linear up-conversion of an intense driving laser. The first HHG demonstration, in 1983, focused a 248.4 nm laser into helium and observed the 7th harmonic at 35.5 nm [59]. The extension to ever higher harmonics, using driving lasers with intensity's of $10^{15} - 10^{16}$ W/cm^2, witnessed the 17th harmonic in Ne, again with a 248.4nm laser [60]. After the experimental demonstration, theory papers discussed the scaling of

HHG [61, 62], with the maximum energy from HHG given by

$$h\nu_{cutoff} = I_p + 3.17U_p \tag{3.10}$$

where h is Planks constant, ν is the frequency, I_p is the ionization potential of the atom, and Up is ponderomotive energy [62, 63]. The ponderomotive energy is the mean kinetic energy gained by the free electron in the laser field and is proportional to $U_p \propto I_L \lambda_L^2$ where I_L and λ_L are the intensity and wavelength of the driving laser. As the harmonic cutoff suggests, higher energy photons are generated with longer wavelength driving lasers because the longer the driving laser wavelength, the longer the electron is accelerated in the laser field. The push toward bright keV photons is a current area of research [63, 64]. The work here used high-harmonics from an ultrafast Ti:Sapphire laser. Further details on high-harmonic generation are discussed in Ch. 4.

Chapter 4

High-Harmonic Generation

Most of the work in this thesis was demonstrated with EUV light from a high-harmonic source, with one exception of a benchtop HeNe laser prototype. High-harmonic generation (HHG) is a highly-nonlinear process in which intense, ultrafast, laser pulses are up converted into the EUV and the soft-x-ray spectral regions [63, 64].

4.1   Driving Laser

The driving laser for the HHG in this work uses a titanium doped sapphire crystal. In the early 1990s, the broad bandwidth of Ti:Sapphire was harnessed in a mode-locked ultrafast laser [65]. The mode-locking in this laser uses the Kerr effect: a change in the refractive index due to intense radiation. The laser cavity can be designed to use the Kerr effect, and when aligned properly, the cavity gain favors pulsed operation instead of a continuous wave. An example of the cavity of a mode-locked laser, called an oscillator, is shown in Fig. 4.1.

The first demonstration had 60 fs pulses and subsequent work, reducing the cavity dispersion with prisms, reduced the pulse length to 10 fs [67]. While the pulse length of the mode-locked Ti:Sapphire is fast, the intensity of the pulse is not sufficient for high-harmonic generation. To increase the intensity, the pulse must be amplified, but care must be taken because intense femtosecond pulses can burn optics or create non-linear effects in the cavity and thereby limiting the gain.

To amplify the short pulses by many orders of magnitude, chirped pulse amplification (CPA)
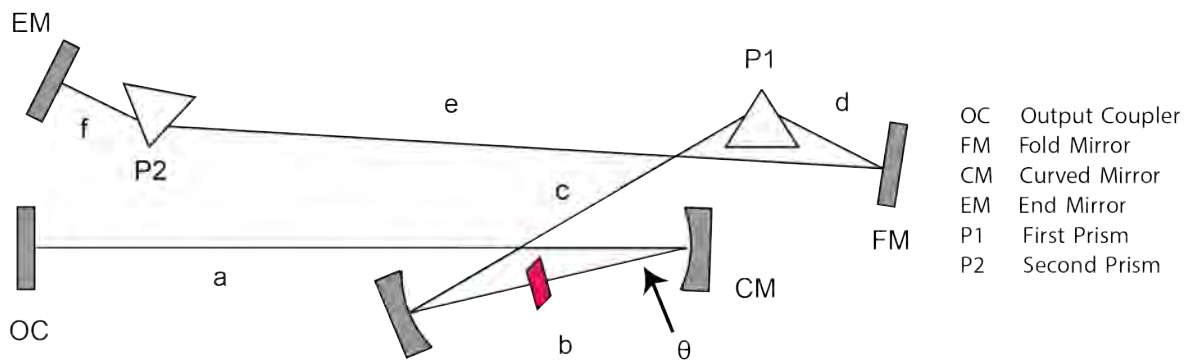
Figure 4.1: **Mode-locked laser cavity alignment** This work used a mode-locked Ti:Sapphire laser to seed an amplifier. The distances are as follows: a $\sim$ 62 cm, b $\sim$ 10.4 cm, θ $\sim$ 16°, c $\sim$ 22 cm, with the total prism separation (d+e) $\sim$ 62 cm, and f $\sim$ 5 cm. Figure adapted from Lytle Ref. [66].
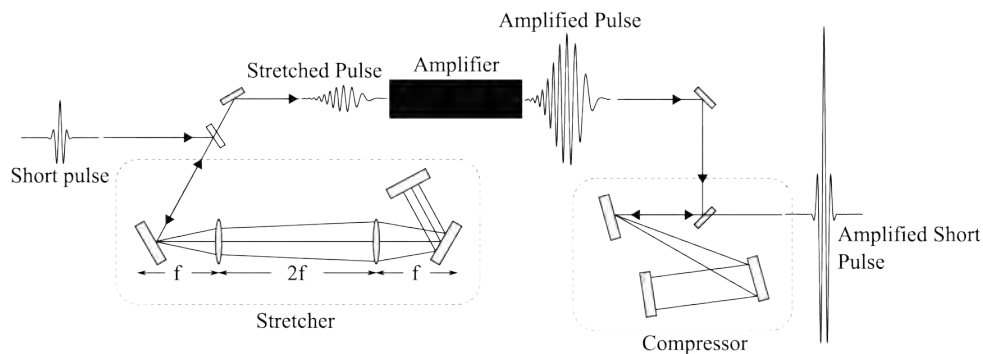
Figure 4.2: **Chirped Pulsed Amplification** Using chirped pulsed amplification, the seed pulse from the oscillator, Fig. 4.1, is amplified to drive the high-harmonic generation process. Figure adapted from Seaberg and Backus et al. Ref. [72, 74].

is used [68,69]. In CPA, the pulse is first stretched out in time using a grating system configured for positive dispersion. Stretching the pulse to a 100 ps or more allows for relatively safe amplification, as long as the optics are clean and have high-damage threshold coatings. In the laser system used in this work, a KM Labs Dragon, the Ti:Sapphire crystal in the amplifier cavity is pumped with a 532 nm, frequency-doubled Nd:YAG, laser at 3-5kHz. The pumping laser (Lee Laser LDP-200MQG-HP) can have an output as high as 100 W. This much power cannot normally be used to pump because thermal lensing effects. However, this laser used cryogenic-cooling to reduce the thermal lensing by two orders of magnitude [70]. After 12-13 passes through the amplifying crystal, the pulse is recompressed [71] to a 21-24 fs pulses [72, 73]. After the amplifier, the output at 3kHz has about 3 mJ per pulse and is sufficient for high-harmonic generation. A schematic of the amplifier is shown in Fig. 4.2.

4.2 HHG - The Microscopic Picture

In typical non-linear processes, like second harmonic generation, a driving laser field passes through a material and the electrons are driven hard enough such that the harmonic-oscillator potential is distorted and the material emits radiation at higher frequencies above the fundamental.

Taking this process to the extreme results in HHG [75].

For the HHG process to occur, the laser field needs to be intense, $10^{13} - 10^{16}$ W/cm^2 such that the electron is ionized. While HHG has been demonstrated with solid [76] and plasma targets [77], we restrict our discussion here to HHG in a dilute gas [78].

In a semi-classical approximation (see Fig. 4.3), when the electron is tunnel ionized from its parent atom, it is assumed to be in vacuum at zero velocity. However, the instant the electron is freed it is accelerated by the inhomogeneous electromagnetic field through the ponderomotive force. When the oscillating laser field switches directions, and if the electron recombines with its parent atom, the energy gained by the electron is released as a high energy photon. The maximum energy that can be released is given by

$$E_{cutoff} = I_p + 3.2U_p \tag{4.1}$$

where I_p is the ionization potential of the atom and U_p is the ponderomotive energy given by

$$U_p = \frac{e^2 E^2}{4m\omega^2} \propto I\lambda^2 \tag{4.2}$$

where e and m are the electron's charge and mass, E, ω, I, and λ are the laser fields amplitude, angular frequency, intensity and wavelength.

To extend the cutoff energy, Eq. 4.1, higher energy radiation can be produced from longer wavelength driving lasers. The use of infrared driving lasers has generated photon energies in the water window [79] and beyond, up to 1.4 keV energies corresponding to wavelengths shorter than a nanometer [63]. Such high energies are the result of over 5000 infrared photons combining to produce a single soft-x-ray photon.

4.3   HHG - The Macroscopic Picture

For a bright source of high-harmonic radiation, the high-energy photons emitted by individual atoms need to constructively interfere. Constructive interference occurs when the phase velocity of the driving laser, ν_ω, matches the phase velocity of the high-harmonic radiation, $\nu_{q\omega}$, where q is
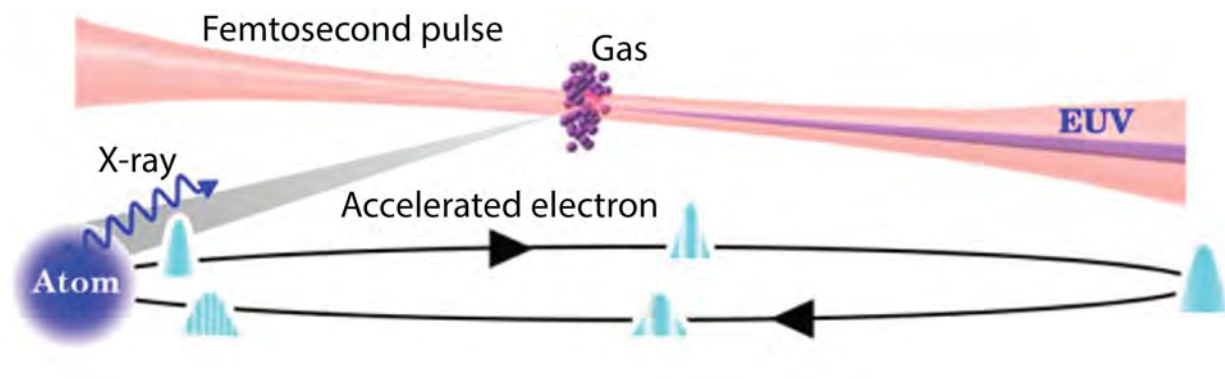
Figure 4.3: **HHG - The Microscopic Picture** An intense, ultrafast, laser is focused into a dilute gas. The laser field tunnel ionizes an electron and the freed electron is first accelerated away from its parent atom before the oscillating laser field switches direction. Then the electron is driven back to its parent atom where it recombines and releases its energy in a high energy photon. The blue curves depict the wave packet evolution of the free electron along a classical trajectory. Figure adapted from Ref. [75].

the harmonic order and ω is the fundamental angular frequency. For phase matching to occur, the difference in wavenumbers, $k = \omega/\nu_p$, between fundamental driving laser, k_ω, and the high-harmonic, $k_{q\omega}$, must be zero.

$$\Delta k = k_{q\omega} - qk_\omega = 0 \tag{4.3}$$

Coherent buildup of HHG in a dilute gas can be accomplished in a waveguide (see Fig. 4.4) [80–83]. In the waveguide, the dispersion can be described by three terms [84]: dispersion from the geometry, plasma, and free-electrons. The mismatch in dispersion is given by

$$\Delta k \approx \underbrace{q\frac{\mu_{11}^2\lambda_L}{4\pi a^2}}_{\text{geometric}} \underbrace{- qp(1-\eta)\frac{2\pi}{\lambda_L}(\Delta\delta + n_2)}_{\text{atoms}} + \underbrace{qp\eta N_a r_e \lambda_L}_{\text{free-electrons}} \tag{4.4}$$

where μ_{11} is the mode factor, a is the waveguide radius, η is the ionization level, r_e is the classical electron radius, N_a is the number density of atoms/atm, $\Delta\delta$ is the difference in the indices of refraction of the gas at the fundamental and x-ray wavelength, ω and λ_L are the fundamental laser frequency and wavelength, n_2 is the nonlinear index of refraction at λ_L for the given intensity $(n_2 = \tilde{n}_2 I_L)$, I_L, of the driving laser, and p is the pressure.

The sign of dispersion is positive for the geometrical and free-electrons, but negative for the neutral atoms. Furthermore, the dispersion terms for the neutral atoms and free-electrons are pressure dependent. By tuning the pressure in the waveguide, a balance of the dispersion terms is possible resulting in a bright and coherent buildup of high-harmonic radiation. Typical conversion efficiencies for HHG in a waveguide are on the order of 10^{-6} [66] and results in $> 10^9$ photons/sec/1% bandwidth [85].

4.4   Temporal Characteristics

As mentioned above, intense, ultrafast, laser fields are needed to generate high-harmonic radiation. The ionization and recombination of the electrons occurs within the temporal envelope of a single laser pulse, thus the high-harmonic radiation is also an ultrafast pulse. Typically, the pulse width of the harmonic generation is given by $\tau/\sqrt{2}$, where τ is the driving laser pulse width
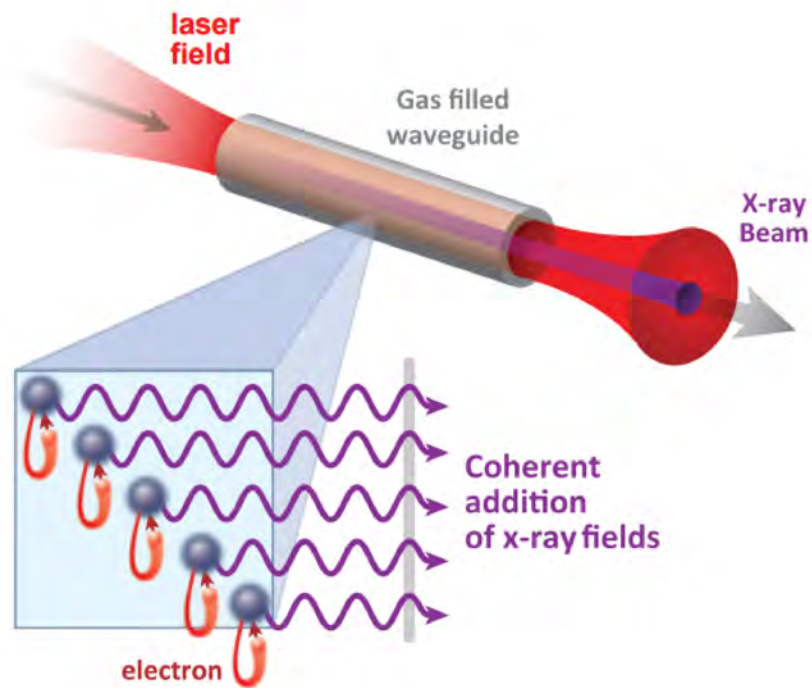
Figure 4.4: **HHG - The Macroscopic Picture** An intense, ultrafast, laser is focused into waveguide. The gas pressure in the waveguide is tuned achieve phase matching. This results in a coherent addition of the high-harmonic radiation. Figure courtesy of KM group (https://jila.colorado.edu/kmgroup/research/articles/attosecond-nonlinear-optics).

and q is the harmonic order [86].

There are a couple of methods to generate high-harmonics such that the bust of radiation occurs on attosecond (as) time scales.[1]   One method uses polarization gating, such that the driving laser has a phase locked polarization modulation which only permits the generation of high-harmonics within a single-cycle resulting in 130 as pulses [87]. In an alternative method, the intensity of the laser can be tuned, such that the generation of high-harmonics is achieved only during the most intense single-cycle of the driving laser [88]. Using mid-IR driving lasers, soft-x-ray bursts of high-harmonics have been demonstrated [89]. The combination of short wavelength radiation, ultrafast bursts, an inherently synchronized pulses with the driving laser, makes HHG the ideal source for imaging at the spatiotemporal limit using pump-probe methodologies. Next, imaging forming methods with EUV and x-rays are discussed.

---

[1] A review on attosecond pulse generation [30].

Chapter 5

Imaging Forming Methods with EUV and X-rays

Probably the simplest method to form an image with EUV and x-rays is to record the shadow of the object, as done in medical x-ray imaging (radiography). Radiography provides information about the distribution of absorbing materials with resolution on the order of millimeters. The sensitivity of radiography can be improved with phase enhancement approaches [90], but the resolution is not improved because no images are formed. The ability to from images in the EUV/x-ray region is not as straightforward as imaging with optical wavelength because of the lack of suitable refractive lens elements, with one exception: the compound refractive lens [91–93].

Recently, compound refractive lens elements have been developed to focus x-ray radiation to about 100 nm spot sizes [94]. A series of cylindrical or parabolic holes in low-z materials such as beryllium, act as lenses in the hard x-ray regime (see Fig. 5.1). The focal length, F, of these lenses is given by

$$F = \frac{R}{2N\delta} \tag{5.1}$$

where R is the radius of the hole in the material, N is the number of holes, and δ is the decrement of the refractive index n ($n = 1 - \delta$). For now, compound lenses are suitable for hard-rays, because as of yet, no suitable material has been found to work in the EUV spectral region.

A couple of methods to improve the resolution of x-ray imaging, without lenses (compound or otherwise), use small apertures. In the first method, the aperture is placed directly in front of the sample and is then raster scanned. The transmitted light at each position is summed on a detector, thus forming an image of the sample with the resolution dependent on the size of the
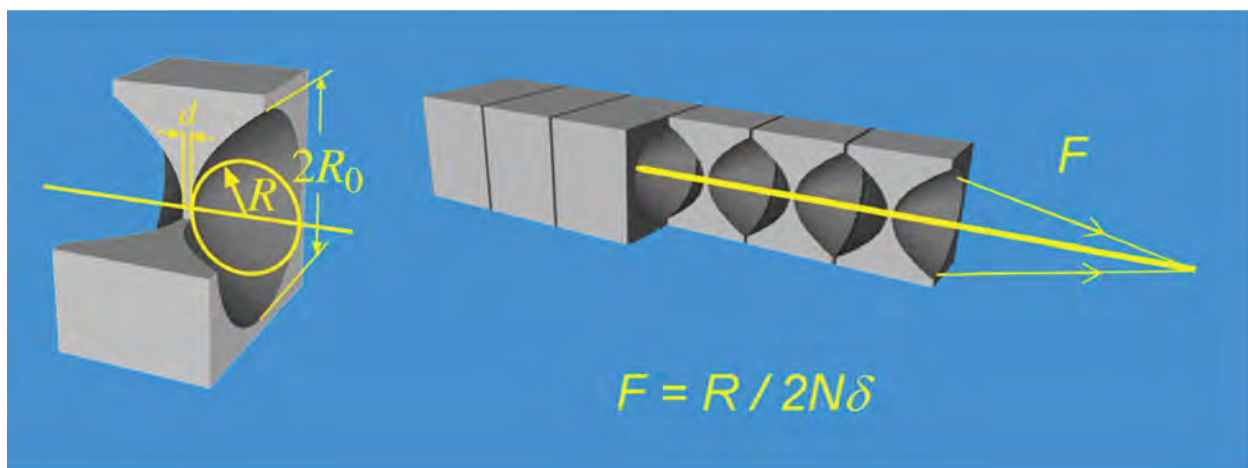
Figure 5.1: **Compound Refractive Lens** The compound lens consists of holes fabricated into a low-z material. Depicted here is the focal length of the compound refractive lens given in Eq. 5.1. The focal length is dependent the radius of the hole, R, the decrement of the refractive index, δ, and the number, N, of holes. The spacing, d, between the holes in not critical to the design. This figure is adapted from Ref. [95].

aperture [96]. The second method, requires a coherent beam. An aperture next to the sample can be used a reference beam for Fourier transform holography [97] as depicted in Fig. 5.2. In Fourier transform holography, the scattered light from the reference pinhole interferes with the scattered light from the sample. The interference is encoded at the detector plane by intensity modulations and by taking the Fourier transform of the recorded diffraction pattern, an image of the sample is retrieved. Fourier transform holography has been used to image magnetic structures using circularly-polarized light from synchrotrons with 50 nm resolution [98]. The resolution of Fourier transform holography is dependent of the size of the aperture. Increasing the resolution is challenging because as the aperture is decreased, more and more photons are blocked, thus becoming increasingly more photon inefficient.

The application of mirrors to x-rays was pioneered at Stanford by Kirkpatrick and Baez [99]. They used super polished substrates placed at 90 degrees with respect to each other, each with either a parabolic or elliptical curvature (see Fig. 5.3a). The curved substrates are able to focus a glancing incident x-ray beam and are known as K-B mirrors. The glancing incident angle is needed for high reflectivity. Another mirror geometry, the Schwarzschild configuration, uses spherical mirrors to focus the beam (see Fig. 5.3b) [100, 101]. The use of two mirrors in a proper design, can reduce the astigmatism from spherical surfaces [102, 103]. Due to the near normal angle of incidence in the Schwarzschild configuration, they are typically used in EUV applications with multilayer mirrors. Multilayer mirrors are layered structures designed such that a select bandwidth of radiation is reflected. The surface quality of the mirrors tend to limit resolution to about 100nm [104]. However, recent work using deformable mirrors, has improved the focal spot to around 10nm [105].

Mirrors do not require coherence, but the follow optics due require a coherent beam: the Fresnel zone plate and Laue lens. The Fresnel zone plate is a series of rings, designed such that some of the diffraction is focused to a spot (see Fig. 5.3c). The resolution from a zone plate is dependent on its fabrication quality, especially the width of the outer most ring. Similar to the zone plate, is the Laue lens (see Fig. 5.3d) [106]. The Laue lens can be thought of a one dimensional zone
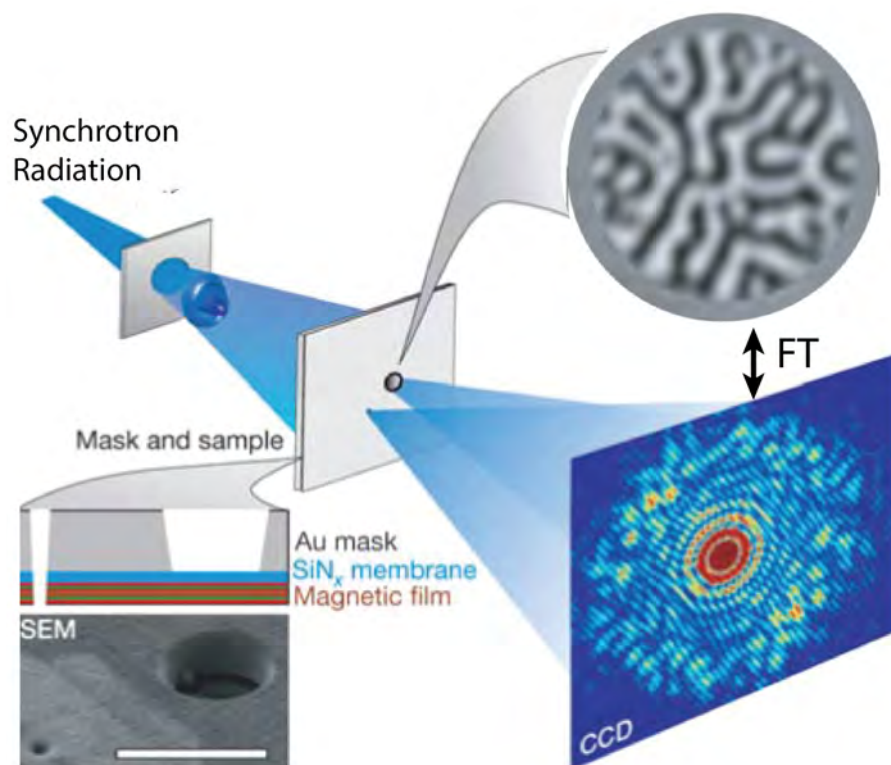
Figure 5.2: **Fourier Transform Holography** In Fourier transform holography, a small aperture is fabricated near the sample. The aperture creates a reference beam that interferes with the diffraction from the adjacent sample. The interference is recorded on a detector as intensity modulations. A Fourier Transform of the intensity results in an image of the sample. In the work depicted here, the sample consists of magnetic domains. Figure adapted from Ref. [98].

plate, creating a tight focus in one-dimension, as tight as 8nm [107]. The Laue lens is created with sputtering methods, as opposed to e-beam lithography techniques used in zone plate fabrication, allowing for 1 nm layers [108]. The ability to make thinner layer promises to further improve the spot size of the Laue lens because, like the zone plate, the resolution is dependent on the layer thickness.

The ability to focus x-rays leads to point scanning imaging forming methods. Point scanning microscopy techniques with zone plates have achieved 30nm resolution [109, 110], while direct imaging with zone plates have achieved 15, 12, and 10 nm resolution [111–113]. A combination of K-B mirrors and zone plates has recently demonstrated 5nm spot sizes [114], which is promising for future high-resolution imaging. Furthermore, by analyzing the intensity changes between adjacent points, quantitative phase information is possible [115].[1]

The imaging forming techniques used in this work do not require any image forming optics, thus the resolution is not dependent on fabrication quality. Furthermore, because no optics are needed between the sample and the detector, this technique is the most photon efficient form of imaging [117]. The resolution in this technique is not dependent on any apertures or pinholes, thus resolution is only limited by Abbe's diffraction limit (Eq. 2.2). This technique is not a point scanning technique, therefore large areas can be imaged in a single exposure. And finally, this technique is a full characterization of how light interacts with the sample yielding both amplitude and phase information. The technique used in this work is coherent diffractive imaging.

Coherent diffractive imaging (CDI), was adapted to optical problems from the Gerchberg-Saxton algorithm [118] used in electron microscopy, in 1978 by Fienup [119,120]. [2] At first this new imaging technique was limited to computer simulation, until the first demonstration with optical beams in 1988 and 1990 [122,123]. It was a decade later, in 1999, that the first demonstrations of CDI were demonstrated using x-rays in 1D by Robinson et al. [124] and 2D by Miao et al. [125].

With all the advantages of CDI, there also comes some challenges. The experimental con-

---

[1] A nice review on non-CDI imaging [116].
[2] A history of CDI is found in [121].

straints and requirements for CDI are discussed in Ch. 6. Overcoming some of those challenges is one aspect of these thesis work and is discussed in Chs. 7 and 8. And finally, extending CDI for stroboscopic dynamic studies is discussed in Ch. 9.
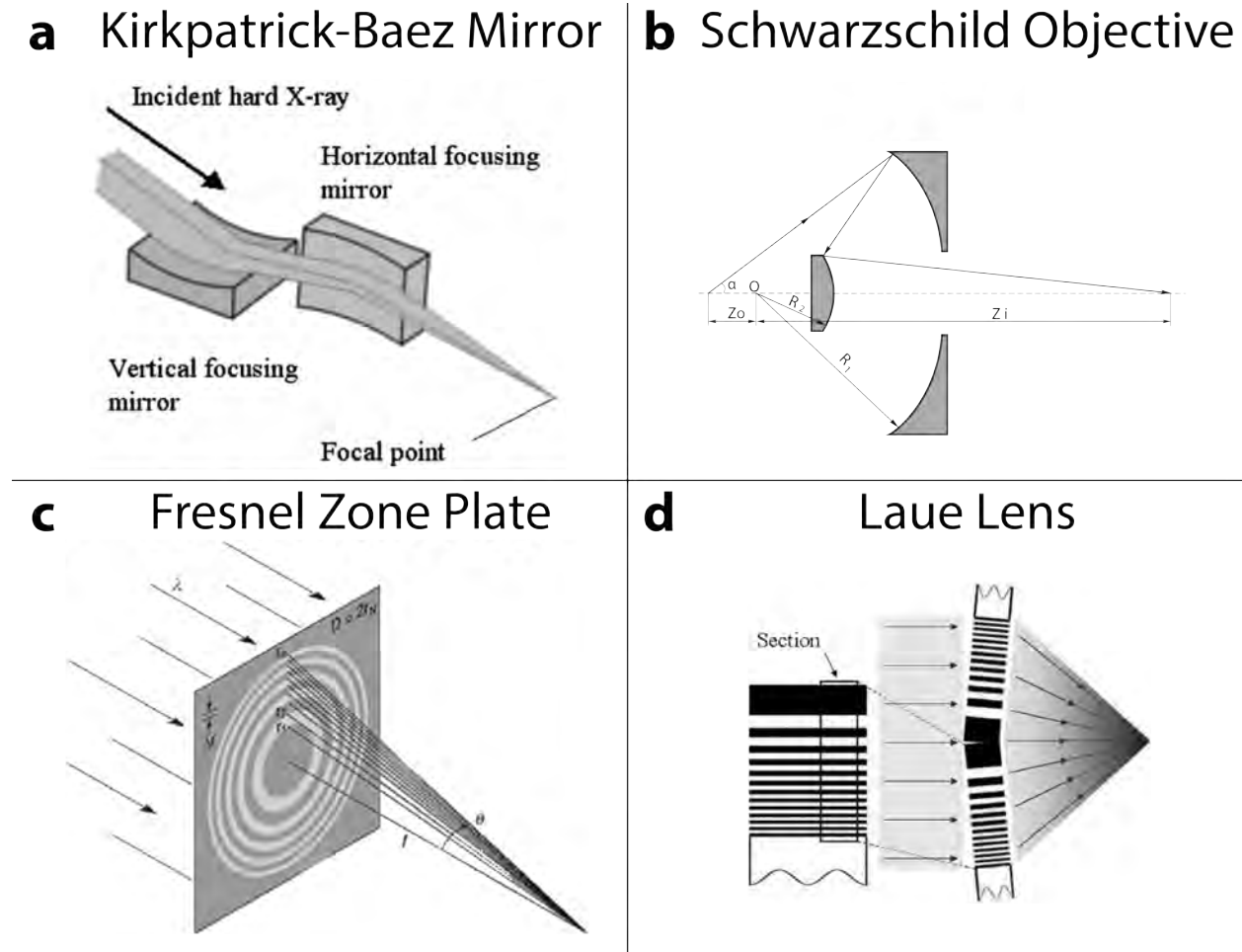
Figure 5.3: **Various EUV and X-ray Optical Elements** (a) The Kirkpatrick-Baez mirror which consists of two super polished substrates with parabolic or elliptical curvature for hard x-ray focusing. Panel adapted from Ref. [126]. (b) The Schwarzschild objective consists of two spherical mirrors, typically multilayer mirrors, and used in the EUV. Panel adapted from Ref. [101]. (c) The Fresnel zone plate is a diffractive element consisting of concentric rings. Panel adapted from Ref. [127]. (d) The Laue Lens is a diffractive element which can form a line focus from sputtered layers of materials. Panel adapted from Ref. [106].

Chapter 6

Coherent Diffractive Imaging

The objective of CDI can be stated as follows: given a diffraction pattern from an unknown object, reconstruct the object. If the phase could be measured on a detector, the recovery of the object would be a simple inverse Fourier transform (see appendix A for a discussion the applicability of the Fourier transform). Unfortunately, the phase is lost by the detector and various methods of phase retrieval must be employed.[1]

6.1   History of Phase Retrieval

In 1952, Sayre [130] noted Shannons sampling theory [131] may lead to a solution to the phase retrieval problem if the diffraction pattern could be sufficiently sampled. Twenty years later, Gerchberg and Saxton developed the first widely used algorithm for phase retrieval [118]. This algorithm used the diffracted amplitude and an image of the object to solve for the phase. Because an image of the object is required, this algorithm in not suitable for a CDI microscope when the sample is unknown. In 1978, Fienup built upon the Gerchberg-Saxton algorithm with a modification of the image constraint [119]. Instead of an image of the object, the object must be isolated and this algorithm was termed Error Reduction (see Fig. 6.1). The isolated object, or support constraint, is motivated and discussed in more detail in Sec. 6.2. Since Fienup's initial CDI algorithm, the CDI community has worked to improve phase retrieval algorithms with respect to convergence speed and robustness to noise. [120, 132–136].

---

[1] For review articles see Refs. [128, 129]

A notable example is the shrink-wrap algorithm put forward by Marchesini et al. in 2003 [133]. Before the shrink-wrap algorithm, the support constraint was applied like it is depicted in Fig. 6.1c: the same shape at each iteration even if the object is converging to a smaller sub-region. The shrink-wrap algorithm uses a blurred and thresholded version of the object, before the support constraint (Fig. 6.1b), as the isolation constraint. The shrinking support constraint leads to faster convergence and reduces stagnation problems of phase retrieval algorithms.

6.2   Oversampling and the Isolation Constraint

From Shannon's seminal paper on sampling theory [131], bandlimited, or isolated samples, if sampled at the Nyquist frequency, can be recovered exactly from their Fourier transform [138]. This is only true if the phase is known. Without the phase the diffraction amplitude must be sampled at greater than the Nyquist frequency.

Consider the phase retrieval problem as a set of linear of equations with known and unknown pixel values. The amplitude of the Fourier transform of the object is measured on a $N \times N$ pixel detector in frequency space (see Fig. 6.2). From the measurement of the Fourier transform, we have N^2 known data points. In object space, without the isolation constraint, we have N^2 unknown amplitude and N^2 phase points for a total of $2N^2$ unknowns. This does not have a unique solution.

To solve the problem, there must be a constraint to limit the number of unknowns. If we restrict the object to a square region of $N/\sqrt{2} \times N/\sqrt{2}$ then the number of unknowns becomes $N^2/2$ amplitude and $N^2/2$ phase points for a total of N^2 unknowns. Now the number of know and unknown pixels are the same allowing a unique solution. The isolation constraint in object space corresponds to a diffraction amplitude pattern that is sampled at greater than the Nyquist frequency leading to the so-called oversampling ratio [139–142], σ, which can be written as

$$\sigma = \frac{\text{total pixel number}}{\text{unknown-valued pixel number}}. \tag{6.1}$$

A theoretical oversampling ratio of 2 is required and this requirement corresponds to oversampling by $> \sqrt{2}$ in each dimension for a 2D object [140]. In practice, it is best to have a ratio of 4 or an
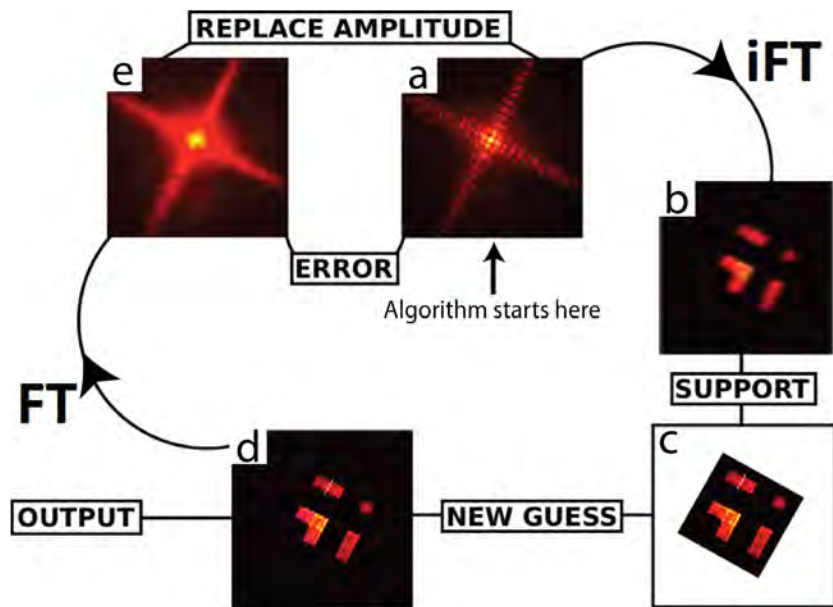
Figure 6.1: **CDI with Error-Reduction** (a) A measured diffraction pattern is fed into the algorithm and random phase guess is applied. (b) The diffraction in (a) is inverse Fourier transformed into object space. (c) The isolation constraint or support is applied. (d) Application of the support constraint yields a better guess of the object. (e) The better object guess in (d) is Fourier transformed back to frequency space. Here the phase is kept, but the amplitude is replaced with the measured amplitude. Convergence of the algorithm can be monitored by calculating the difference between (e) and (a). The algorithm continues to loop until some termination condition is met such as an error below a predefined threshold. Figure panels contain data from Ref. [137].
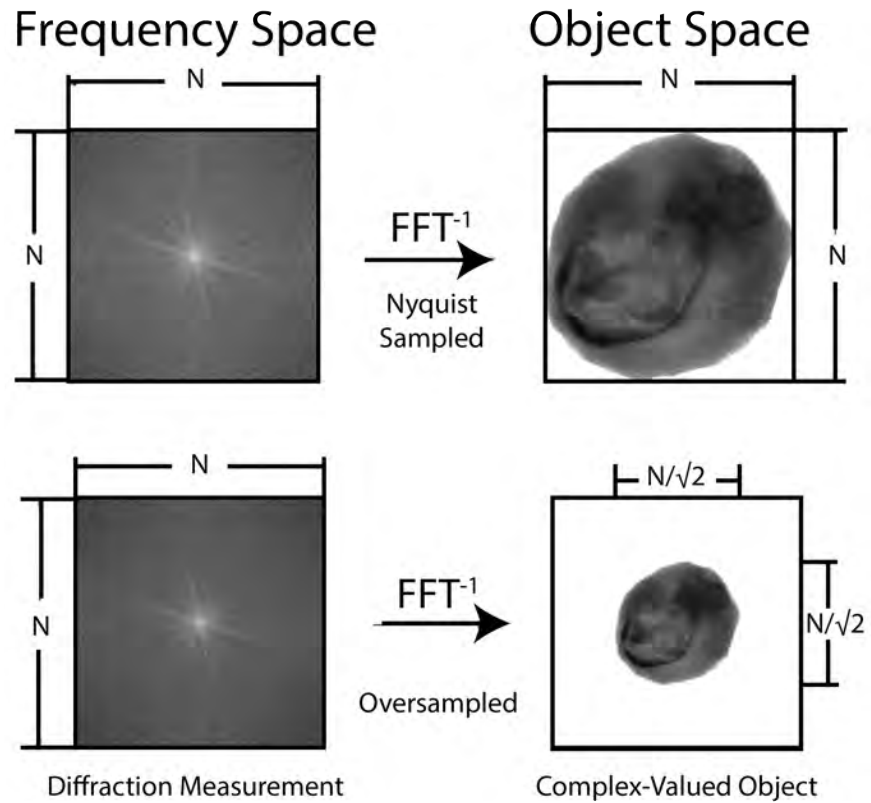
Figure 6.2: **Oversampling and a Isolated Object** (Top) A Nyquist sampled diffraction pattern, when inversed transformed, results in a object that fills the gird. (Bottom) An oversampled diffraction pattern, when inversed transformed, results in an isolated object. Figure adapted from Ref. [139].

oversampling of 2 in each dimension to overcome noise in the measurements.

For convenience, the oversampling ratio can be re-written using tunable experimental parameters

$$\sigma \geq 2 = \frac{N}{N/2} = \frac{N\ dx}{D} \tag{6.2}$$

where dx is the object pixel size and D is the largest extent of the sample. The object pixel size is related to the detecotor pixel size by Fourier relationships [138]

$$dx = \frac{\lambda z}{N\ px} \tag{6.3}$$

where λ is the wavelength of illumination, z is the distance from the sample to the detector, and px is the pixel size of the detector. Plugging Eq. 6.3 into Eq. 6.2 yields

$$\sigma = \frac{\lambda z}{D\ px} \geq 2 \tag{6.4}$$

a very useful expression when designing a CDI microscope.

6.3   Ptychography

Ptychography is a powerful CDI technique based on many diffraction measurements from the sample. The sample is illuminated and is scanned, area-by-area, with about 60%-70% overlap between adjacent scan positions. From the set of diffraction patterns, and the known shifts between scan positions, it is possible to reconstruct both the amplitude and phase of the sample.

6.3.1   History

Ptychography started with theoretical investigations of phase retrieval for crystalline samples [143] using the convolution theorem of Fourier optics [138].[2]   The early work was published in German, in which the German word for convolution is word for folding [145]. Following scientific naming conventions, the Greek work of fold is ptycho, hence the name ptychography.

The early description of ptychography considered a crystalline sample illuminated with a focused beam from a lens with a hard aperture. The diffraction pattern, using the convolution

---

[2] The discussion here is presented in greater detail in Refs. [144, 145]

theorem, is the Bragg peaks of the crystal diffraction convolved with the Fourier transform of the focused beam. Hoppe realized the phase could be retrieved by measuring the intensities of two adjacent diffraction orders and their interference fringes. At the time of the early ptychography work, coherent sources in the EUV and x-ray spectral regions were not fully developed and thus it was some time before ptychography became widely used.

Ptychography was developed for non-periodic objects in the 1990s [146]. It was realized that the resolution in a scanning microscope is not necessarily dependent on the focus spot size. Instead, collecting the diffraction patterns and using a Wigner deconvolution, the resolution is proportional to the scan step size as opposed to the spot size [145]. This early experimental work was able to decouple effects from the illuminating and improved the resolution of scanning microscopy, but the entire dataset needed to be deconvolved at once. This was not easily done at the time given the lack of computer resources to handle such large datasets.

A beakthrough in ptychography occurred in the early 2000s [147, 148]. Instead of using the entire dataset at once, as in the Wigner deconvolution method, one diffraction pattern can be considered at a time. In combination with phase retrieval methods pioneered earlier by Fienup [119, 120], each diffraction could be considered serially with the object updated piecemeal. With overlap from adjacent scan positions, ptychography has more constraints than traditional CDI. The first methods of serial ptychography required accurate knowledge of the illumination, but works in 2008 and 2009 further improved the ptychography algorithm to solve for both the object and the illumination [149, 150].

6.3.2   Ptychographic Data Collection

Here we address ptychography using EUV and x-ray sources, although the same considerations apply to other coherent sources (such as some forms of electron microscopy [151, 152]). We assume that the illumination is sufficiently coherent and monochromatic [153]. We also consider the thin sample approximation [149] applies to our case of study, such that the interaction of probe

and the sample can be described by:

$$\psi(\vec{r}) = O(\vec{r})P(\vec{r}) \tag{6.5}$$

where ψ is the exit-surface wave (ESW), O is the complex-valued object, P is the complex-valued probe, and $\vec{r}$ is the real space coordinate vector. We further assume that propagation from the ESW to the detector plane can be described with a propagator, $\mathfrak{F}$, and an inverse propagator, $\mathfrak{F}^{-1}$, such that (see appendix A for a discussion):

$$\psi(\vec{r}) = \mathfrak{F}^{-1}[\Psi(\vec{u})] = \mathfrak{F}^{-1}[\mathfrak{F}[\psi(\vec{r})]] \tag{6.6}$$

where Ψ is the ESW at detector and $\vec{u}$ is the spatial frequency coordinate vector. In many instances, the propagator is the Fourier transform because the detector is placed sufficiently far from the sample such that the far field approximation is satisfied:

$$\frac{W^2}{z\lambda} << 1 \tag{6.7}$$

where W is the diameter of the area illuminated on the sample, z is the distance from the sample to detector plane, and λ is the wavelength of illumination. The detector records the intensity, $\mathcal{I}$, of the diffracted light given by $\mathcal{I}(\vec{u}) = |\Psi(\vec{u})|^2$. As discussed in 6.2, the geometry of the data collection needs to ensure oversampling of the diffraction [140].

A ptychographic dataset consists of scanning the probe over the object at j known positions, r_1, r_2, r_3,...,r_j, yielding a set of intensity measurements:

$$\mathcal{I}_j(\vec{u}) = |\mathfrak{F}[O(\vec{r})P(\vec{r} - r_j)]|^2 \tag{6.8}$$

where r_j is a shift transverse to the beam direction and the $|\ |$ indicate the absolute value. At each scan position, the illuminated portion of the sample overlaps with adjacent scan positions. For a robust reconstruction, $60\% - 70\%$ overlap is typical between adjacent scan positions [150]. A useful chart for ptychographic data collection is shown in Fig. 6.3. Assuming the illumination is a uniform circle, Fig. 6.3 shows the overlap of adjacent position as a function of radius, R. For an overlap of about 70%, the illumination needs to be shifted by $R/2$. For the work in this thesis,

shifts of R/2 are considered a minimum threshold of overlap. Most ptychographic datasets had $R/3$ or $R/4$ overlap because the redundant information allows the algorithm to be more robust in the presence of noise. However, too much overlap can be a problem, because the diversity in the diffraction patterns decreases resulting in a stagnation of convergence. To overcome the lack of diversity in the diffraction patterns, a large scan is needed.

When scanning the sample in a rectilinear grid, artifacts from the periodic scan grid may be introduced into the reconstruction [154]. To avoid this, each scan step is randomly offset by up to 20% of its step size. This is the so-called noisy grid scan pattern. Its been shown the best scan pattern is a Fermat spiral because there is uniform illumination without periodicity [155].

6.3.3   The Ptychography Algorithm

The ptychography algorithm starts with the ESW from an object and probe guess such that

$$\psi_{Gj}(\vec{r}) = O_G(\vec{r})P_G(\vec{r} - r_j) \tag{6.9}$$

where the subscript G designates a guess. Typically the initial guess of the object is unity; the probe is an estimate of the illumination based on a size or better yet, a calculation of the illumination at the sample through all the optical components upstream. The ESW guess is propagated to the detector, forming a guess of the diffraction

$$\Psi_{Gj}(\vec{u}) = \mathfrak{F}[\psi_{Gj}(\vec{r}] \tag{6.10}$$

The recorded diffraction pattern, $\mathcal{I}(\vec{u})$, at the position r_j, is used to constrain the algorithm with the modulus constraint, M, expressed as

$$\Psi_{Mj}(\vec{u}) = \sqrt{\mathcal{I}(\vec{u})}\frac{\Psi_{Gj}(\vec{u})}{|\Psi_{Gj}(\vec{u})|} \tag{6.11}$$

where $\Psi_{Mj}(\vec{u})$ is the diffraction at the detector plane, consistent with the measured diffraction, which also contains a guess of the phase. The diffraction, $\Psi_{Mj}(\vec{u})$, is propagated back to the sample plane forming a better guess, $\psi'_{Gj}(\vec{r}) = \mathfrak{F}^{-1}[\Psi_{Mj}(\vec{u})]$, of the ESW because the ESW is now consistent with the measured diffraction.
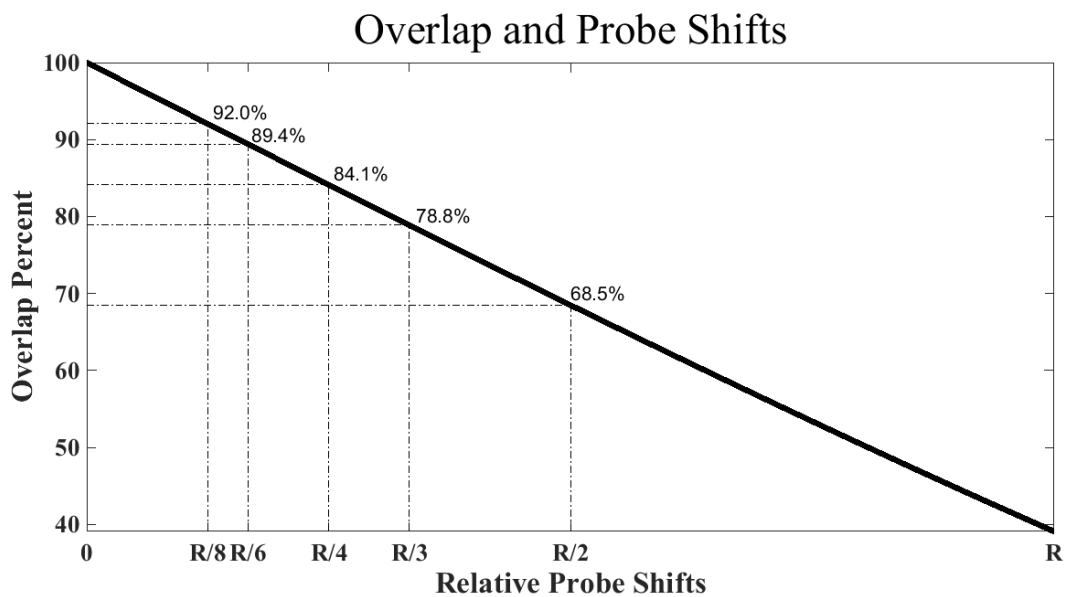
Figure 6.3: **Overlap and Probe Shifts** Assuming the illumination (probe) is a uniform circle, this graph shows the overlap of adjacent scan positions as a function of shift. The vertical axis is the amount of overlap in percentage and the horizontal axis is the probe shift in units of circle radius R.

At this point, the object and probe guesses are updated employing the known overlap between adjacent positions. The particular form of the update varies between algorithms, see for example Refs. [149, 150, 154, 156–158]. The ptychography reconstructions in this work are based on the extended ptychographical iterative engine (ePIE) algorithm [150]. In this algorithm the object guess, $O_{Gj}(\vec{r})$, and the probe guess, $P_{Gj}(\vec{r} - r_j)$, are updated by the following equations:

$$O_{Gj+1}(\vec{r}) = O_{Gj}(\vec{r}) + \alpha \frac{P_{Gj}^*(\vec{r} - r_j)}{|P_{Gj}(\vec{r} - r_j)|^2_{max}}(\psi'_{Gj}(\vec{r}) - \psi_{Gj}(\vec{r})) \tag{6.12}$$

$$P_{Gj+1}(\vec{r}) = P_{Gj}(\vec{r}) + \beta \frac{O_{Gj}^*(\vec{r} + r_j)}{|O_{Gj}(\vec{r} + r_j)|^2_{max}}(\psi'_{Gj}(\vec{r}) - \psi_{Gj}(\vec{r})) \tag{6.13}$$

where α and β are feedback parameters and $*$ denotes the complex conjugate. The feedback parameters in this work are unity. These better guesses, $O_{Gj+1}(\vec{r})$ and $P_{Gj+1}(\vec{r})$, are be fed back into the algorithm until all j positions have been updated. At this point, one full iteration of ptychography is complete. Further iterations of ptychography will continue following the described iterative procedure, until a convergence condition is met, which usually consists of a minimization of an error metric [159]. A flow chart of ptychography is shown in Fig. 6.4. Having described CDI, its application to EUV and and specially in a reflection geometry is discussed next.

-
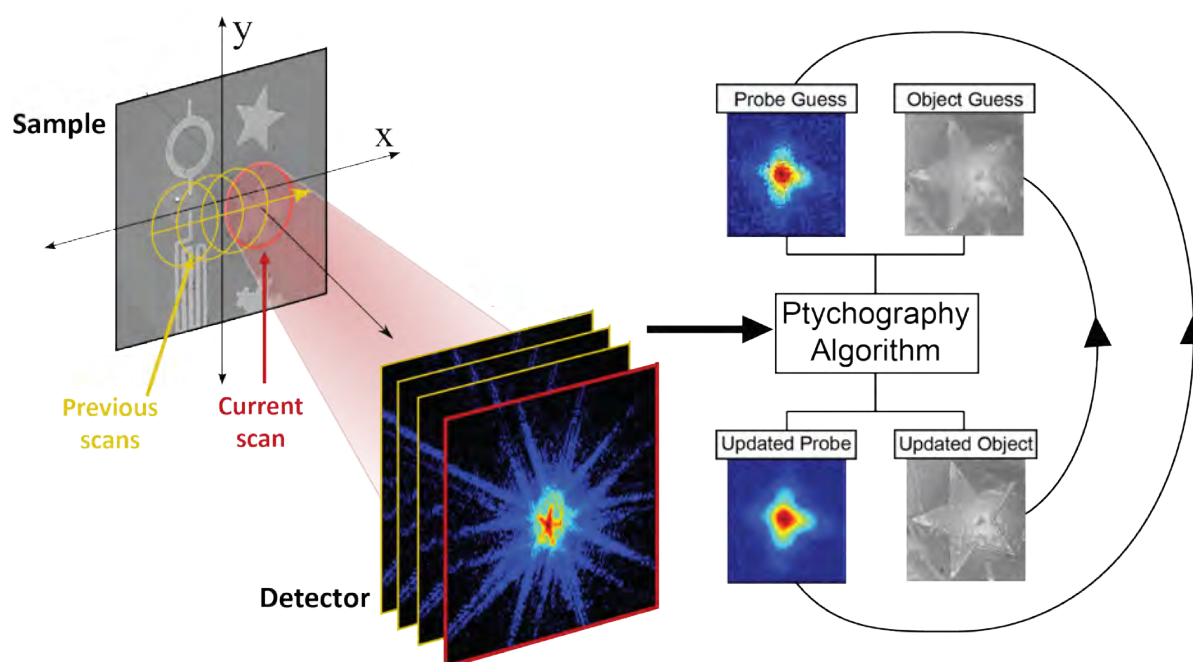
Figure 6.4: **Ptychography data collection and flowchart** The ptychographic dataset consists of a set of diffraction patterns collected at known object shift positions. The dataset is fed into the ptychography algorithm and which solves for both the object and the probe.

Chapter 7

Coherent Diffractive Imaging in a Reflection Geometry

As discussed previously, coherent diffractive imaging (CDI) is a promising solution for EUV and x-rays imaging because the resolution scales with the wavelength. Nearly all of the EUV and x-ray CDI demonstrations to date have been in a transmission geometry, with only a few exceptions [160–164]. None of the previous works have been able to obtain near wavelength limited resolutions which is needed to image nanostructures patterned on substrates, substrates that are too thick for transmission imaging.

This chapter is divided into two sections. In the first section, a benchtop optical CDI microscope is developed, using a 632 nm Helium Neon laser, to rapidly iterate solutions for reflection mode imaging. An algorithm was developed, named tilted plane correction, which enabled high-fidelity reconstructions. The application of tilted plane correction using 30 nm high-harmonic radiation, is the topic of the second half of this chapter. The highest resolution-to-wavelength images were obtained in the EUV and x-ray spectral regions using CDI in this work.

7.1 Aperture-Illumination Coherent Diffractive Imaging

Interestingly, the application of CDI, using light sources in any region of the electromagnetic spectrum, has been limited almost exclusively to transmission mode imaging (at the time of this work in 2012), with the exception of two recent experiments [160, 161]. This is due to the fact that reflection mode geometries are intrinsically more demanding than transmission mode samples since it is far more difficult to isolate the sample. Marathe et al., Ref. [160], isolated the object by

placing a pinhole directly onto the sample. While this simplistic approach works for their micron scale samples, it will not work with sensitive nanoscale structures because the attachment of the pinhole will either damage or alter sensitive samples. Furthermore, their technique does not easily allow imaging of different parts of the sample since the pinhole is attached directly to the sample. In the work by Roy et al. [161], the pinhole was not placed on the sample, but instead placed between the sample and detector. Unlike Ref. [160], the sample is unaltered and different areas can be imaged, but the numerical aperture (NA) is severely limited. The reduction in NA limits the attainable resolution and therefore their resolution of 60nm is far from their wavelength of 2.5nm.

We demonstrate the most straightforward strategy for reflection mode CDI by simply illuminating the object with the image of a pinhole, an approach termed aperture-illumination CDI (AICDI). For the first time CDI can image and scan over large samples with high NA, in an off-axis reflection geometry, demonstrating a versatile reflection mode microscope.[1]

7.1.1   Transmission mode AICDI

In order to implement and test the AICDI technique, and associated data processing algorithms, a proof-of-concept system is developed using a polarized 632.8 nm HeNe laser in a transmission geometry. A schematic diagram of the setup is shown in Fig. 7.1. The illuminated beam overfills a 300 μm diameter circular aperture. The aperture is imaged to the sample plane using a one-to-one 4f imaging system. A bundle of suspended 26 μm diameter copper wires in a crisscross pattern across a half-inch diameter ring is used as the sample. The inset in Fig. 7.1 shows an optical microscope image of the sample. A positive lens placed directly after the sample sends the scattered light into the Fourier plane at the CMOS detector (Mightex Systems MCE-B013, 5.2 μm pixel size). In general, the positive lens after the sample is unnecessary, however the detector used in this experiment has a small collection area, such that a demagnification of the far field was required in order to use a wavelength as large as 633 nm. The aperture size is selected to satisfy the oversampling criterion [139–142] (see Sec. 6.2), where the distance between the lens and the

---

[1] This section is adapted from Gardner et al. [165]

detector is 11.6 mm, corresponding to an NA 0f 0.22 for our 5.3 mm detector.

A bundle of suspended copper wires, 26μm diameter, were illuminated with an image of the aperture to demonstrate the effectiveness of this technique for imaging extended samples. An optical microscope of the suspended wires is shown in Fig. 7.1. An example of a recorded diffraction pattern is shown in Fig. 7.2a. We use the RAAR algorithm as outlined in Ref. [134] with shrink-warp [133] to recover the phase. (An explanation of the shrink-wrap algorithm is given in 6.1). With the recovered phase, we are able to reconstruct the exit surface wave as shown in Fig. 7.2b. This technique constitutes a bright-field imaging microscope.

A dark-field image can be obtained, if instead the scattered light, with the sample removed (leaving the rest of the system unchanged), is measured. This measurement of the un-diffracted illumination is used to reconstruct the electric field at the sample plane. During the reconstruction process, the complex amplitude of the illumination at the detector plane is subtracted at each iteration. Subtracting out the illumination results in the wires appearing bright instead of dark as in Fig. 7.2c, and constitutes a dark-field microscope.

By scanning the sample in a plane perpendicular to the optical axis, we are able to reconstruct different areas of the extended sample independently. With overlap between the scan positions, we can register adjacent reconstructions to build up a large-area, high resolution image. Figure 7.2d shows a number of reconstructions of this sample, which were overlaid in post-processing. Colored circles indicate the area that was illuminated by the aperture for each individual reconstruction.

7.1.2 Reflection mode AICDI

Having shown the ability to isolate and image part of an extended sample in transmission, AICDI is now applied to samples in a reflection geometry. Unless the detector has a hole for an illumination beam, the sample must be at some non-zero angle of incidence with respect to the beam. At non-zero incidence angles, and at high NA, the far field diffraction pattern is no longer proportional to a uniformly spaced Fourier transform of the specimen, as evidence by the curvature of the diffraction pattern in Fig. 7.3a. A correction is needed to remap the diffraction
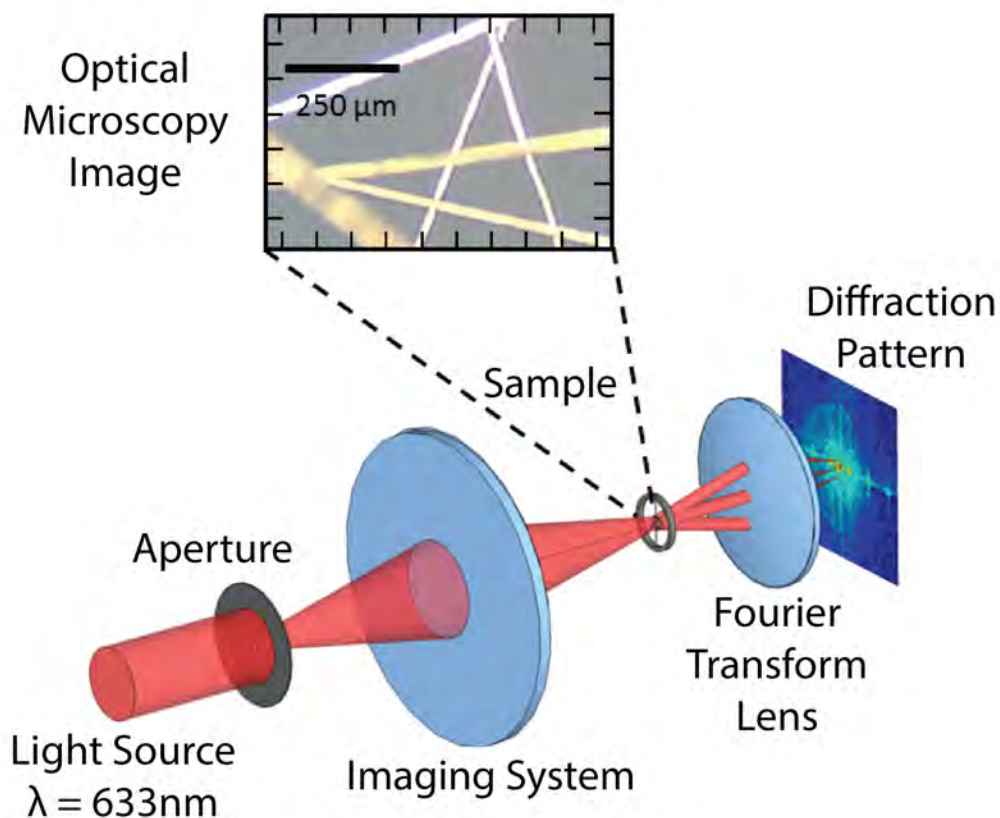
Figure 7.1: **Aperture-Illumination Setup** The illumination is passed through a pinhole aperture and then is imaged onto the sample plane. The inset shows an optical microscope image of the sample which consists of a crisscross pattern of 26 μm diameter wires. After the sample, a positive lens is placed transforming the scattered light into the Fourier plane at the detector where the diffraction pattern is recorded. Figure adapted from Gardner et al. [165].
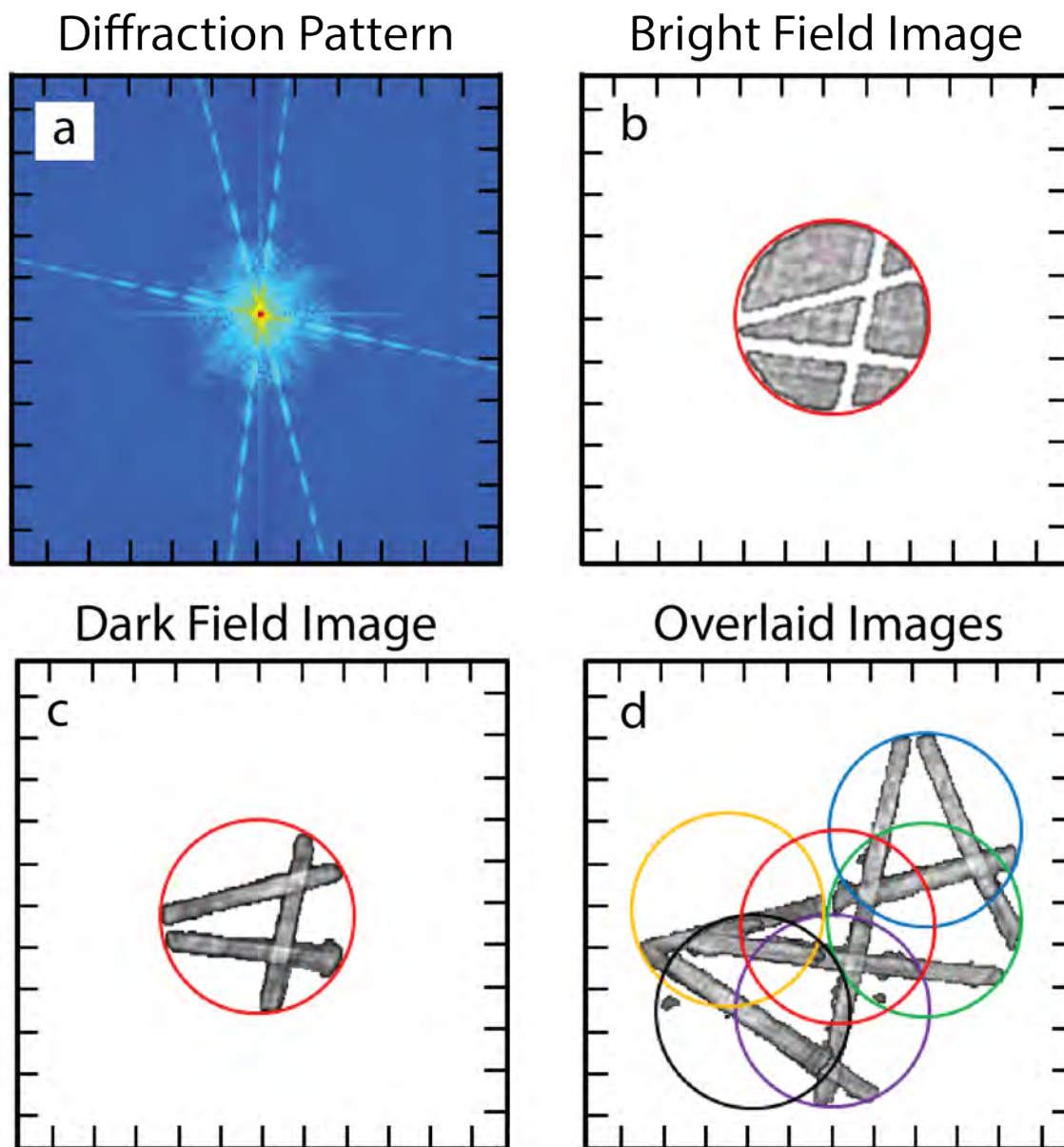
Figure 7.2: **Aperture-Illumination Transmission Imaging** (a) An example of the collected diffraction from the wire sample scaled by the 4th root. (b) The exit surface wave reconstructed from the diffraction pattern. The circle outlines the area illuminated by the aperture. (c) A reconstruction when the illumination is subtracted out. (d) Overlay of the images from many scan positions. The circles represent the outline of the aperture illumination at different scan positions. Figure adapted from Gardner et al. [165].
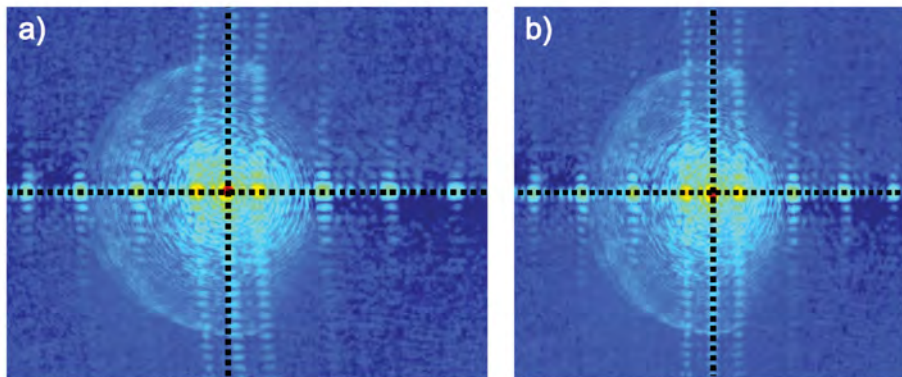
Figure 7.3: **Tilted Plane Correction** (a)The raw diffraction from light scatted by the sample at an angle of 30 degrees (b) The data mapped onto a linear grid in frequency space. The dotted black lines are added to highlight the curvature seen in the tilted sample diffraction shown in (a). Both images have been scaled by the fourth root. Figure adapted from Gardner et al. [165].

onto a linearly spaced grid. This remapping, termed tilted-plane correction, is described in detail in appendix B and Ref. [165]. The application of titled-plane correction allows the use of the Fast-Fourier transform (FFT) algorithm [166, 167]. The use of the FFT improves the speed of the algorithms and allows the use of any of the existing phase retrieval algorithms.

To demonstrate the tilted-plane correction and reflection mode imaging, the transmission system was modified so the sample was at an angle of $\theta = 30$ degrees (Fig. 7.4a). The same detector and Fourier transform lens were used as in the transmission setup, but were re-positioned such that they were aligned along the specular reflection from the sample. The NA was kept at 0.22 and the resolution at 1.4μm. A positive 1951 Untied States Air Force (USAF) resolution target was used as the sample. Figure 7.3a shows the diffraction pattern from the vertical bars of group 5 (element 1) of the resolution target. The black dashed lines are overlaid to illustrate the curvature in the diffraction resulting from the non-zero angle of incidence. In Fig. 7.3b, the re-mapped diffraction onto a linear grid in spatial frequency is shown. After the interpolation of tilted-plane correction, the diffraction pattern is proportional to the modulus of the Fourier transform of the sample. Using the same iterative phase retrieval algorithm as mention in section 7.1.1, the AICDI technique is capable of reconstructing an arbitrary position of the target. Reconstructions are

overlaid and shown in Fig. 7.4b. An objective based bright field microscopy image is shown in Fig. 7.4c for comparison.

7.2   Near-Wavelength Resolution CDI in Reflection with EUV

The above benchtop proof-of-principle demonstration of high-NA reflection CDI is now adapted and applied to EUV radiation. A 30 nm high-harmonic beam is used to illuminate a titanium-patterned silicon wafer in a reflection geometry. High quality, high contrast, full filed images are retrieved using tilted plane correction and ptychography. Images with 80 nm by 40 nm lateral (1.3λ) resolution are obtained with quantitative phase information enabling profilometry with 6 angstrom (Å) resolution.[2]

7.2.1   High numerical aperture data collection of scattered EUV

Intense ultrashort pulses from a Ti:Sapphire laser amplifier system are used to generate the high-harmonic beams (see Ch. 4 for a discussion on high-harmonic generation). In this experiment, the driving laser had a central wavelength of 780 nm, pulse energy of 1.4 mJ, and operated at a 5 kHz repetition rate with 22 fs pulses. The waveguide used to generate the harmonics was 200 μm in diameter, 5 cm long, and filled with argon at 36 Torr backing pressure. After the waveguide, a differential pumping scheme is used to limit absorption of the EUV light and maintain high vacuum (10^{-6} Torr) is the experimental chamber. To remove the co-propagating driving laser from the harmonic radiation, a pair of silicon rejecter mirrors, set near Brewsters angle for 780 nm, is used with two 200 nm-thick aluminum filters.

Figure 7.5a depicts the inside of the experimental chamber where two 45° angle-of-incidence multilayer mirrors select the 27th harmonic (28.8 nm). The harmonic beam is focused onto the sample using a nickel-coated ellipsoidal mirror with a 5° grazing incidence angle. The sample is placed just after the focus of the ellipse, at an angle of 50.5° and the scattered light is recorded on an EUV-sensitive CCD with a square array of 2048 × 2048 pixels, each with a side-length of

---

[2] This section adapted from Zhang and Gardner et al. [168].
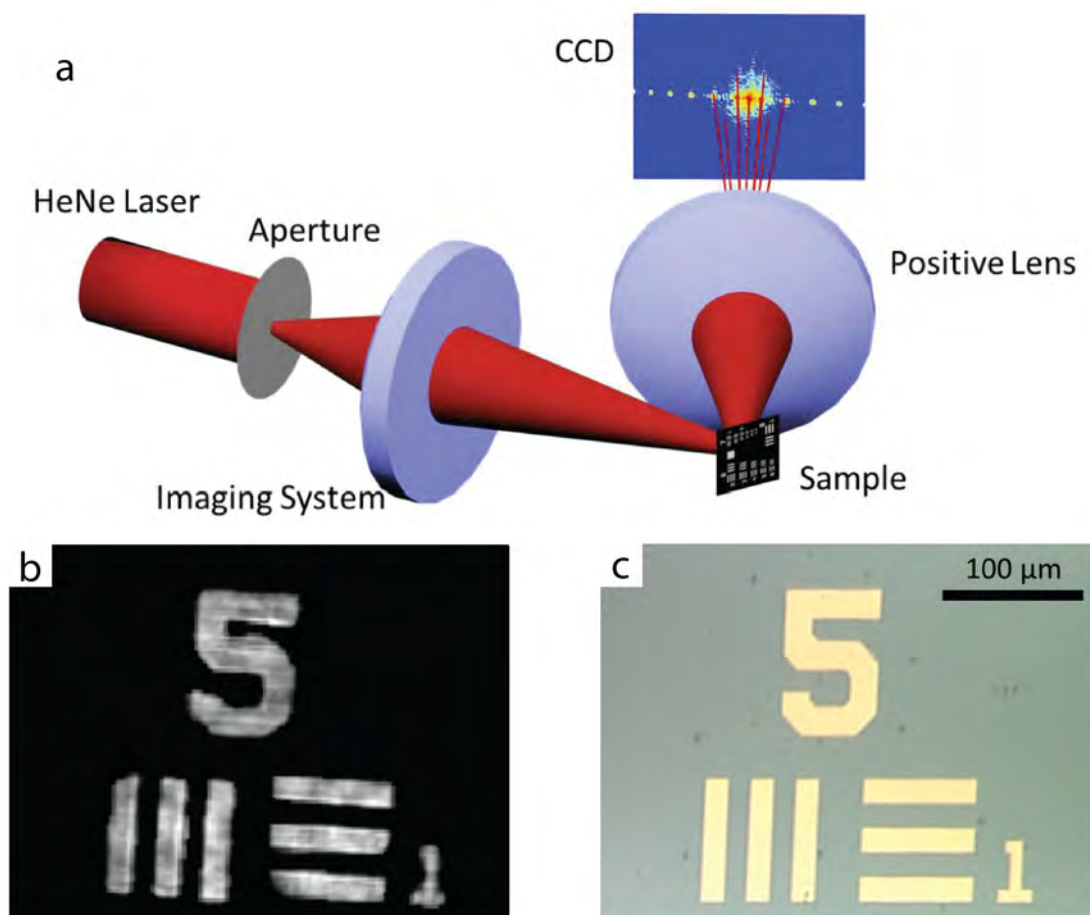
Figure 7.4: **Aperture-Illumination Reflection Imaging** (a) A schematic of the setup. Note that a negative USAF pattern is shown, but a positive USAF was used in the experiment. (b) Several images with different scan positions are overlaid to show the AICDI reconstructions. (c) A traditional bright-field microscopy image of the sample. The scale bar in (c) is shared with (b). Figure adapted from Gardner et al. [165].

13.5 μm (Andor iKon-L). The CCD plane of the camera is placed 3.17 cm from the sample and perpendicular the specular reflection, resulting in a numerical aperture of 0.4. Figure 7.5b shows an SEM image of the sample, consisting of titanium shapes patterned onto a silicon substrate using e-beam lithography. This same sample was used in a previous experiment and details about the fabrication can be found in the supplemental section of Ref. [169]. Due to the sample's age and its storage in a laboratory environment the surface of the sample was contaminated, which resulted in very fine height variations across the sample. The fine variations on the sample are used, as discussed below, to compare our CDI methods with SEM and AFM.

Before collecting the ptychographic dataset (see Sec. 6.3.3), the beam size at the sample plane is measured using a knife-edge scan. The beam size diameter was measured to be 12 μm in both the horizontal and vertical directions. With a step size of $\approx$ 3 μm, we ensure about 70% oversample between adjacent scan positions (see Fig. 6.3). The camera recorded diffraction patterns from a total of 198 positions in a nearly rectangular scan grid of 18×11 points. To prevent periodic artifacts from being introduced by the scan grid, random offsets up to 20% of the step size are added before each step. Each collected diffraction pattern had an exposure of 0.1 s with 3 accumulations for a total exposure time of 59.4 seconds.

7.2.2   Reconstructing high-NA reflection geometry data using CDI

An example of a raw diffraction pattern from the sample is shown in Fig. 7.6a. The frequencies associated with the raw diffraction are mapped non-linearly onto the detector due to a combination of the non-zero angle-of-incidence and the high NA data collection. In order to use the fast Fourier transforms [166, 167] in our data analysis, the raw diffraction is re-mapped into linear frequency using tilted plane correction [165, 168, 169]. The remapped, or corrected, diffraction pattern is shown in Fig. 7.6b. As a result of the remapping, the NA in the x-direction (horizontal) is reduced compared with the y-direction (vertical). The diffraction patterns were cropped to 512×1024 pixels corresponding to a reconstruction pixel size of 76 nm in the x-direction and 38 nm in the y-direction.
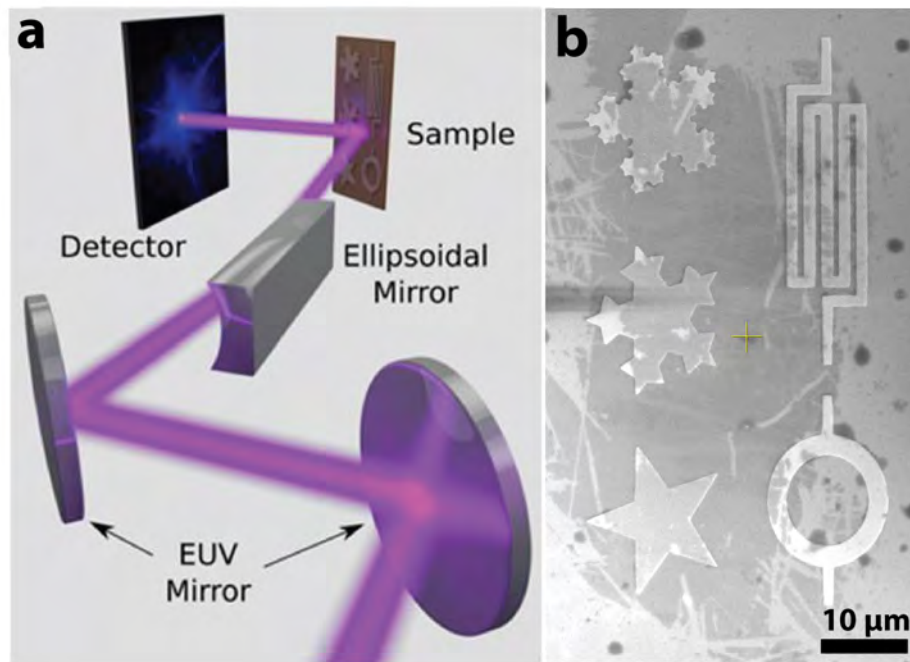
Figure 7.5: **High-NA reflection geometry and sample** a) A depiction of the experimental chamber showing high numerical aperture data collection of diffracted EUV light from the sample. The multilayer mirrors select a single harmonic and the ellipsoidal mirror focus the EUV onto the sample. b) A scanning electron microscope image of the sample, which consists of patterned titanium shapes on a silicon wafer. Panel (a) is adapted from Zhang, Gardner et al. [168].
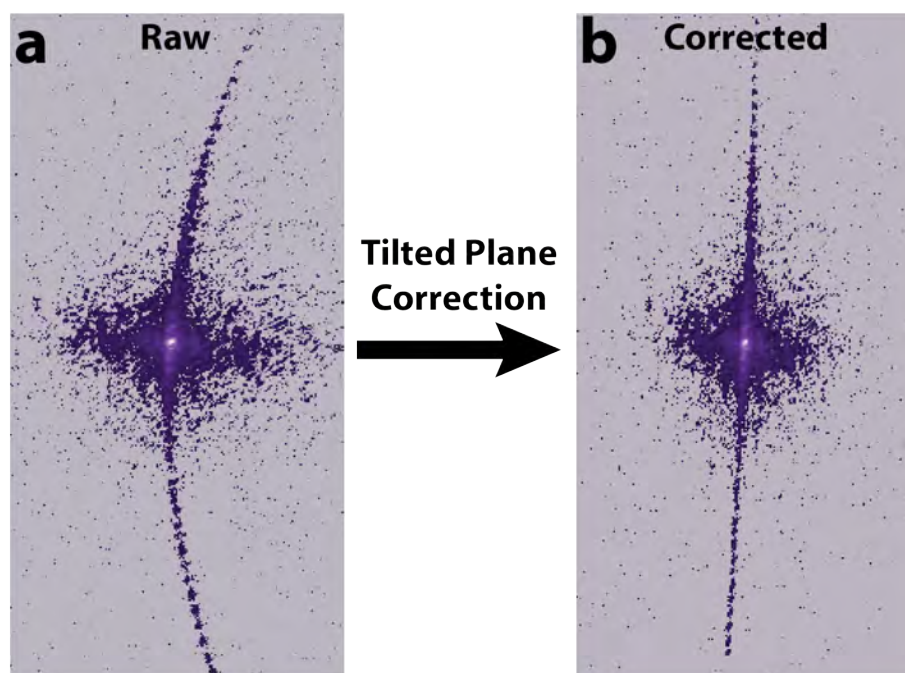
Figure 7.6: **Tilted Plane Correction in the EUV** a) Diffraction collected from the sample in a high-NA reflection geometry. The frequencies associated with the diffraction are mapped non-linearly onto the detector. b) The remapped, or corrected, diffraction pattern. In the corrected diffraction, the frequencies are linearly spaced. Figure adapted from Zhang, Gardner et al. [168].

A complex-valued image of the sample was reconstructed using the extended ptychographical iterative engine (ePIE) algorithm [150] with position refinement [170]. The retrieved amplitude and phase are shown in Fig. 7.7b,c with a SEM image for comparison in panel (a). The phase information, Fig. 7.7c, is used to create the 3D rendering of the sample shown in Fig. 7.8.

7.2.3   Resolution Characterization

Three methods were used to characterize the lateral resolution: the phase retrieval transfer function [171, 172], the modulation transfer function (MTF), and a knife-edge test (10%-90% width). All approaches to characterize the resolution, shown in appendix C, support a lateral spatial resolution of 76 nm in the horizontal direction and 38 nm in the vertical direction.

The phase of the ptychographic reconstruction was converted to height using

$$\phi = \frac{2\pi}{\lambda}(2h\cos\theta) \tag{7.1}$$

where ϕ is the reconstruction phase, λ is the wavelength of illumination, h is the sample height, and θ is the angle of incidence on the sample. To avoid 2π ambiguities or complex reflection coefficients, only the heights of the substrate are compared with the AFM. The AFM image had a higher resolution than our ptychographic reconstruction, so a Gaussian blur was applied, such that the resolution is equivalent. After smoothing, the 2-σ (95% confidence interval) of a histogram difference of the CDI calculated height and AFM profile is ≈ 6 Å.
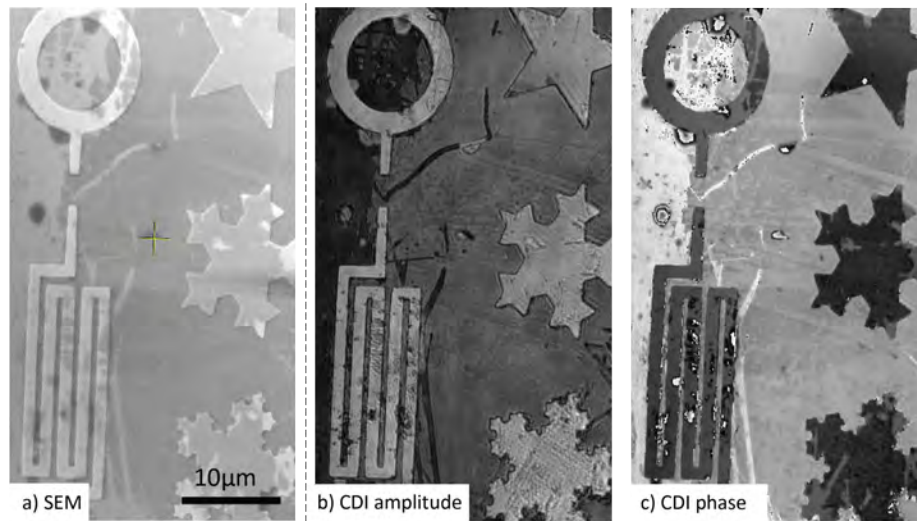
Figure 7.7: **High-Resolution EUV imaging in a reflection geometry** a) Scanning electron microscopy (SEM) image of the sample for comparison with ptychographic coherent diffractive imaging (CDI) b) Amplitude and c) phase reconstruction. Figure adapted from Zhang, Gardner et al. [168].
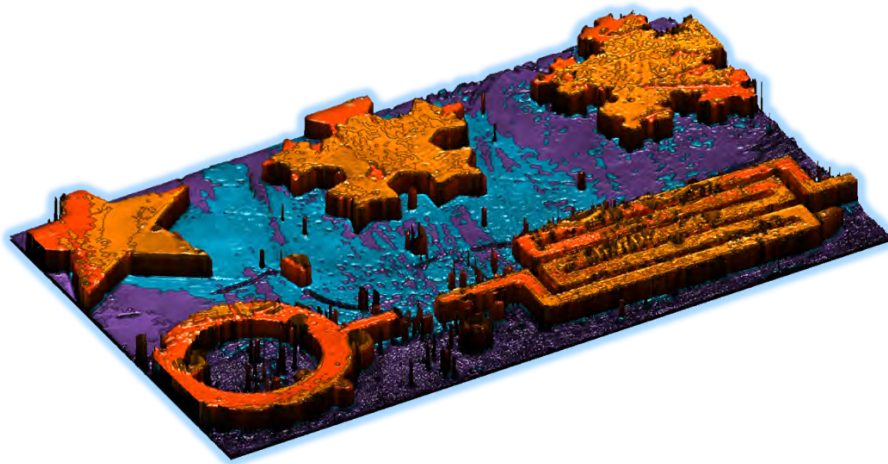
Figure 7.8: **Three-Dimensional Rendering from the Phase Information** Using the phase information from the ptychographic reconstruction, a 3D rendering is generated. Figure courtesy of Dan Adams.

Chapter 8

Sub-wavelength coherent imaging of a periodic sample

Progress in algorithm development and computing, coupled with improvements in coherent short wavelength light sources, are leading to revolutionary advances in coherent diffractive imaging (CDI) at extreme ultraviolet (EUV) and X-ray wavelengths. However, to date it has been challenging to obtain high-fidelity images of periodic objects using CDI because most of the diffraction pattern is dominated by intense peaks from the underlying periodicity. In this chapter, a tabletop 13.5 nm high harmonic beam is used to make two significant advances: first, a demonstration of high-quality imaging of an extended nearly-periodic sample for the first time, and second, sub-wavelength spatial resolution (12.6nm) imaging is achieved, also for the first time. The key to both advances is a novel technique, termed modulus enforced probe (MEP), which uses the far-field diffraction of the illumination as a constraint in the CDI algorithm. This new technique enables faster convergence, quantitative reconstructions, the ability to image periodic objects, and is robust in the presence of background noise. This work is important for high-resolution imaging of a broad range of next-generation nanoscale electronics. [1]

8.1   Introduction

High resolution imaging is needed to support the development of next-generation EUV lithography, nanoelectronics, data storage, and self-assembled nanostructures, as well as functional imaging of nano-enhanced devices. Due to the wavelength dependent diffraction limit, short wavelength

---

[1] This chapter is adapted from Gardner et al. [173]

sources in the extreme-ultraviolet (EUV) and soft X-ray regions of the spectrum are attractive for high resolution imaging. However, most EUV optics are costly, imperfect, lossy, and cannot reach diffraction-limited spatial resolution. Coherent diffractive imaging (CDI) techniques, as discussed in chapter 6, address the critical limitations in EUV optics by employing computational techniques to form images. Moreover, CDI techniques are the most photon efficient form of imaging because there are no lossy optics between the sample and the detector [117]. Using CDI, it is now possible to achieve diffraction-limited spatial resolution at short wavelengths.

For non-periodic samples, the CDI technique known as ptychography (Sec. 6.3) can reliably, and simultaneously, solve for the sample and illumination. On the other hand, periodic samples pose a particular challenge to CDI techniques because the lack of diversity in the diffraction patterns, resulting in poor convergence of the algorithm [125, 130, 140, 163, 174, 175]. Moreover, the spatial resolution achieved to date, for real-world objects under good reconstruction conditions, was limited to $1.3\times$ the wavelength (λ) [168].

In this work, using a tabletop 13.5 nm high harmonic light source, a sub-wavelength resolution (0.9λ) image of an extended sample is achieved in the EUV region for the first time. Also for the first time, high-fidelity, full-field, quantitative imaging of near-periodic objects is demonstrated with CDI. The key to achieving high-fidelity images of periodic samples is a novel constraint termed Modulus Enforced Probe (MEP). The new constraint, MEP, is based on one additional measurement of the illumination on the detector. This additional measurement is then used within a ptychography algorithm, such as the extended ptychographic iterative engine [150], to highly constrain the guess for the illumination beam. Furthermore, the measurement of the illumination is a measurement of the total power of the input beam allowing quantitative amplitude and phase information for both the sample and illumination. Using the MEP technique also improves the robustness of the algorithm in the presence of noise, reduces artifacts from cross-talk between the sample and illumination, and converges in fewer iterations. To my knowledge, the experimental demonstration discussed in this thesis, is the best resolution-to-wavelength ratio for any full-field, non-isolated sample, CDI-based microscope.

8.2 Experimental set-up and Modulus Enforced Probe methodology

Bright, phase-matched, high harmonic beams (see Ch. 4) are generated in a KMLabs eXtreme Ultraviolet Ultrafast Source by focusing an ultrafast infrared driving-laser into a helium-filled waveguide. The driving-laser is a 3 kHz KMLabs Dragon centered at a wavelength of 785 nm, with 23 fs pulse duration and 2 mJ pulse energy. The laser is focused and coupled into a 150 μm diameter waveguide, filled with 500 Torr of helium, which is carefully engineered to minimize the reabsorption of the EUV radiation. After the high harmonic generation in the waveguide, most of the residual infrared light is removed by a beam separator: a Brewster-angle silicon substrate coated with $\approx$210 nm of ZrO_2 [137, 176–178]. Any residual infrared light after the beam separator is removed with a 600-nm thick zirconium filter.

As shown in Fig. 8.1, a pair of Si/Mo multilayer mirrors are used to select and focus a single harmonic order, at a wavelength (λ) of 13.5 nm $\pm$ 0.2 nm, onto the sample. The angle of incidence on the mirrors is estimated to be $2° \pm 0.5°$ from normal, with a 100 mm radius of curvature on the second mirror. Using a knife-edge measurement at the sample plane, the EUV focus is measured to be 2 μm $\pm$ 0.5 μm in diameter. A scanning electron microscope (SEM) image of sample is shown in the inset of Fig. 8.1. The sample, placed at the focus and perpendicular to the EUV beam, is a zone plate with 150 nm-thick polymethylmethacrylate (PMMA) rings on a 50 nm silicon nitride window. The sample was scanned in an 11×11 rectilinear pattern with nominally 0.88 μm between adjacent positions. A random offset of $\pm20\%$ of the step size is added to each scan position to prevent periodic artifacts from being introduced by the scan grid itself [154]. At each scan position, the EUV light scattered by the sample is detected on back-illuminated charged-coupled device (Andor iKon) with an array of 2048 x 2048 square 13.5 μm pixels placed 22.6 mm $\pm$ 0.2 mm from the sample. Each recorded diffraction pattern is two accumulations at 4.25 second exposure time, with 2×2 binning on-chip, at a 1 MHz pixel readout rate. After collection, and after the on-chip binning, the diffraction patterns were cropped to 900×900 pixels. A representative diffraction pattern, including stray HHG light that bypassed the multilayer mirrors, is shown in

Fig. 8.1. The sample was scanned in the top-right quadrant, such that the strongest diffracted light scattered along the diagonal of the detector, thereby maximizing the numerical aperture (NA) of the microscope. The scattered light was detected at an NA of 0.54 corresponding to an Abbe diffraction limited resolution, Δr, given by Eq. 8.1, where λ is the wavelength, and NA is the numerical aperture.

$$\Delta r = \frac{\lambda}{2\ NA} = 12.5\ nm \pm 0.2\ nm \qquad (8.1)$$

There are many ways to employ the novel modulus enforced probe (MEP) methodology. In the first method, depicted in Fig. 8.2, the sample is moved out of the EUV beam path, and a single image of the direct illumination is collected under the same, or similar, experimental conditions as the ptychographic dataset. The collection of the direct, un-scattered beam, can be carried out before or after the acquisition of the ptychographic dataset. In a reflection geometry, rather than the transmission geometry presented in this work, a measurement of the specular reflection off of a smooth surface can be used as the un-diffracted beam. Unlike the transmission geometry, where no information about the sample is needed for quantitative imaging, in a reflection geometry the reflectance of the surface is needed to scale the beam data for quantitative imaging. However, it is possible and has recently been demonstrated for quantiative analysis of buired layers [179]. The data for the MEP constraint can be obtained by separating the DC (zero-order diffraction) from the rest of the scatter pattern. This last method is especially effective when the sample is too large to be removed from the beam path or the ptychographic dataset has already been acquired and no measurement of the direct beam was taken. The third approach is used in this demonstration and discussed in detail in the following section.

8.3   Intensity assignment to the extracted zero-order diffraction peak

While removing the sample and collecting the direct beam is the most straight forward of the MEP methodologies (Fig. 8.2), a measurement of the raw beam without the sample was
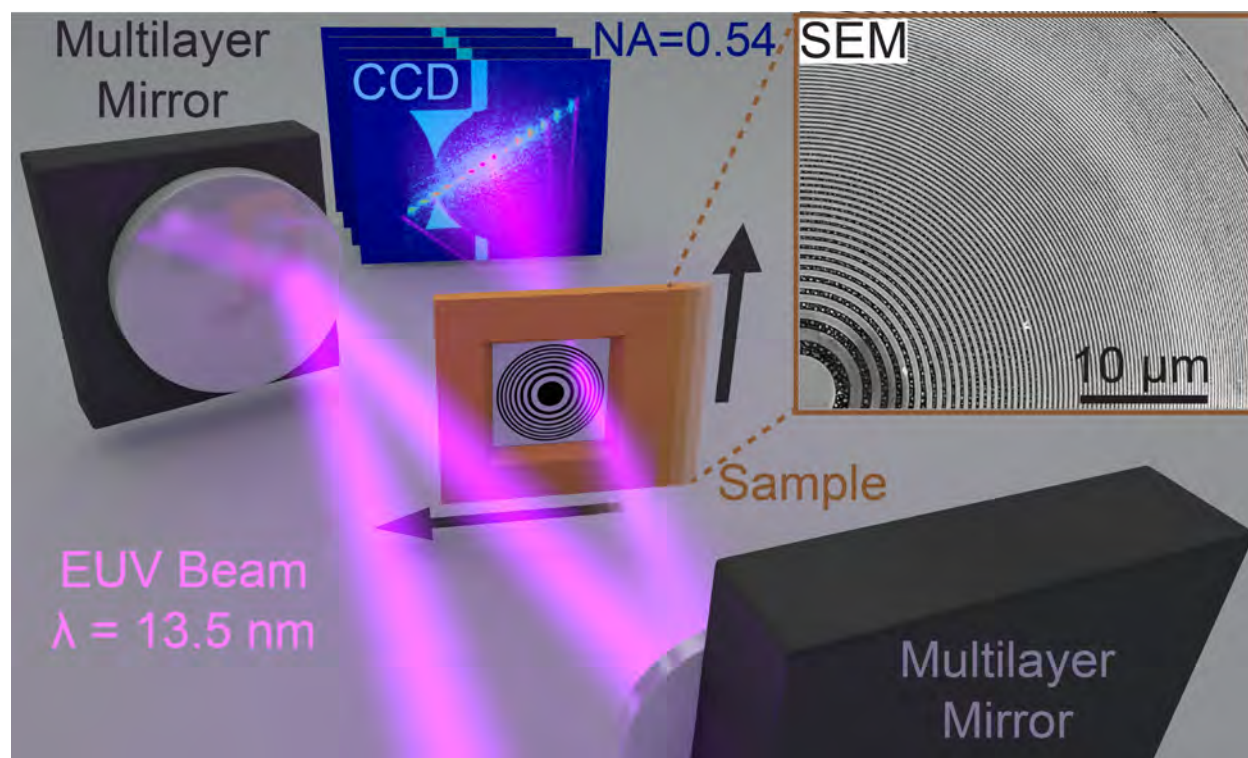
Figure 8.1: **Modulus enforced probe coherent EUV microscopy** A 13.5 nm harmonic beam is selected and focused, using a pair of multilayer mirrors, onto a zone plate sample. The sample is raster scanned and the scattered EUV is collected on a charged-coupled device (CCD) at a numerical aperture, NA, of 0.54. In addition to scattered light from the sample, some background light is also recorded on the CCD. The inset shows a scanning electron microscope (SEM) image of the sample's upper right quadrant, where the EUV data was collected.

not taken under the same experimental conditions as the ptychographic dataset in this work. It was only during post-processing that a new constraint was discovered to improve convergence and image quality. To apply the MEP constraint without the collection of the un-scattered beam, the zero order, or DC component, of the diffraction patterns must be extracted from the dataset. Furthermore, for quantitative imaging the correct intensity must be assigned to the isolated DC peak.

The un-diffracted beam is extracted using a three step process. First, to wash-out sample dependent features, the mean of the ptychographic dataset is computed. Then the diffraction peaks are isolated by thresholding at 30% of the maximum value. And finally, the DC peak is spatially isolated from the other peaks. The isolation of the DC peak is not necessary in the case of weakly scattering objects. With weakly scattering objects, the DC peak may be extracted by only thresholding. In experiments with photon flux that may cause damage to the detector, such as x-ray sources at free-electron laser facilities, weakly scattering objects can be used to attenuate the beam.

After extracting the DC peak, the correct intensity must be assigned to for quantitative imaging. If the average transmission of the sample is known, this information may be used to scale the DC peak. Alternatively, if the flux of the input beam is known, this information can also be used to scale the DC peak. The latter technique is used in this work.

The flux of our HHG beam is frequently monitored by recording the maximum count on the same detector used for data collection without any samples in the beam path. The camera setting for the max count measurement had the following settings: 2×2 binning, one accumulation, 0.1 second exposure, and 3 MHz readout rate. This resulted in a maximum count value of 23,550 after subtracting the offset from the camera's analogy-to-digital converter. The maximum count in extracted DC peak was scaled to match the maximum count of our flux measurement after adjusting for differences in camera settings. After adjusting the max count for differences in exposure time and accumulations, the max count assigned to the DC peak is $2,119,500$. The extracted and scaled DC peak is shown in Fig. 8.2 as if it were collected with the sample removed.
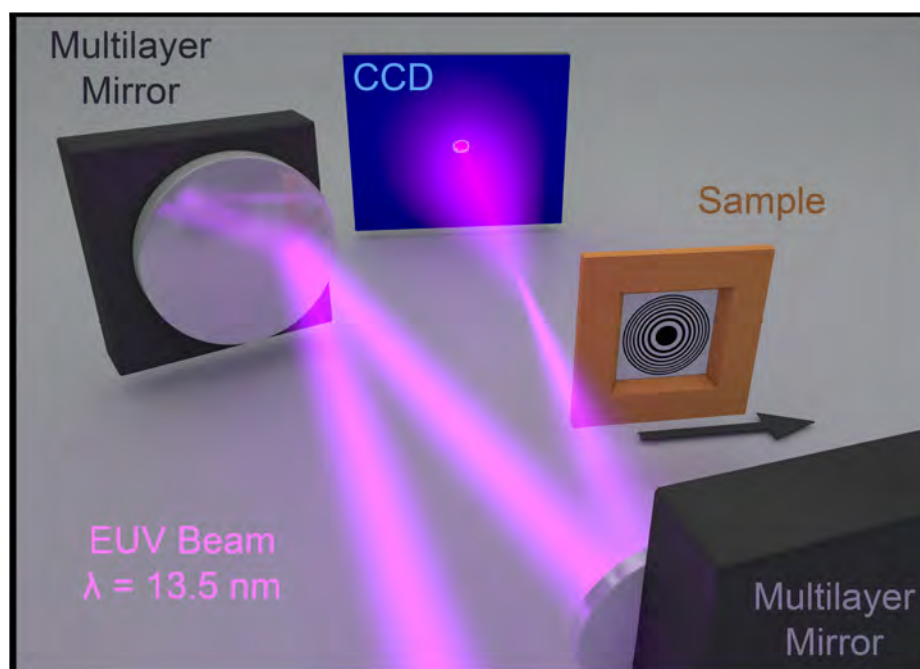
Figure 8.2: **Modulus enforced probe methodology** The modulus enforced probe constraint uses the direct beam as a constraint in the ptychography algorithm. One strategy to obtain the un-scattered beam is to move the sample out of the beam path, either immediately before or after the ptychographic data collection, and record the direct beam. Another strategy is to isolate the zero order weak from the collect ptychographic data set. The latter is employed here and the zero order peak is depicted on the detector.

8.4   Sub-wavelength coherent imaging of extended near-periodic objects

After collection of the ptychographic dataset and the extraction of the zero-order diffraction as the MEP constraint, intensity images are reconstructed using the ePIE algorithm [150] with and without the MEP modification. Sub-regions of reconstructed intensity images of the zone plate are displayed in Fig. 8.3, with the full reconstruction displayed in Appendix D. As a reference for image quality, a scanning electron microscope (SEM) image is shown in Fig. 8.3a. The reconstructed image with the MEP constraint, Fig. 8.3b, is of much better quality than the image without the MEP constraint, Fig. 8.3c, and compares favorably with the SEM image in the same region. The inverted contrast between the SEM image and the ptychographic images is a result of the different imaging geometries; the SEM image was taken in a reflection geometry and the ptychography data was obtained in a transmission geometry.

Imaging periodic samples represents a major challenge in traditional ptychographic CDI, due to the lack of diversity in the diffraction patterns, resulting in poor convergence and artifacts. Although the width of the PMMA zone plate rings have a radial dependence proportional to $1/r$, with $r = 40\mu m$ being the radius of the outer-most ring, the rings within the $5.65\mu m \times 5.65\mu m$ area, shown in Fig. 8.3, constitute a quasi-periodic arrangement of lines. When the MEP methodology is not applied, Fig. 8.3c, artifacts, as indicated by stripes and rapid oscillations, are present in the image. On the other hand, with application of the MEP constraint, Fig. 8.3b, the artifacts are either removed or reduced.

The insets of Fig. 8.3, show the periodic arrangement of 8 PMMA lines with 110 nm $\pm$ 10 nm width spaced by 90 nm $\pm$ 10 nm of Si_3N_4. To determine if the reconstruction resolution is consistent with the numerical aperture (NA) of the collected diffraction patterns, a lineout across a zone plate PMMA feature is analyzed with and without the MEP constraint. The location of the lineouts are shown by the lines inside the insets of Fig. 8.3b,c. The profile of the PMMA features are shown in Fig. 8.4a. The profile with MEP is shown by blue circle data points and was fitted to an error function. The 10% - 90% width of the fit (r-square better than 0.97) is approximately

6 nm and is better than our reconstruction pixel size, dx, given by

$$dx = \frac{\lambda \, z}{N \, px} = 12.6 \; nm \; \pm \; 0.2 \; nm \tag{8.2}$$

where λ is the wavelength, z is the distance from the CCD to the sample, N is the number of pixels on the detector, and px is the effective pixel size with on-chip binning. The agreement between the 12.5 nm Abbe limit from the numerical aperture (NA) of the collected diffraction patterns and the 12.6 nm resolution supported by the lineout of the zone plate feature, with the MEP constraint, substantiates that the algorithm was able to converge to a solution limited only by the NA of the data, and demonstrates sub-wavelength EUV imaging for the first time.

Due to the presence of artifacts in the image without the MEP constraint, 10 parallel and adjacent profiles were averaged for the lineout analysis. The orange square data points in Fig. 8.4a correspond to the lineout without MEP. The lineout is fitted to an error function (r-squared better than 0.98) and the 10% - 90% values of the fit support a 60nm resolution.

In addition to the sub-wavelength resolution of 0.9λ with the MEP constraint, we can also obtain three-dimensional topographical information from the phase image as shown in Fig. 8.4b. To create the topographic image from the phase (shown in Appendix D), the phase information must be converted to a physical thickness. The intensity image of the zone plate, inset of Fig. 8.3b, is used to create two binary masks: a mask for the PMMA features and a mask for the Si_3N_4 substrate. To separate the two materials, a threshold of $\frac{1}{3}$ of the theoretical transmission of Si_3N_4 [180] is used to separate the materials. The phase of the Si_3N_4 was fitted to a 2nd order plane, using a non-linearly least squares routine, and the fitted phase plane was subtracted from the entire phase image. Phase values below $-\pi$ are wrapped around to lie between $-\pi$ and π. Within the PMMA features, values less than $3\times$ the standard deviation of the substrate were increased by π to unwrap the phase. With the flattened and unwrapped phases, the thickness is calculated using the reported index-of-refraction values of PMMA for 13.5nm radiation [180]. The resulting 3D image is interpolated onto a $4\times$ larger grid and the vertical scale is scaled by $\frac{1}{5}$. The height of the zone plate features are calculated to be $180 \; nm \pm 40 \; nm$.
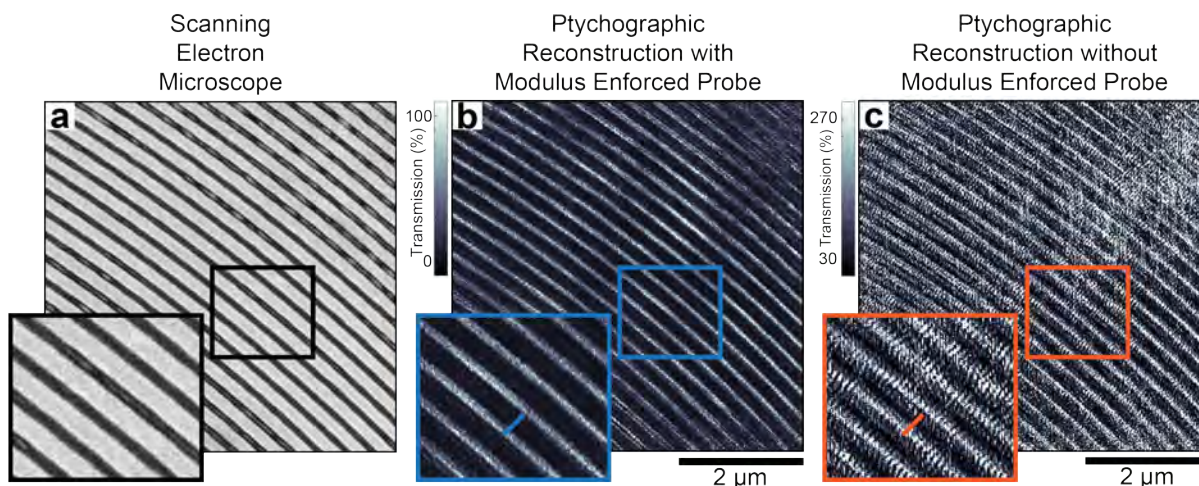
Figure 8.3: **Record sub-wavelength resolution imaging using 13.5 nm light and Modulus Enforced Probe** a) Scanning Electron Microscope (SEM) image of the zone plate sample. b) Intensity image from the ptychographic reconstruction, in the same region as the SEM image, obtained with the novel Modulus Enforced Probe constraint. The use of the MEP constraint results in quantitative transmission values of the sample. c) Ptychographic reconstruction without the MEP constraint results in degraded reconstruction quality and unphysical transmission values. Due to the contrast mechanisms of the SEM in a reflection geometry, the contrast of the SEM image is inverted with respect to ptychographic images obtained in a transmission geometry. The insets show a zoomed in region of the image and the lines within the inset indicate the location of the knife edge test, shown in Fig. 8.4.
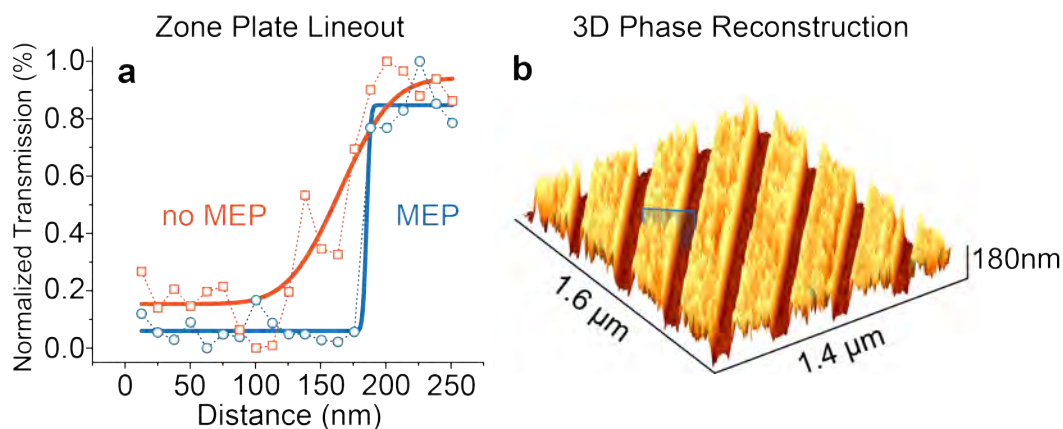
Figure 8.4: **Zone plate PMMA feature lineout and topographic image** a) The lineouts of a PMMA feature along the lines shown in the insets of Fig. 8.3a,b. The blue and orange data points, with error-function fits (solid lines), correspond the images with and without the MEP constraint. The distance between the 10% - 90% values of the MEP constrained lineout fit supports sub-wavelength resolution at 12.6 nm . b) Topographic image obtained by converting the phase image, with the MEP constraint, to height using the PMMA index-of-refraction. The vertical scale bar has been scaled by 1/5 and the image has been interpolated unto a 4× larger grid. The blue plane shows the location of the lineout in (a).

An important implication of the MEP constraint is quantitative imaging as shown in Fig. 8.3b. Quantitative reconstructions allow for materials to be identified and has been used to investigate oxide formation in buried structures [179]. Without the MEP constraint, power in the algorithm is allowed to flow between the object and probe, which can lead to unphysical transmission values as seen in Fig. 8.3c. The average transmission value of the 50 nm thick Si_3N_4 region (bright areas in the inset of Fig. 8.3b) is 0.44 $\pm$ 0.2. This transmission value is lower than the tabulated value, 0.65, reported in Ref. [180]. The difference may be explained by the incomplete liftoff of the PMMA, as can be seen in the SEM images of the sample shown in Fig. 8.1 and Fig. 8.3a.

The discrepancy between the tabulated and reconstruction values of the 150 nm thick PMMA regions (dark areas in the inset of Fig. 8.3b) are larger than the Si_3N_4 discrepancy. The tabulated value of PMMA is 0.46 [180] compared to 0.05 $\pm$ 0.04 in the reconstructed image. While the reconstructed transmission of PMMA is inconsistent with the tabulated value, the reconstructed value is consistent with a transmission measurement of the zone plate using the same setup for the ptychographic data collection. The transmission measurement was performed near the central disk of the zone plate and not the upper-right quadrant where the ptychography scan was performed. The mismatch in transmission values was noticed only after the data collection, otherwise the transmission measurement would have been in the same location as the ptychography scan.

The transmission measurement was performed as follows. Keeping all the detector settings the same, a diffraction pattern is collected with and without the zone plate in the beam. The transmission of the zone plate, after the subtraction of detector readout noise, is the sum of the diffraction with the zone plate divided by the sum of the diffraction without the zone plate. The calculation of the transmission, including both the PMMA and Si_3N_4, yielded a value of 10.9%. To determine the transmission of PMMA, the SEM image, shown in Fig. 8.1, is used to determine the area occupied by PMMA vs. Si_3N_4 near the central disk. The result of the PMMA transmission calculation is 0.05 $\pm$ 0.03, with the uncertainties coming from the threshold value used to separate PMMA and Si_3N_4 in the SEM image, uncertainties in the beam size, and uncertainties in the

location of the measurement. Further exploration of the low transmission of PMMA is beyond the scope of this work, but possible reasons include the sample's age and its storage. The sample was purchased in 2004, was stored in atmosphere, exposed to room lights, and contaminated with dust because it was not stored in a clean room environment. To summarize, the transmission values obtained with the MEP methodology, in contrast to unphysical values obtained without MEP, are reasonable and consistent with experimental transmission measurements.

The MEP constraint enables unique capabilities for periodic object reconstructions by minimizing the cross-talk between object and probe. The minimization of cross-talk, or decoupling between the probe and sample reconstructions, are seen by comparing the reconstructed probes shown in Fig. 8.5. The reconstructed probe with the MEP constraint (Fig. 8.5a,b) is smooth and continuous, while without the constraint (Fig. 8.5c,d) the probe is of poor quality. The poor quality probe leads to a poor quality sample reconstruction because the ptychography algorithm's reconstruction of the sample is dependent on the probe (and visa-versa). The lack of diversity in the diffraction patterns from periodic objects means less information for the algorithm, and may lead to poor decoupling of the object and probe, as seen in this work. Therefore, additional information introduced by the MEP constraint is especially important in reconstructing the probe from periodic samples.

The additional information from the MEP constraint leads to quantitative reconstructions because the MEP constraint eliminates the transfer of power between the sample and the illumination. In ptychography without the constraint, the power of the exit-surface wave, or product of the sample and illumination, is fixed by the power in the measured diffraction. As a result, power is able to flow, inside the algorithm, between probe and sample because the product is unaffected, leading to unphysical transmission values as seen in Fig. 8.3c. The MEP constraint eliminates this transfer of power, because the power of the probe is enforced in addition to the diffraction measurement. Therefore, the reconstructions of the sample and illumination are quantitative (Fig. 8.3b).

With the exception of the MEP constraint, the reconstructions procedure is identical. The
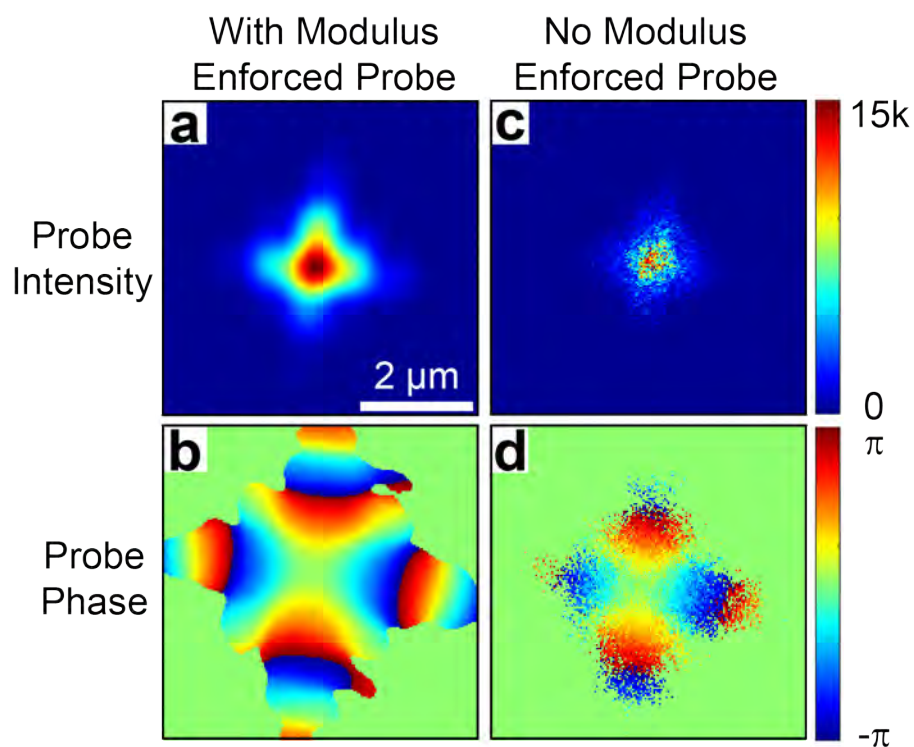
Figure 8.5: **Minimization of cross-talk with the modulus enforced probe constraint** a) The intensity and b) the phase of the 13.5 nm illumination (probe) at the sample plane with the Modulus Enforced Probe (MEP) constraint. The probe is smooth and continuous and is in contrast to c) the intensity and d) the phase of the illumination without MEP. Without the MEP constraint, there is cross-talk, or poor decoupling, between the illumination and sample reconstruction, Fig. 8.3c, leading to artifacts and degraded image quality. The probe intensity is shown in detector counts and the scale bar in (a) applies to all the panels.

Table 8.1: **Reconstruction parameters**

	Total Iterations	Probe Updates	Position Correction
Stage 1	950	100-950	No
Stage 2	700	100-700	No
Stage 3	10,000	2000-9000	No
Stage 4	10,000	2000-9000	2-9000

reconstruction was done in four stages using the ePIE ptychography algorithm [150] on a Nvidia GPU (Tesla k-40). The initial probe guess for the algorithm was generated by modelling the optical components in the beamline; the initial object guess was unity. In the first two stages a binary mask was used to block the stray background light during the modulus constraint; the modulus constraint was not applied in the background region, instead the values were set to zero.

Table 8.1 summarizes the parameters of the four reconstruction stages. After completion of the first stage, the updated probe was used as the initial probe guess for stage two; the object was re-initialized to unity. Stage three began in the same manner as stage two, with the updated probe from the end of stage two as the initial probe guess and the object re-initialized to unity. In stage three, principles discussed in Ref. [181] were used to let the algorithm fill in data in the masked-off background region. In other words, the modulus constraint was not enforced in the stray background region and the algorithm filled in these regions. Finally, in stage four, both the probe and object at the end of stage 3 are used as the initial guesses. As in stage 3, the algorithm was allowed to extrapolate values in the background region. During this last stage, position correction, as described in Ref. [170], was performed. The reconstruction as the end of stage four are shown in Fig. 8.3, Fig. D.1, and Fig. D.2.

8.5   Implementation of the Modulus Enforced Probe Constraint

The ptychography algorithm, as described in sec. 6.3, solves for both the object and the probe from a set of diffraction measurements. With one additional measurement of the un-diffracted illumination, a powerful constraint is possible. This novel constraint is termed Modulus Enforced

Probe (MEP) and the general working principle is displayed in Fig. 8.6.

It is assumed the probe does not change during the scan. If the sample is removed from the beam path, either immediately before or after the ptychographic data collection, a direct measurement of the probe, $\mathcal{P}_j(\vec{u})$, can be recorded on the detector, which is given by

$$\mathcal{P}_j(\vec{u}) = |\mathfrak{F}[P(\vec{r} - r_j)]^2|. \tag{8.3}$$

Following the notation in 6.3.2 and 6.3.3, $\vec{u}$ is the spatial frequency vector at the detector plane, $\mathfrak{F}$ is the propagator from the sample to detector plane, $\vec{r}$ is the spatial coordinate vector at the sample plane, r_j is the shift for position j, P is the amplitdue of the probe at the sample plane, and $\mathcal{P}$ is the intensity of the probe at the detector plane. The MEP constraint utilizes the measured probe on the detector, $\mathcal{P}_j(\vec{u})$, to constrain the guess of the probe in the ptychography algorithm. While the implementation of MEP has not been investigated in all versions of ptychography, for example see [149, 154, 156–158], here it is implemented as a modification to the ePIE algorithm [150]. The constraint is introduced after the probe update function given by Eq. 6.13 in 6.3.3 . The updated probe, $P_{Gj+1}(\vec{r})$, is propagated to the detector plane forming a guess of the probe on the detector given by, $P_{Gj}(u) = \mathfrak{F}[P_{Gj+1}(\vec{r})]$. Here, we apply a modulus constraint to the probe guess enforcing the measurement

$$P_{Mj}(\vec{u}) = \sqrt{\mathcal{P}_j(\vec{u})}\frac{P_{Gj}(u)}{|P_{Gj}(u|} \tag{8.4}$$

This modulus constrained probe guess, $P_{Mj}(\vec{u})$, is propagated back to the sample plane forming a further updated probe guess

$$P'_{Gj+1}(\vec{r}) = \mathfrak{F}^{-1}[P_{Mj}(\vec{u})] \tag{8.5}$$

which is consistent with the measured probe at the detector. The new probe guess, $P'_{Gj+1}(\vec{r})$, is now fed back into the algorithm. This additional constraint to the probe is analogous to the error-reduction (ER) algorithm as described in by Fienup [119], but instead of using ER to solve for the object, it is used within the ptychography algorithm to further constrain the probe guess. In this work, a simple version to enforce the probe measurement is used, but more advanced algorithms
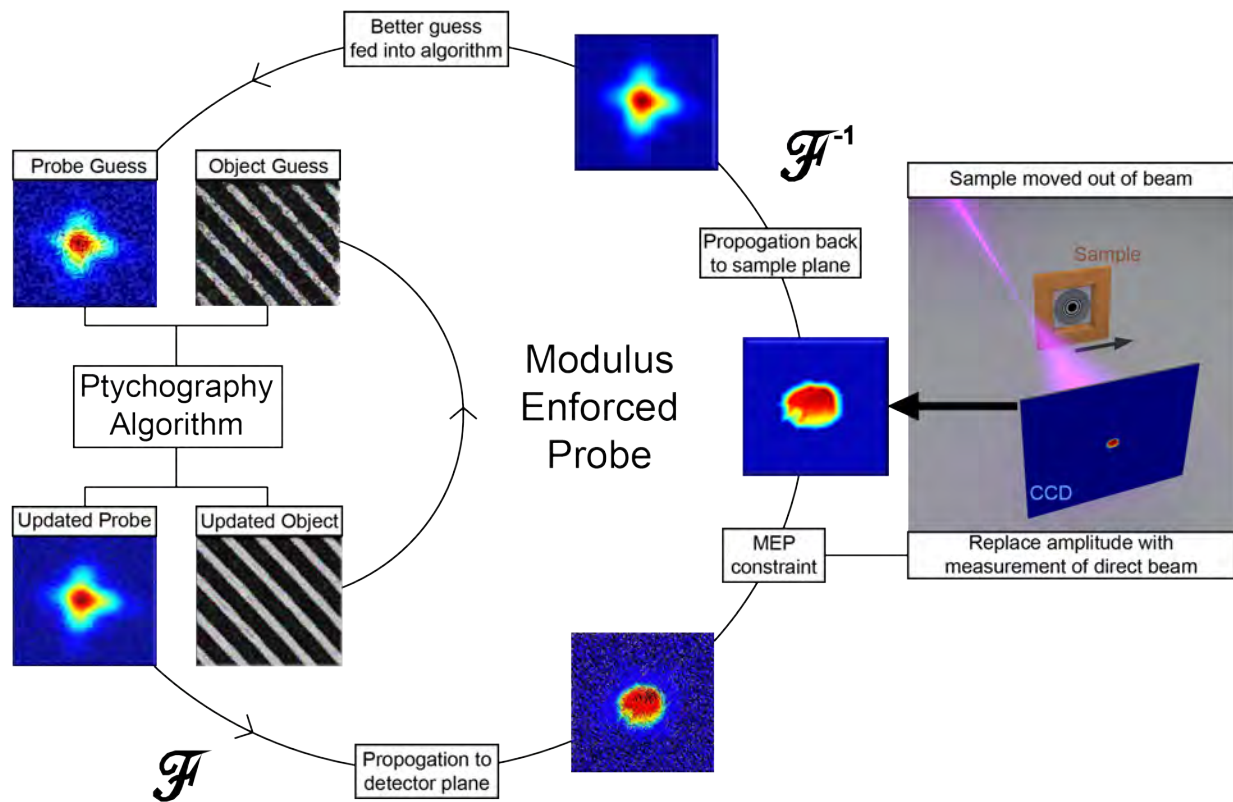
Figure 8.6: **Modulus Enforced Probe implementation within ptychography algorithm** The updated probe from the ptychography algorithm is further constrained with measurement of the un-diffracted probe. First, the update probe is propagated to the far field. In the far field, the amplitude is replaced with the measured amplitude. Then the probe is inverse transformed back to the sample plane and feedback into the ptychography algorithm. This sequence of steps is the modulus enforced probe implementation with the ptychography algorithm.

such as hybrid input-output [120], or relaxed averaged alternating reflections (RAAR) [134] can be used.

8.6   Modulus Enforced Probe Simulations

In this section, the effects of the MEP constraint on convergence, initial probe guesses, and noise are explored using simulated data. The simulation parameters are given in Table 8.2 and were chosen to follow the experimental conditions. The complex-valued sample, for the simulation, was composed of open-source test images[2] ; the amplitude and the phase are shown in Fig. 8.7a and Fig. 8.7b, respectively. The simulated probe, also shown in Fig. 8.7a,b, consists of a Gaussian profile with a $1/e$ width (σ) equal to 2μm. The probe has a hard edge at $r = 2\mu$m and one Fresnel zone of phase curvature. The 7×7 scan positions, with $r/3$ step size, are shown as green dots on the amplitude of the sample (Fig. 8.7a), with the total reconstruction area outlined in green. The simulation uses the ePIE algorithm as described in Ref. [150]. There is no sub-pixel shifting, instead the shift is rounded to the nearest pixel. The alpha and beta feedback parameters are unity. The scan positions are called in the same order for each iteration. To propagate between the sample and detector, a normalized fast Fourier transform (FFT) is used [166, 167].

In the first simulated reconstruction, the initial guess of the probe is the probe used to simulate the ptychographic dataset; the initial object guess is unity. Three tests are performed: no probe updates, as well as probe updates with and without the MEP constraint. The results of the simulation are shown in Fig. 8.8 and Table 8.3. In Fig. 8.8 a plot of the root-mean-square (RMS) is shown, where the RMS error defined by

$$RMS = \sum_{j} \frac{\sqrt{\sum_n (|\Psi_j(u)| - \sqrt{I_j(u)})^2}}{M \times N} \tag{8.6}$$

where $\Psi_j(u)$ is the FFT of the exit surface wave, $I_j(u)$ is the intensity of the diffraction pattern on the detector, M and N are the dimensions of the grid, and j is the index of the scan position. Table 8.3 shows the total time of the simulation and the number of iterations to reach convergence.

---

[2] `https://commons.wikimedia.org/wiki/Main_Page` Tv resolution chart and Ishihara Test

Table 8.2: **Modulus Enforced Probe Simulation Parameters**

Wavelength	Sample-to-CCD	Probe Radius	Step Size	Gaussian Width
$\lambda = 13.5$ nm	$z = 22.6$ mm	$R = 2~\mu$m	$R/3$	$\sigma = 2\mu$ m

CCD pixel(no bin)	Binning	Scan Size	Number of Pixels (no bin)	Probe Update
$px = 13.5~\mu$m	2×2	7×7	256×256	iteration 10

The times of the simulation can be greatly improved by using GPU computing, as done in the experimental results above. However for these simulation, the reconstructions were done on a single Intel CORE i5 CPU.

The reconstruction converges in fewer iterations with the MEP constraint, but the additional FFTs needed for the MEP constraint result in a longer per iteration time. The combination of fewer iterations to converge and a longer per iteration time nearly balance out; it took 2% longer, it time, to converge with the MEP constraint than without it. In future work, the MEP constraint does not need to be applied at each iteration nor each position of each iteration. Instead, the MEP constraint could be applied to some subset of the iterations or scan positions. Further simulations are needed to find the balance between convergence in fewer iterations and faster iterations times. Furthermore, the feedback parameter on the probe udpates, β [150], can be increased with the MEP constraint as discussed in the simulation sections of [173], and leads to even faster convergence.

The next test uses random initial probe guesses cropped to three radii: $r = 1\mu m$, $2\mu m$, and $3\mu m$. Both the amplitude and phase of the initial probe guesses are random with the amplitude values between 0 and 1 and the phase values between $-\pi$ and π. The results of this simulation are shown in appendix D.3. With the MEP constraint the algorithm still converges, even with the random guesses of the probe. This suggests that as long as the diffraction patterns are properly sampled, no knowledge of the probe is needed at the sample plane with the MEP constraint; the far-field information of the probe is sufficient for the algorithm to converge. On the other hand, without the MEP constraint, the algorithm will not converge with random guesses.

The effects of additive white Gaussian noise are also investigated. The addition of white
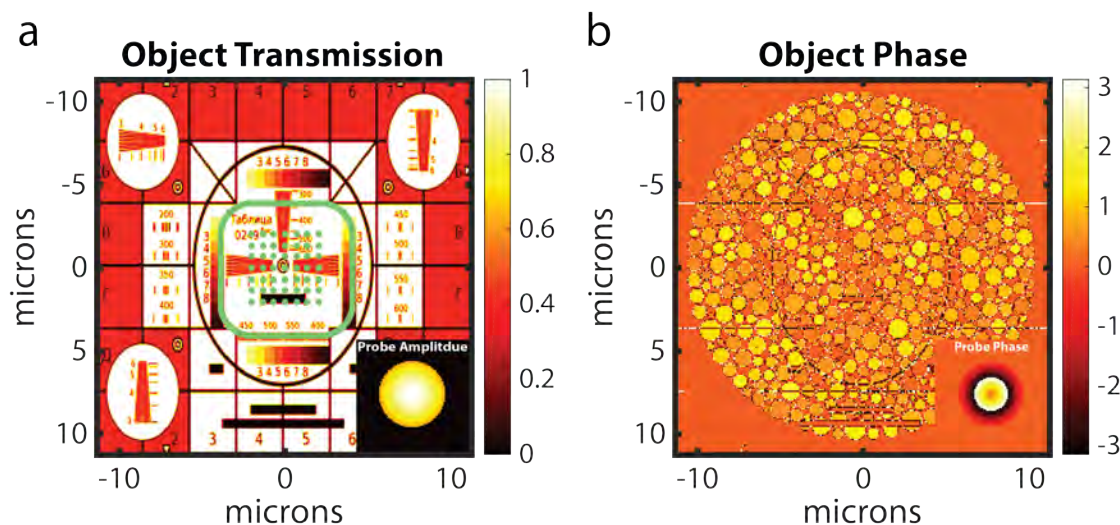
Figure 8.7: **Ptychography with MEP: simulated sample** a) The amplitude and b) phase of the complex-valued simulated sample. The green dots on shown in (a) indicate the scan positions used to simulate the ptychographic dataset. The green outline shows the area scanned by the probes. The insets in (a) and (b) show the simulated probes amplitude and phase.
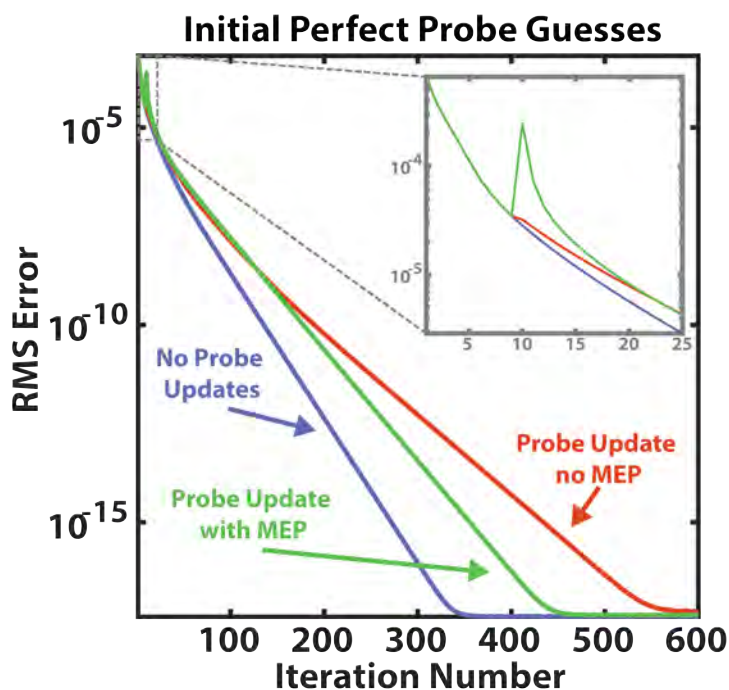
Figure 8.8: **Perfect Initial Probe Guess Simulated Reconstruction** In this test, the initial probe guess is the probe used to generate the simulated data. The plot shows the root-mean-square error of the reconstruction as a function of iteration. The algorithm converges faster with the MEP constraint than without it.

Table 8.3: **Few iterations to converge with MEP**

	Total Iterations	Total Time(s)	Time per Iteration(s)	Iterations to Converge	Time to Converge(s)
No Probe Updates	600	165	0.275	372	102
Probe Updates	600	193	0.322	583	188
Probe Updates w/ MEP	600	246	0.410	469	192

Gaussian noise reduces the ratio of signal to noise ratio (SNR) and two SNR values were simulated: 100 dB and 50 dB. The noise was added to the simulated diffraction patterns. In both cases, the ptychography algorithm with the MEP constraint reached a lower RMS error than without the MEP constraint as shown in appendix Fig. D.4. The MEP constrained algorithm reached 83% and 85% better RMS error for the 100 dB and 50 dB SNR simulations.

8.7   Conclusion

By applying the novel modulus enforced probe technique (MEP), a spatial resolution of $0.9 \times \lambda$ was demonstrated on an extended, quasi-periodic object using 13.5 nm illumination. Without the MEP constraint, the resolution is lower, 60 nm, and suffers from cross-talk between the object and the probe leading to a poor quality image. With the MEP constraint, the achieved 12.6 nm $\pm$ 0.2 nm spatial resolution is in agreement with the theoretical Abbe resolution of 12.5 nm $\pm$ 0.2 nm corresponding to the numerical aperture. To my knowledge, this is a record resolution-to-wavelength ratio for any EUV or x-ray full-field image of an extended object. Moreover, this work is the first high-quality image of a periodic sample using a coherent diffractive imaging.

Ongoing research in ptychography, including imaging with multiple colors [182–184], under-sampling [185,186], and thick samples [187–190], will all benefit from the from the MEP constraint because the addition information introduced. In these ongoing efforts, the algorithm is tasked with solving form more than just a single sample and illumination, thus the additional information from the MEP constraint reduces the number of unknowns in the algorithm.

As the techniques presented here are scalable, illumination with shorter wavelengths, either with tabletop high-harmonic sources or large-scale synchrotrons and x-ray free electron lasers, can

enable nanometer, or even atomic scale resolution, of a broad range of next-generation electronics such as semiconducting chips and data storage devices.

Chapter 9

Stroboscopic Imaging of Thermal Transport in Nanostructures

The fastest processes at the nanoscale, such as heat transport [191], shock waves in plasma [192], and ultrafast magnetization [193, 194], happen at the picosecond (ps) to femtosecond (fs) time scales. Optical pulses have made it possible to temporal resolve dynamics at these timescales, but the spatial resolution of these wavelengths are not sufficient to image the nano scale features directly. Thus, to capture the fast dynamics and image the features simultaneous pulses of short wavelengths are employed [195].

Ultrafast electron microscopes have been developed [23, 24] an can achieve nanometer scale spatial resolution, with 100 fs temporal resolution. The ability to obtain shorter pulses mainly limited by space-charge effects and is an active area of research [25]. Complementary to ultrafast electron microscopes are pulsed sources of coherent EUV and X-rays. Without imaging, short pulses of x-rays were used to analysis the Airy diffractions of circular samples using model based approaches [196, 197]. Extreme ultraviolet lasers have been used, with their nanosecond (ns) pulses, to image an oscillating magnetic nano probe using Fresnel Zone plates [198] and, with Fourier transform holography, imaged a vibrating cantilever. Coherent diffractive imaging techniques have been employed ultrafast imaging of samples in a single shot [199, 200].

In this chapter, we explore stroboscopic imaging of micron to nanoscale structures using high-harmonic generation sources. As discussed in Ch. 4, the radiation from HHG maintains the temporal structure of the driving laser and is inherently synchronized in time with the IR driving laser making HHG the ideal source for tabletop pump-probe experiments. The IR light is used to

thermal excite the sample and the EUV, in combination with ptychographic coherent diffractive imaging (CDI), is used to image the sample with and without the excitation of the pump. The analysis of the images shows a 3 Å axial expansion of the sample when excited with the pump.

9.1   Pump-Probe Principles

In pump-probe experiments, the sample is excited with the pump and measured with the probe. It is critical that the pump pulses are synchronized with the probe pulses with little jitter between the pulses. Typically, this is accomplished by splitting a pulsed laser into a pump-arm and a probe-arm. The relative path length of each arm can be adjusted, enabling control over the arrival time of the pump and probe pulses. If the sample dynamics are reversible, then stroboscopic imaging is possible by taking snap shots of the sample at various pump-probe delays.

The timing of pump-probe pulses can be divided into three categories: positive time, time zero, and negative times. These different pumping schemes are depicted in Fig. 9.1. Positive time refers to instances where the pump beam reaches the sample before the probe. This allows the sample to be excited before the measurement by the probe. The simultaneous arrival of the pump and the probe is called time zero. At this instant, the beams are overlapped in time and the sample begins to be respond to the pump. Negative time occurs when the probe arrives before the pump. During negative time, the probe does not measure the pump's excitation of the sample.

9.2   Experimental Geometry

The temporal resolution of the this stroboscopic imaging system is on the order of femtoseconds, and is limited by the pulse length of our driving laser (21-24 fs). The timing between pulses is 200 μs, or 5kHz repetition rate, and is long enough to ensure the sample dynamics have relaxed before arrival of the next pump pulse [191].

Before the generation of harmonics, but after the beam stabilization mirrors, part of the driving laser is split off into a separate beam path called the pump-arm. The pump-arm is depicted in Fig. 9.2. It is critical that the pump-arm be split off after beam stabilization mirrors because
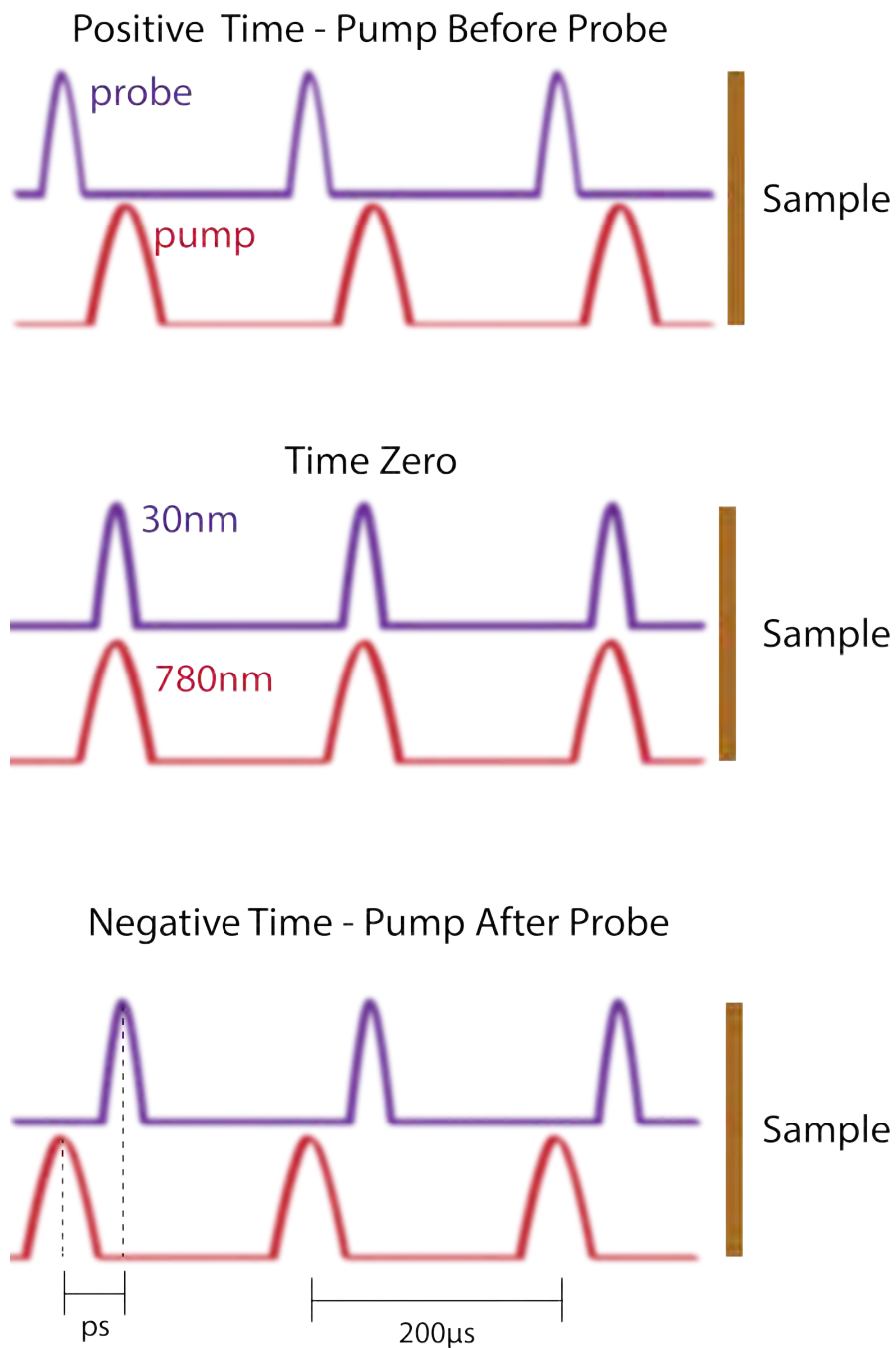
Figure 9.1: **Pump-Probe Timing** In a pump-probe experiment, the pump pulse excites the sample and then a probe pulse measures the excitation (positive-time). The simultaneous arrival of the pulses is time zero. When the pump arrives after the probe, the probe does not measure the excitation by the pump pulse (negative-time).

if not, the beam stability feedback will introduce spatial beam jitter or walk off. The driving laser is separated with a 70:30 beam splitter with low dispersion characteristics. The reflected beam is sent towards the high-harmonic waveguide (not shown in Fig. 9.2), while the transmitted beam travels through a half-wave plate and polarizer combination allowing for tunable pump fluence and polarization. The delay stage consists of two components: an Areotech ANT130 motorized linear stage with nanometer precision and a retro-reflecting mirror. The retro-reflector is carefully design to reflect the beam parallel to the input beam, but shifted laterally. The total distance of the pump-arm was designed to equal that of the probe arm when the delay stage is nearly at the end of its negative-time range. This alignment enables investigation farther into the positive time regime, allowing for more dynamics of the samples to be captured.

Before the pump beam enters the experimental chamber, through a sapphire window, a focusing lens is placed on a linear, micrometer-actuated, stage. The lens focuses the pump beam onto the sample plane. The stage allow the lens to be moved along the optical axis enabling fine control of the spot size on the sample which was fine tuned to ≈ 350 μm diameter. At the most negative-time delay position of the stage, the spot size is 385μm x 304μm. While at the other end of the stage, the most positive-time, the spot size is 393μm x 309μm. The change is spot size is due to slight misalignment of the delay stage, which causes the beam to point differently through the focusing lens. The sample is placed before the focal spot and the spot size is measured using a CMOS detector (Mightex S-series). After the lens, the pump beam is steered into the experimental chamber with an ultra-stable tunable mirror mount. This adjustable mirror mount enables fine adjustments of the pump beam, without altering the alignment through the focusing lens.

In the following experiments, the pump beam is the driving laser (780nm) and the probe beam is the high-harmonic radiation ($\approx$30nm) (Fig. 9.1). The pump beam is used to heat the sample before the arrival of the probe. The probe scatters off the sample and is recorded on a detector as depicted in Fig. 9.3. The camera used in the experiment is a Princeton Instruments in-vacuum camera with a back-thinned CCD. The CCD has a square array of 2048x2048 pixels, each with a side length of 13.5μm. The entire camera and readout electronics are placed inside
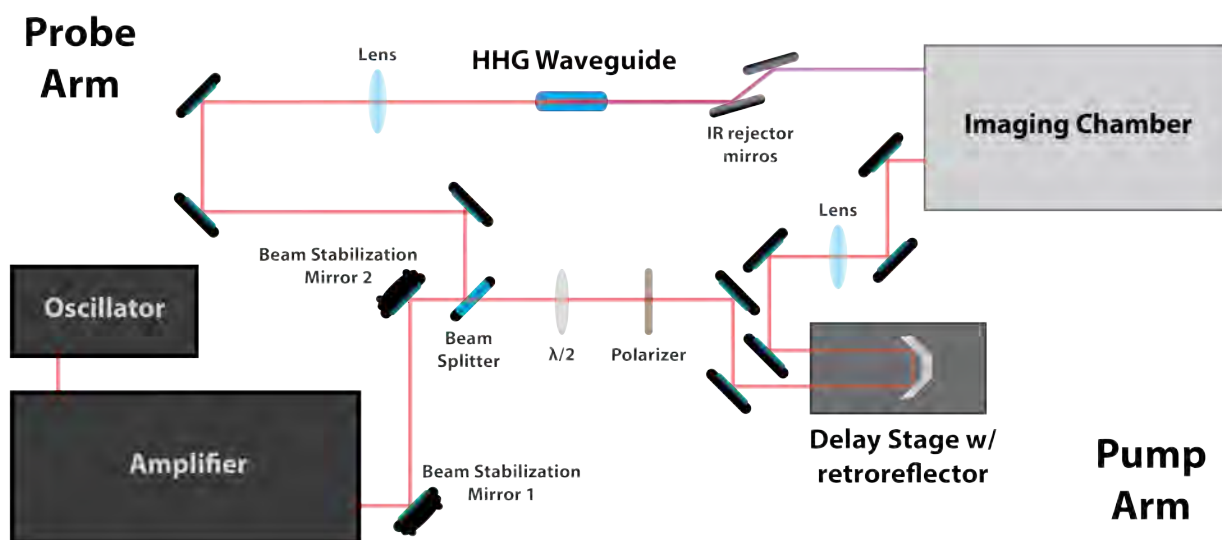
Figure 9.2: **Pump-Probe Schematic** After the beam stabilizing mirrors, the driving laser is split into two paths. One path, the probe arm, is steered towards the HHG waveguide. The other path, the pump-arm, is steered into a delay stage. Movement of the delay stage alters the path length enabling control of the pump-probe timing. A $\lambda/2$ wave plate and polarizer combination are used to adjust the pump fluence. A lens outside the experimental chamber focuses the pump onto the sample. The path length of the pump-arm is carefully designed to match the length of the probe arm and is not drawn to scale here.

the evacuated experimental chamber. Feedthroughs for electrical and cooling were installed. The chiller, used to pump a 50:50 mixture of distilled water and propylene glycol, was customized for low vibration pumping.

The pump beam at least 10^5 to 10^6 times brighter than the high-harmonic radiation, thus the camera will completely saturate or become damaged if the pump light reaches the CCD. To protect the CCD, and only measure the scattered EUV light, a 200nm thin aluminum filter, was installed over the CCD. The filter holder was designed to mount directly over the CCD and contained a baffling system for safe evacuation and venting of the chamber. As determined by recording a negligible increase in CCD background counts with a pump power of 1 W, the pump light is attenuated by at least 10^{-6}.

To ensure synchronization of the pump and probe pulses with the camera exposure, two in-vacuum shutters are adopted. In addition to these shutters, a third shutter is installed, labeled the "alternating shutter" in Fig. 9.3. This shutter is physical located outside by chamber, but is depicted inside for simplicity. The alternating shutter, as the name suggests, opens every-other exposure. Thus, when the data are collected there is a pump-on exposure, followed by a pump-off exposure. This is important during data analysis because the pump-off data acts as a control set. Changes from pumping should only be present in the pump-on exposure. Changes in the pump-off signal indicate some changes in the HHG beam or irreversible sample changes, such as melting or burning.

Before the ellipsoidal mirror shown in Fig. 6.3, a single harmonic from the HHG comb is selected using a pair of 45 degree angle-of-incidence SiC/Mg multilayer mirrors. The distance from exit of the waveguide to the center of the ellipse is 1500mm and the ellipse to focus distance is 100 mm. The sample is placed at the focus of the ellipse with a 3-axis stage. The HHG beam is incident on the sample at an angle of 62 degrees from the sample normal (28 degrees glancing) with the CCD placed 47.5mm from the sample and perpendicular to the specular reflection.
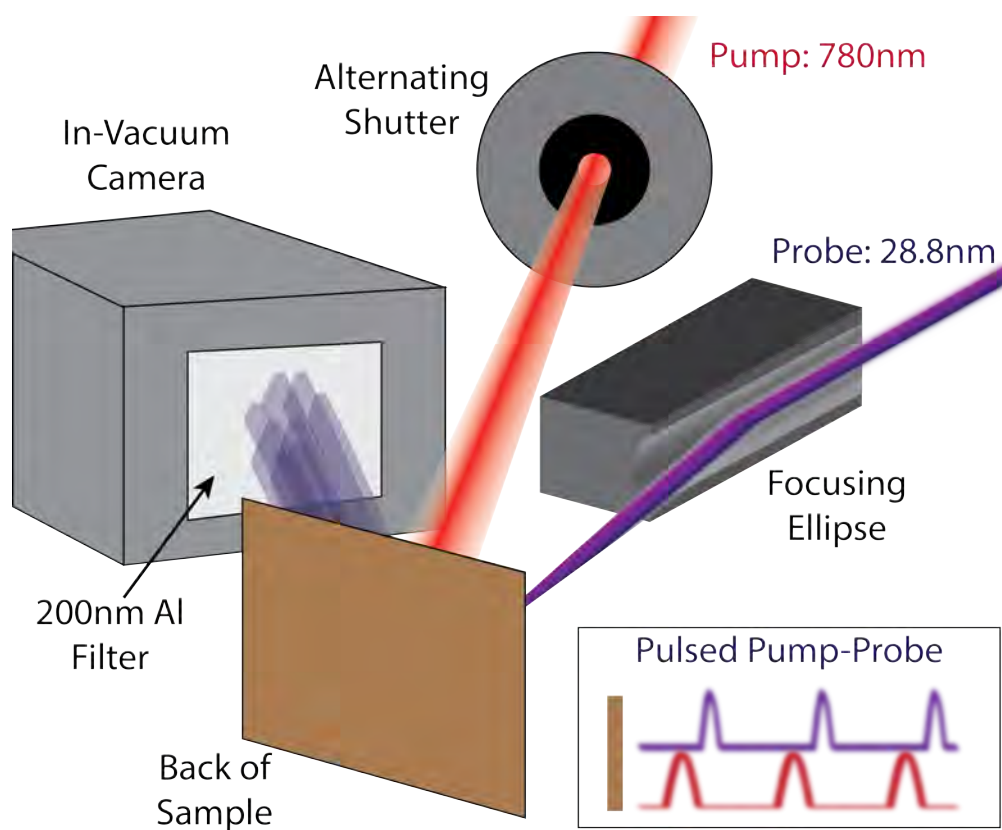
Figure 9.3: **The pump-probe experimental chamber** The HHG beam is focused onto the sample with an ellipsoidal mirror. The sample scatters EUV light onto the in-vacuum detector. The detector has a 200nm aluminum filter in front of the CCD to block the pump light. A shutter is used to alternatively block the pump; there is one measurement with excitation from the pump, followed by a measurement without excitation.

9.3 Experimental characterization of the Time-resolved ptychographic CDI microscope

The stroboscopic EUV microscope presented in this thesis is the first of its kind. Therefore, after its development, a series of tests was required to ensure its correct implementation. The verification of time zero is first done outside of vacuum with a Beta Barium Borate (BBO) crystal, a common nonlinear optical material, using the IR laser instead of the HHG radiation. With sufficient intensity, 150-300 mW, the IR light from the driving laser can frequency double inside the crystal. If two ultrafast beams are overlapped on the BBO crystal, non-collinearly, in both time and space, an additional cross-correlation signal is generated [201]. The cross-correlation signal is only present at time zero. Without generating high-harmonics, some of the driving light is passed through the probe arm, into the chamber, and off the ellipsoidal mirror. The sample, as shown in Fig. 9.3, is replaced with the BBO crystal. Finding the autocorrelation signal from the BBO in this manner, provides an estimate of the delay stage location corresponding to time zero.

After this step, a more precise estimate of time zero needs to be determined in vacuum, overlapping spatially and temporally the the HHG radiation from the probe path with the IR pump beam. To accomplish this, the spatial overlap in the chamber in vacuum condition is first determined with an external imaging system which consists of mirrors placed inside the chamber to relay light reflected off the sample out through a transparent viewport and into a telescopic lens system mounted on a CMOS detector. A LED white light is attached to a viewport on the chamber to illuminate the sample. The aluminum filter, mentioned in the previous section, mounted on the CCD blocks the white light from the LED, allowing real-time monitoring of the sample during data collection.

To visualize the HHG beam on the sample plane, a featureless area of the sample is coated with a thin layer of phosphorus. When the phosphorus is illuminated with HHG, it fluoresces in the visible spectrum which is detectable with the external imaging system. The pump light is also visible on the phosphorus, thus allowing the visualization of the overlap pump and probe in

vacuum, at the sample plane.

In vacuum, as discussed thus far, only the spatial overlap of the pump and probe beam have been accomplished. The next step is verifying temporal overlap. Verification of temporal overlap is achieved by detecting a time-dependent change in scatter from a calibration sample consisting a periodic array of lines, 500nm in width with a 75% duty cycle, composed of 8nm tall nickel features patterned on silicon. This sample scatters light into distinct orders as seen by a representative diffraction pattern shown in Fig. 9.4a.

The thermal response of this sample was reported in Ref. [191], where the dynamics occurred on the order of picoseconds. The dynamics of this sample include longitudinal acoustic waves (LAW) and surface acoustic waves (SAW). The LAW waves are the vibrations of the nanostructures after the rapid thermal expansion from the pump pulse. The SAW waves are acoustic modes that are confined to a very shallow penetration depths [202] and have been used to characterize the nanoscale properties such as the mechanical properties of thin films [203].

As the grating-like sample is rapidly heated by the pump beam, thermal expansion from the grating lunches LAW and SAW waves, which cause the relative height of the lines to change with respect to the substrate. The changing height of the grating causes a phase shift of the scattered light resulting in a change in the diffraction efficiency of the grating at the detector plane. The change is diffraction is quantified by

$$change\ in\ diffraction = \frac{(AC^+ + AC^-) - DC}{AC^+ + AC^- + DC} \tag{9.1}$$

where AC^+ and AC^- are the total power in the positive and negative first order diffraction peaks, and DC is the zero order peak. The peak regions used for the calculation are shown in Fig. 9.4a. This type of analysis have been employed previously to investigate the dynamics of surface acoustic waves and nanoscale heat transport [191, 202, 203].

In this work, the change in diffraction signal is used to verify the presence of a dynamic signal and is shown as a function of pump-probe delay in Fig. 9.4b. The figure shows the signal with and without the pump accomplished by switching of the alternating shutter (Fig. 9.3). The relatively
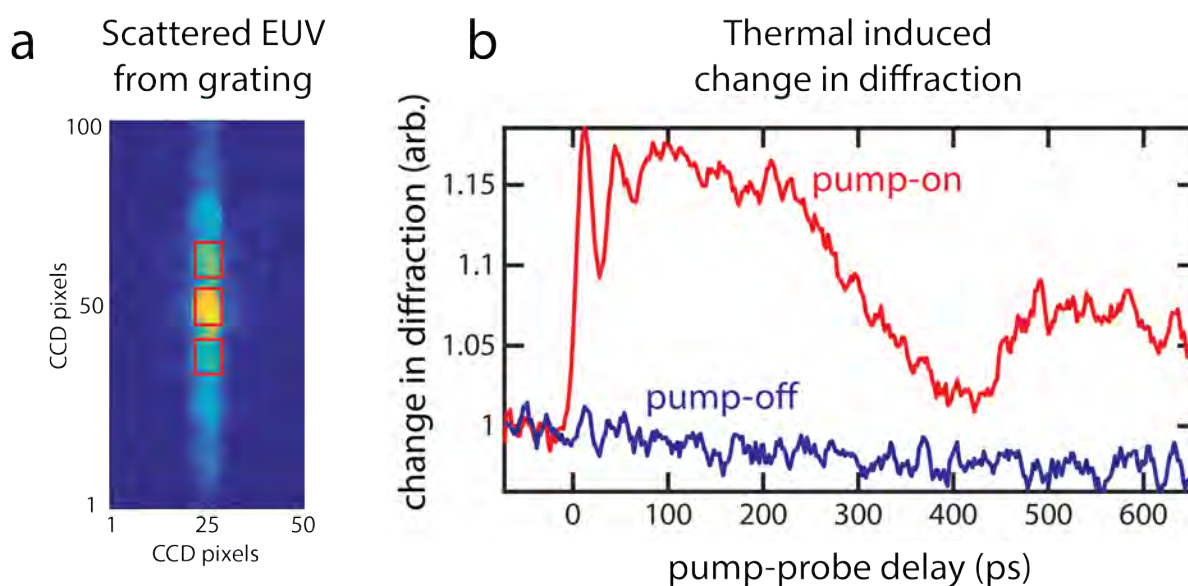
Figure 9.4: **Verifying time zero with a grating sample** a) Scattered EUV from a Ni grating sample. The grating sample scatters the EUV into distinct orders. The orders highlight with the boxes were used in the change in diffraction calculation, Eq. 9.1. b) The change in grating efficiency changes when the grating is heated by the pump light. The abrupt change in diffraction indicates the location of time zero.

flat pump-off signal compared to the pump-on, Fig. 9.4b, indicates the change in diffraction is due to heat expansion of the grating and not fluctuations in the HHG source. The abrupt jump in the pump-on signal is the location of time zero. The change in diffraction signal ensures that the pump and probe beams are overlapped in both space and time. Furthermore, the signal-to-noise ratio is similar to previously published work [191, 202], and both the LAW and SAW waves are visualized. The LAW waves are the rapid oscillations in the pump signal, see Fig. 9.4b, immedialty following time zero. The SAW wave is the longer period wave, and with our delay stage range, just over a full period was captured. With a more range, the SAW wave exponentially deceares and the heat from the sample disipates [202].

9.4 Dynamics from a gold circuit-like sample

The detailed characterization of the stroboscopic EUV microscope enbaled the investigation of the thermal response from a gold circuit-like sample, by means of time-resolved ptychographic CDI. The sample was fabricated using e-beam lithography on a silicon substrate and consists of 29 nm tall features of evaporated gold on a 5 nm titanium adhesion layer. [1]

A static ptychography scan is taken on the gold circuit sample. To prevent periodic artifacts [154], while maintaining uniform overlap of the sample, the scan follows a Fermat spiral trajectory [155]. The step size between positions is 2μm with a total of 197 positions. At each scan position, 3 accumulations, at 1 second exposure time, are acquired with 2x2 binning on chip. The static ptychography reconstruction is shown in Fig. 9.5. Figure 9.5a is the amplitude and Fig. 9.5b is the phase. In the upcoming experiments, when the sample is pumped, a phase change is expected because the pump will heat up the sample causing thermal expansion. The expansion of the features, relative to the substrate, results in a phase shift to larger values.

Using the same principles to verify alignment of the pump and probe on the grating sample, diffraction patterns are collected from the gold sample as a function of pump-probe delay. First, the stage is moved to its most negative-time position and a total of 50 diffraction patterns were collected

---

[1] sample fabricated at JILA by Christina L. Porter
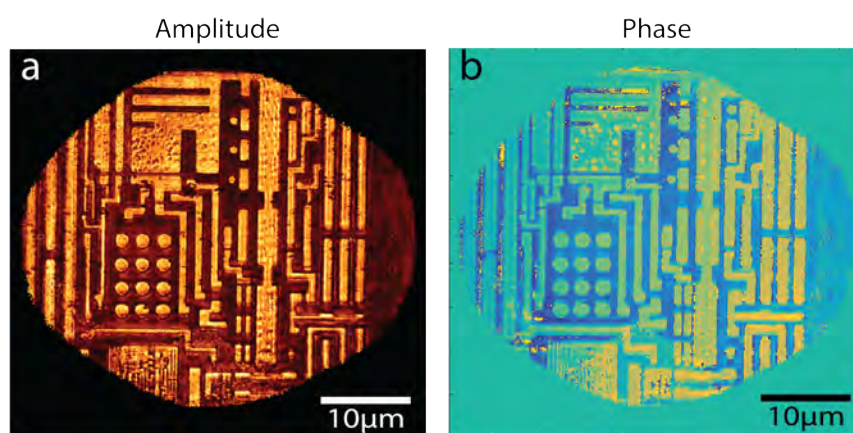
Figure 9.5: **Static Gold Circuit Reconstruction** The a) amplitude and b) phase of the gold circuit sample reconstructed from a static ptychography scan.
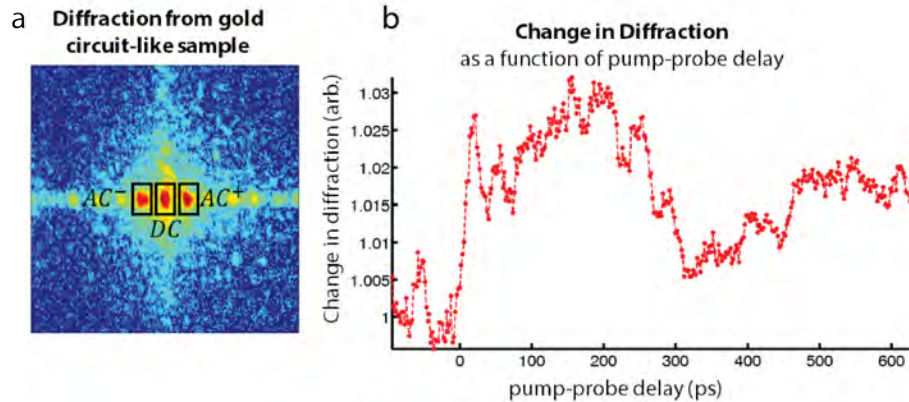
Figure 9.6: **Dynamic Signal from Circuit Diffraction** a) An example of the diffraction from the circuit sample with the beam at the center of the features. The boxes highlight the zero and first order peaks. b) Using the change in diffraction equation, Eq. 9.1, and the highlighted regions in the diffraction, a pump-probe signal is extracted.

(25 pump-on and 25 pump-off). The collection of at least 50 negative-time diffraction patterns is done to allow the sample to thermalize and reach thermal equilibrium. After thermalization, the stage is moved in 2ps steps until it reached its positive-time limit. Including pump-off and pump-on exposures, a total of 780 diffraction patterns were collected, with a representative diffraction pattern is shown in Fig. 9.6a, to generate the time trace shown in Fig. 9.6b.

Each collected diffraction pattern has an exposure time of 0.4 seconds with 2 x 2 binning on-chip and 2 accumulations. To speed up the data acquisition, only a subset of the detector was read-out in the vertical direction: 832 vertical x 2048 horizontal pixels (before binning). The input pump-power was measured at 76.2mW. The spot size of the pump, $350\mu m$, was measured at the sample plane with a CMOS detector at the $1/e^2$ intensity.

The diffraction in Fig. 9.6a does show first order peaks, but it is not as pronounced as the grating sample diffraction (Fig. 9.4a) due to the non-periodicity of the sample. As a result, the change-in-diffraction signal, Fig. 9.6b, is not as distinct as the signal from the grating, Fig. 9.4b, as quantified by the small percent change in the signal. Nevertheless, the signal is present and verifies the pump and probe are spatially and temporally overlapped on the gold circuit sample.

The static reconstruction in Fig. 9.5 and the pump-probe change in diffraction signal seen in

Fig. 9.6b confirms the proper configuration of the experiment. In a stroboscopic fashion, images are obtained using ptychography. In total, 4 ptychography scan are acquired: two scans at negative time with the pump-on and pump-off, and two scans at positive time with the pump-on and pump-off. At negative times, the probe scatters off the sample before the pump heats the sample. Therefore, there should be no change in the phases at negative times. On the other hand, at positive-time the sample is heated by the pump before the arrival of the probe, thus a phase change in the pump-on image with respect to the pump-off image is expected.

The pump-on and pump-off scan at negative time is intentional, even though theoretically the phases should be the same. The purpose of the pump-on/pump-off negative images‘ is a measurement of the repeatability and stability of the microscope. In fact, if there are statistically significant differences in the phases at negative time between pump-on/pump-off, then the microscope, in its current form, is not suitable for detection of small phase shifts from nano to micron scale structures because the signal is buried in the noise.

The parameters for each of the 4 stroboscopic ptychography scans are identical. Each scan consisted of 122 scan positions in a Fermat spiral pattern with $2\mu m$ between adjacent positions. The camera was set to readout out full-chip images at 1MHz readout rate with 2x2 binning on-chip at 0.5 second exposures and 4 accumulations. A total of 488 diffraction patterns are collected over approximately 1 hour and 40 minutes. A full ptychography scan is taken, then the alternating shutter switches states i.e., a pump-off ptychographic data set is collected followed by the pump-on ptychographic data set.

In addition to the recorded diffraction patterns, other measurements are taken and used for data analysis, namely beam and background data. Before and after the ptychography scans at a particular pump/probe delay, beam data is acquired by moving the features of the sample out of the beam path, such that the beam reflects off the silicon substrate. This beam data is used as the modulus enforced probe constraint as discussed in Sec. 8.5. The beam data, before and after scans, also measures the beam drift and changes in intensity. Background data is taken with the gas removed from the high-harmonic waveguide and is used to characterize detector‘s readout noise

and hot pixels, as well as any stray light on the detector.

The phase images from the ptychography scans are shown in Fig. 9.7 and Fig. 9.8. Figure 9.7 shows the phases at the most negative-time delay position of the stage, with the pump-on (Fig. 9.7a) and the pump-off (Fig. 9.7b). The phases of these images are displayed in a histogram plot in Fig. 9.7c with a bin width of $2\pi/200$. Similarly, 9.8a and 9.8b show the pump-on and pump-off phase images at the most positive-time delay position, with 9.8c showing the histogram phase distribution.

The phase reconstructions shown in Fig. 9.7 and Fig. 9.8 followed an identical analysis procedure. In the first step, the processing consisted of background subtraction and titled plane correction [165, 168, 169]. After titled plane correction, the diffraction patterns were cropped to 512 x 512 pixels. The retrieved probe from the static reconstruction was used as an initial probe guess. The initial object guess is always unity with no phase. The ptychographic reconstructions were done in three stages. First, the ptychography algorithm with the modulus enforced probe constraint ran for 200 iterations with probe updates allowed after iteration 11. After the first stage, the updated probe was cropped with a super Gaussian, order 60, with $\sigma = 25 \ \mu m$. The cropped probe was fed back into the algorithm for stage two. Stage two consisted of 250 iterations with probe updates after iteration 30. The modulus enforced probe constraint was only used in the first stage and not in second or third stage. During stage two, the same super Gaussian used to crop the probe was enforced during the probe updates. The enforcement of the super Gaussian eliminates noise from build-up at the edges of the updated probe. After the second stage, the retrieved probe was again cropped with a super Gaussian, order 60, but with $\sigma = 15 \mu m$. The cropped probe was fed into the algorithm for stage three. Stage three ran for 1000 iterations with no cropping of the probe. Position correction, as described by Ref. [170], was preformed between iterations 50 and 500. Updates to the probe were allowed between iterations 501 and 900. While the ptychography algorithm is a powerful phase retrieval algorithm, there are some ambiguities in reconstructions. There can be translations in the reconstructed images, which correspond to linear phase shifts. There can also be an overall offset in the phase between reconstructions.
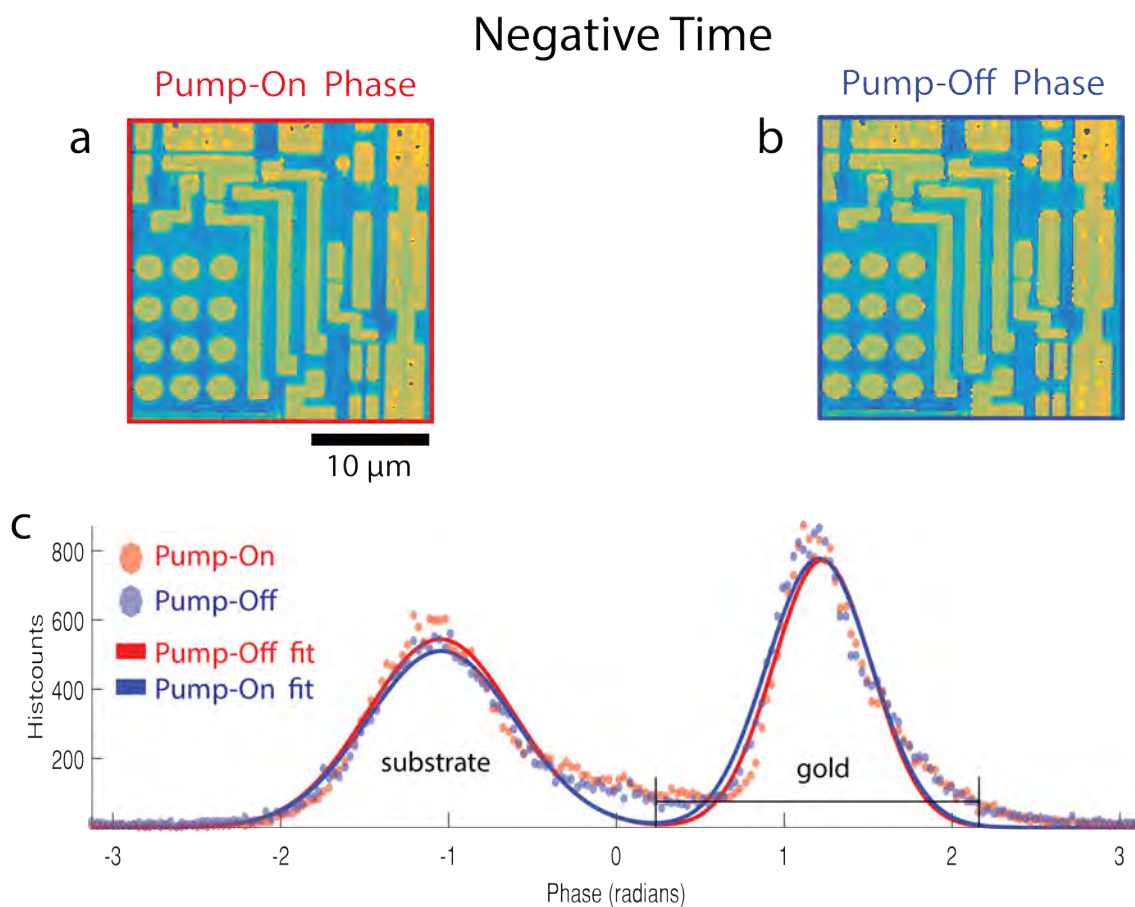
Figure 9.7: **Negative Time Phase Distribution** At negative time, the probe scatters off the sample before the pump. Therefore, there should be no difference in phase between pump on and pump off. The phase images a) with and b) without the pump. c) A histogram, $\pi/200$ bin width, of the phases (dots) with a double Gaussian best fit (solid line).The black bars at the bottom of the gold phase distribution guide the eye to the area used in t-test.
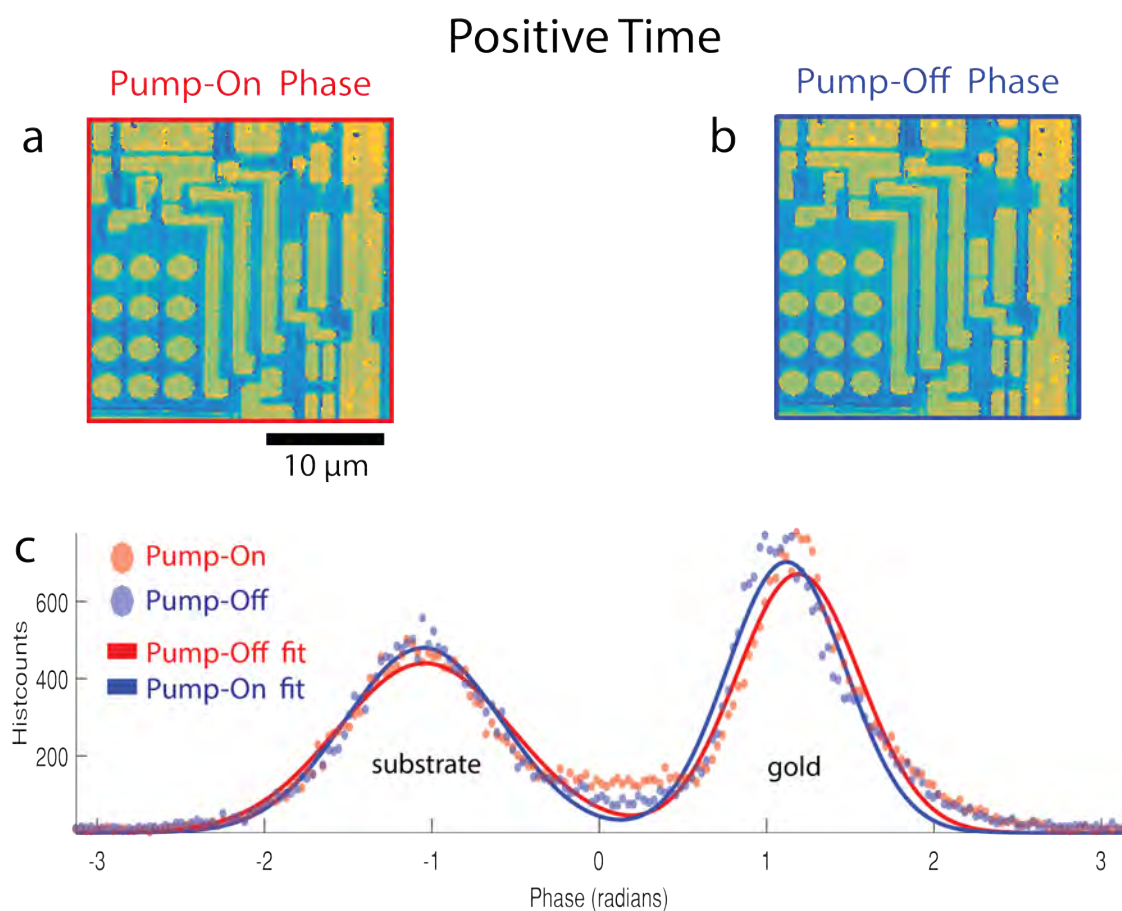
Figure 9.8: **Positive Time Phase Distribution** At positive time, the pump heats the sample before the probe scatters off the sample. Therefore, a phase shift between pump on and pump off from thermal expansion is expected. The phase images a) with and b) without the pump. c) A histogram, $\pi/200$ bin width, of the phases (dots) with a double Gaussian best fit (solid line).

Before we can compare the phases from the four reconstructions, the phase ambiguities need to be addressed. With this aim, each reconstruction is aligned to each other, by whole-pixel shifting, such that the gold features are in the same location. After aligning, the central region of the reconstruction is cropped at 200 x 200 pixels. A preliminary phase shift compensation is done by taking a histogram of the phase, with $2\pi/200$ bin widths, and calculating the center-of-mass. The center-of-mass of the phase distribution is set to zero. The shifting of the center-of-mass ensures the peaks in the histogram from the substrate and gold phases fall around zero. Without shifting the center-of-mass, the gold phase peak, for example, may be near $+\pi$ and wrap around to $-\pi$. The next step is using the phase histogram to separate the substrate from the gold features.

With the center-of-mass of the phase distribution set to zero, the histogram is fit with a double Gaussian:

$$f(\chi) = a_1 * exp(-((\chi - b_1)/c_1)^2) + a_2 * exp(-((\chi - b_2)/c_2)^2) \tag{9.2}$$

where χ the location of the histogram bin center, a the amplitude, b the offset, c the width (or σ) of the Gaussian, with the subscripts denoting the first and second Gaussian parameters. The fit is done by a non-linear least squares routine with the coefficient of determination (R^2) better than 0.96 for all the fits. The minimum phase value between the two Gaussian fits is used to separate the phase into two categories: the substrate and gold. The substrate region of the phase image is fit to a 2nd order plane given by

$$Pfit(x, y) = p00 + p10 \times x + p01 \times y + p20 \times x^2 + p11 \times x \times y + p02 \times y^2 \tag{9.3}$$

where the pXX's are the coefficients of a 2nd order plane, with x and y the coordinates of the phase image. The fitted plane is subtracted from the entire phase image (both the gold and substrate). Subtracting the fitted plane removes any phase ambiguities from the reconstructions due to phase shifts and offsets. The second order plane is used, instead of a first order, because a quadratic phase may introduced from sample bending or an inaccurate sample-to-CCD distance measurement. Regardless of the cause of phase distortion in the image, subtracting the fitted phase allows for a direct comparison of the phases from different reconstructions.

After flattening the phases by subtracting the 2nd order plane fit, the phase image is again divided into a histogram and fit to a double Gaussian. The peak of the first Gaussian, the substrate peak, is shifted so the maximum counts is arbitrarily aligned to $-pi/3$. The alignment of all the substrate peaks to $-pi/3$ allows a direct comparison of the gold feature phase distributions as shown in Fig. 9.7c and Fig. 9.8c.

9.5   Statistical significance of the phase shifts

As shown in Fig. 9.7c, the pump-on and pump-off phases at negative-time appear to be identical. On the other hand, the gold phase distribution shown in Fig. 9.8c shows a slight shift with the pump-on as compared with pump-off. In order to determine if the phase shift from the pump at positive-time is statistically significant, a Welch's t-test (or unequal variances t-test) is performed. A t-test can determine if the means of two normal distributions are statistically different and is given by

$$t_{test} = \frac{\bar{x}_2 - \bar{x}_1}{\left(\frac{\sigma_1^2}{N_1} + \frac{\sigma_2^2}{N_2}\right)^{1/2}} \qquad (9.4)$$

with the degrees of freedom Ω,

$$\Omega = \frac{\left(\frac{\sigma_1^2}{N_1} + \frac{\sigma_2^2}{N_2}\right)^2}{\frac{\sigma_1^4}{N_1^2 \nu_1} + \frac{\sigma_2^4}{N_1^2 \nu_2}} \qquad (9.5)$$

where $\bar{x}$ is the mean, σ is the standard deviation, N is the number of points, and $\nu = N - 1$. The subscripts 1 and 2 denote the pump-off and pump-on phases, respectively. The t-test assumes normal distributions and from the Gaussian fits with R^2 better than 0.96, that assumption is reasonable. Since the peak substrate phase has been assigned the value of $-pi/3$, only the gold phase distribution is analyzed with the t-test. To separate the gold phase from the substrate phase, the phase at the trough between the two fitted peaks, plus 0.24 radians, is used divide the data (see black bars in Fig. 9.7c). Phases greater than the trough are considered the gold phase, as long as the counts are greater than the counts at the trough. Removing phase values with fewer counts than the trough-point removes the tail of points extending to π. The black bars in Fig. 9.7c guide-the-eye to the points selected for the t-test. The points selected for the t-test are shown in
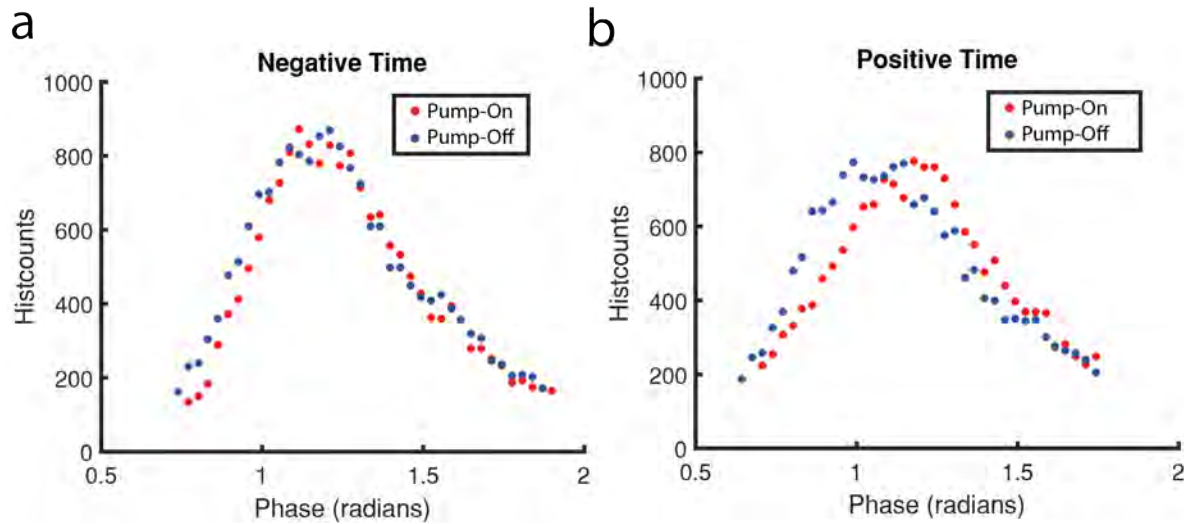
Figure 9.9: **Statistical z-test on gold phase distributions** The phase histogram distributions for (a) negative and (b) positive time. A t-test is used to determine if the means of these distributions are statistically different.

Fig. 9.9.

The mean is calculated from the histogram distribution. Each point in histogram corresponds to the number of pixels that fall within the bin width. The mean is the central bin value multiplied by the number of counts divided by the total number of counts,

$$\bar{x} = \frac{counts \times phase}{\Sigma \; counts}. \tag{9.6}$$

The standard deviation is estimated the from difference between the max and min phase values of the gold phase distribution divided by six, because in a Gaussian distribution 96% of the data falls within six standard deviations. A summary of the values used for the t-test are summarized in table 9.1. The t-test results for the negative and positive times are 0.6 and 1.2, respectively. Using a t-test significance look up table, and the given number of data points and degrees of freedom, the negative time delay phase distributions are indistinguishable. On the other hand, there is a marginal statistical difference between the pump-on and pump-off phase.

Table 9.1: **Statistical significance determined with a t-test**

		Negative Time		Positive Time	
		pump-on	pump-off	pump-on	pump-off
$\bar{x}$	mean	1.274	1.248	1.204	1.152
σ	variance	0.1728	0.1885	0.1728	0.1883
N	data points	37	37	34	36
Welch's t-test		0.5776		1.242	
degrees of freedom		72		68	
confidence level		~0%		~75%	

9.6 Calculation of the height change from thermal expansion

The change in height from thermal expansion is calculated using two methods. The first method uses the difference in mean values between the gold phase distributions from the histogram (Fig. 9.9). The difference in the mean values, shown in Table 9.1, is 0.05 radians, and using the following equations:

$$\Delta d = \frac{\Delta \phi \lambda}{2\pi} \tag{9.7}$$

$$\Delta h = \frac{\Delta d}{2 \cos \theta} \tag{9.8}$$

the change in height Δh is calculated, where Δd is the optical path length difference, $\Delta \phi$ is the phase change in radians, λ is the wavelength, and θ is the angle of incidence on the sample (from normal). This calculation yields a height change of 2.4 Å.

The other method uses the phase difference between the substrate and gold features to calculate to the height of the gold. In order to compare the phase from the different materials, the phase change upon reflection needs to be calculated. The procedure used here is adapted from Ref. [204], which describes how to calculate the complex reflection coefficient from a stack of materials. The complex indices of refraction where taken from Ref. [180]. The thickness of the silicon oxide layer, 3 nm, was measured on a similar substrate in previous work using ellipsometry [169]. Taking into account the phase change upon reflection, the average phase change between the substrate and the gold feature is 7.23 radians with the pump off and 7.29 radians with the pump on. Using

equations 9.7 and 9.7, the heights of the gold features are 35.3 nm and 35.6 nm, respectively, corresponding of a thermal expansion induced height change of 3 Å.

9.7   Summary and Future work

The design and implementation of an extreme ultraviolet microscope capable of stroboscopic ultrafast temporal resolution is demonstrated here with a preliminary data analysis. Some of the near-infrared driving laser is split-off before the high-harmonic generation and used to heat the sample. Spatial and temporal alignment of the system was verified with a grating sample, using similar techniques described previously [191, 202, 203]. The thermal expansion of the grating, due to heating from the pump, causes a time dependent change in diffraction. A non-periodic sample was then used and ptychographic scans were collected, with and without the pump, and negative and positive time delays. The phase reconstructions demonstrate a 3 Åheight change at from thermal expansion.

While there is a difference, between the pump-on and pump-off phase at positive times, the statistical difference is marginal. Using the same data set, the statistics may improve with further data processing. For example, letting the ptychography algorithm iterate for longer, i.e. 10,000 iterations instead of the 1450 used here, will allow the phase distribution to converge to a more homogeneous value thereby strengthening the significance of the t-test. For reference, over 10,000 iterations were used to obtain the high-fidelity images with sub-wavelength resolution discussed in the previous chapter (Ch. 8); therefore using the same number of iteration here is reasonable.

There are also many other datasets not presented here that show promising dynamics, such as datasets in which a 16 μm diameter circular nickel structure was pumped. The reconstruction of this data set suggests a radial expansion of 100nm, with a 1nm axial expansion, when pumped. The challenge with the circle data is the time trace analysis because the diffraction from the circle does not of clear diffraction orders. New methods for detecting changes in diffraction are currently being investigated, including radially averaging techniques.

To improve future data collections the camera readout time needs to be faster. As of right

now, nearly all of the data collection time is readout. Typical exposures for the dynamic data sets were less than a second, but it takes about 15 seconds to readout the CCD. With the ability to readout faster, many more ptychography scans could be taken immediately following time zero and after reconstruction and registering the images, a movie could be rendered.

The methodology described here can be used to study scientifically relevant samples in the near future. For example, the techniques described here can be combined with newly demonstrated circularly polarized high-harmonic generation [205, 206] for magnetic domain imaging [207, 208]. The combination of the pump and EUV probe tuned to a magnetic edge, can be used to study ultrafast demagnetization [194], which is important for next-generation data storage devices.

Chapter 10

Conclusion

10.1   Summary

This thesis discussed methods for high-resolution static and stroboscopic microscopy using tabletop coherent extreme ultraviolet (EUV) light from tabletop high-harmonic generation (HHG) sources (Ch. 4). An ultrafast Ti:Sapphire laser was up-converted using HHG to either 30 nm or 13.5 nm harmonics, depending on the demonstration. The coherent short wavelength sources were combined with a lensless, computational, phase and amplitude-contrast technique called ptychographic Coherent Diffractive Imaging (CDI) (Ch. 6).

In this work, a combination of experimental methods for high-numerical aperture data collection and novel computational algorithms enabled the highest resolution-to-wavelength imaging using CDI and EUV in both reflection and transmission geometries. For ptychographic CDI imaging in a reflection geometry, the titled plane correction algorithm [165] was developed, which enabled high-resolution imaging of surfaces in a reflection geometry (Ch. 7). An EUV microscope with 40 nm transverse resolution and 6 Åaxial resolution using 30 nm radiation was developed [168].

A powerful technique termed modulus enforced probe, was developed in this work which enables both imaging of periodic objects and convergence of the ptychographic CDI algorithm in fewer iterations (Ch. 8). The novel constraint consists of on additional measurement of the unscattered illumination at the detector plane, which is used to tightly constrain the algorithms guess of the illumination. The MEP constraint was used to achieve a record subwavelength resolution image, 12.6 nm, of an extend periodic sample in the EUV spectral region using the technologically

relevant wavelength of 13.5 nm [173].

Furthermore, the ultrafast pulse durations in the femtosecond (fs) range of the high-harmonic source were harnessed to demonstrate proof-of-principle pump-probe imaging of nanostructures (Ch. 9). Some of the IR light used to generate the harmonics, was split off and used to pump a sample with micron to nanoscale structures. Two images of the structure were taken strobo-scopically, and captured the thermal excitation of the nano-features with an axial resolution of 3 angstroms (Å).

10.2 Future Work

In Ch. 7, high numerical aperture CDI imaging was demonstrated in a reflection geometry for the first time. The structures used for the EUV demonstration (Sec. 7.2) had low, on the order of one, aspect ratios: the ratio of feature depth to wavelength-of-illumination. Some work on high aspect ratio structures has been done in a transmission geometry [209], but thus far there have been no reflection demonstrations in the EUV or x-ray spectral regions. The ability to image high-aspect ratio structures further opens up the applicability of EUV CDI.

Regarding the Modulus Enforced Probe (MEP) constraint discussed in Ch. 8, further sim-ulations and demonstrations are needed. With simulated data, it was seen that the ptychography algorithm converges in fewer iterations with MEP, but the iteration time per iteration is slower. With a modified application of MEP, such that it is only applied every five or ten iterations, it is suspected that the convergence properties will be nearly the same, but the per iteration time will be much faster. Simulations and experimental demonstration of CDI on a near-perfect periodic sample will be exciting future work. Of particular importance, is the imaging of self-assembled periodic structures from block copolymers [210]. These structures are promising as the building blocks of nano-engineered systems, but are sometimes difficult to image using electron microscopies because they are non-conducting, low-z, materials.

Many opportunities remain to be explored with the newly demonstrated EUV dynamic imag-ing capabilities. In the immediate future, there needs to be more data processing of acquired data,

especially of data acquired on a 16 μm nickel disc sample and on a 750 nm nickel grating. In preliminary analysis, the nickel disc sample shows about a 100nm radial and 1nm axial thermal expansion due to pumping. The grating sample is also promising, but reconstruction quality is poor at the moment. Application of the MEP constraint and more iterations may yield better images.

The development of a new algorithm is needed to verify a time-dependent change in diffraction signal due to pumping. As discussed in section 9.3, the diffraction peaks of a grating were used to verify the spatial and temporal alignment of the pump and probe. This is a powerful tool and has been used to study nanoscale heat flow [191, 202, 203], and a similar techniques have analyzed the Airy diffraction patterns from circular samples [196, 197]. In its current form, this technique only work for periodic objects, or simply circular shapes, with well-known diffraction. For a general structure, it does not perform well. An algorithm capable of quantify changes in diffraction patterns from general structures, but is insensitive to fluctuation in high-harmonic radiation, is needed to open up the EUV stroboscopic microscope to a broader sample set.

In future stroboscopic EUV microscope systems, a camera with faster readout is critical. The largest bottle neck in data collection is the readout of the CCD. The exposure time is less than a second, even with multiple accumulations, but the readout time takes 15 seconds or longer. The recently released, commercially available, back-illuminated CMOS cameras will enable faster data collection, so more snapshots of the sample can be taken enabling movies showing the angstrom-scale axial dynamics of nanoscale features.

10.3 Future Outlook

One of the advantages of EUV and x-ray wavelengths is the long penetration depths compared with electron microcopy methods, allowing for the imaging of buried surfaces non-destructively. A recent demonstration used EUV at 30 nm to image below an optical opaque film of aluminum (see Fig. 10.1). [179]. Currently under development are experimental methods and algorithms to image the interior of objects, without the need to physically slice the sample. Instead, these techniques computationally decompose the sample into thin slices, tasking the ptychography algorithm to solve

for each slice, such that the resulting exit-surface-wave, when propagated to the detector plane, is consistent with the measurement [187–190]. These three-dimensional algorithms are likely to be adapted to image high-aspect ratio structures in a reflection geometry.
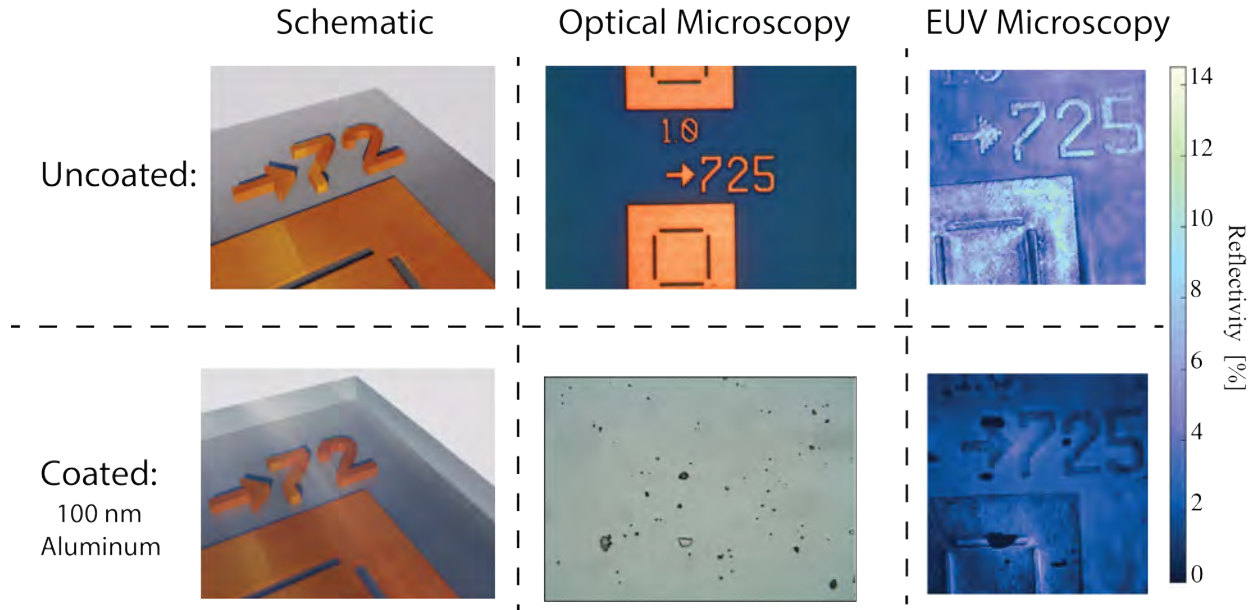
Figure 10.1: **EUV imaging through metal** A planarized damascene sample, copper and silicon, is coated with 100nm Al. The aluminum coating prevents an optical microscope from imaging the buried surface. With EUV, the damascene sample is imaged with and with the metal coating. Figure adapted from Ref. [179].

The analysis of the phase distribution in the stroboscopic images, section 9.4 and 9.5, suggest 3 angstrom resolution in the axial direction. In future work, an analytical expression for the phase resolution is of interest. The ability to image atomic layers should be possible and can be tested on cleaved SiC wafers used for atomic force microscopy calibration. These sample are nearly-periodic, but the application of the MEP constraint should enable reconstructions.

Typically, a single harmonic is used for imaging, but recent work has shown simultaneous illumination of a sample with multiple harmonics (see Fig. 10.2a) [211]. The ptychography algorithm then reconstructs an image for each harmonic. In the future, this methodology can be applied with harmonics spanning atomic edges providing elemental contrast without the need to scan wavelengths with hardware.

In related work, it has been shown that different areas of the sample can be imagined simultaneously, with different probes, allowing larger fields of view with a single scan [212]. In the same work, it was also shown that orthogonal polarization states can be used in image a sample simultaneously (see Fig. 10.2b). Employing polarization sensitivity in the EUV, in combination with CDI, will allow for a complete characterization of how light interacts with the sample: amplitude, phase, and polarization contrast.

An exciting possibility is tabletop magnetic imaging using the newly demonstrated circularly polarized high-harmonics (see Fig. 10.2c) [205, 206, 213]. The circularly harmonics, if properly tuned to the magnetic edge, can be used to image magnetic domains, as done at large scale facilities [98, 208, 214].

All of the techniques developed in this thesis are scalable to shorter wavelengths, wavelengths shorter than a nanometer using mid-IR driving lasers (see Fig. 10.2d) [63, 84, 85]. Furthermore, the stroboscopic methods discussed can employ short pulses, pulses as short as attoseconds [30, 89]. The combination of attosecond pulses with soft-x-ray HHG, will probe the fastest dynamic processes at the nanoscale.

a) EUV Hyperspectral Imagng
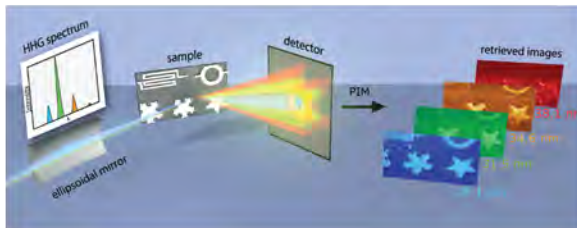
b) Polarization Multiplexed Ptychography
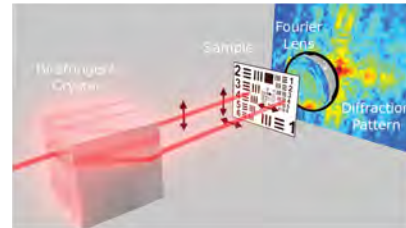
c) Non-collinear circularly polarized HHG
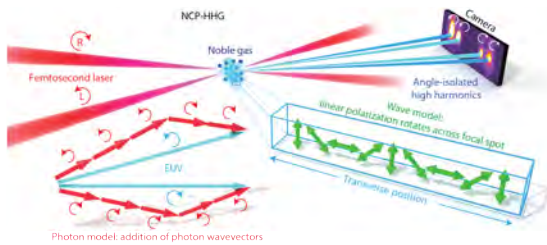
d) Sub-nanometer soft-x-ray HHG
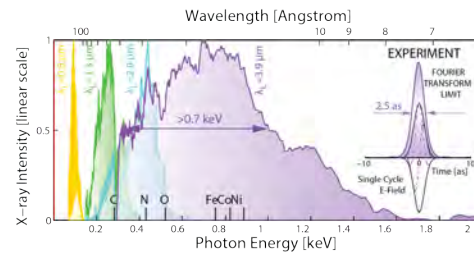
Figure 10.2: **Possibilities for future work** a) EUV hyperspectral imaging with simultaneous illumination of harmonics. In the future, harmonics spanning atomic transitions can be used for element specific imaging. Panel adapted from Ref. [215]. b) Polarization multiplexed ptychography can be applied in the EUV for a complete characterization of lights interaction with the sample. Panel adapted from Ref. [212] c) The generation of circularly polarized HHG can be used to image magnetic samples. Panel adapted from Ref. [206] d) The generation of sub-nanometer soft-x-ray from mid-IR driving lasers will lead to higher spatial and temporal EUV microscopy. Panel adapted from Ref [63]

Bibliography

[1] R. Hooke, <u>Micrographia, or Some physiological descriptions of minute bodies</u> (J. Martyn and J. Allestry, London, 1665), 1st ed.

[2] D. Evanko, A. Heinrichs, and C. K. Rosenthal, "Milestones in Optical Microscopy," Nat. Cell Biol. **11**, S56 (2009).

[3] "Numerical aperture of a thin lens by Moxfyre at English Wikipedia [Public domain], via Wikimedia Commons," .

[4] J. Squier and M. Müller, "High resolution nonlinear microscopy: A review of sources and methods for achieving optimal imaging," Rev. Sci. Instrum. **72**, 2855–2867 (2001).

[5] W. R. Zipfel, R. M. Williams, and W. W. Webb, "Nonlinear magic: multiphoton microscopy in the biosciences." Nat. Biotechnol. **21**, 1369–77 (2003).

[6] J.-X. Cheng and X. S. Xie, "Coherent Anti-Stokes Raman Scattering Microscopy: Instrumentation, Theory, and Applications," J. Phys. Chem. B **108**, 827 (2004).

[7] U. Dürig, D. W. Pohl, and F. Rohner, "Near-field optical-scanning microscopy," J. Appl. Phys. **59**, 3318–3327 (1986).

[8] E. Betzig, A. Lewis, A. Harootunian, M. Isaacson, and E. Kratschmer, "Near Field Scanning Optical Microscopy (NSOM)," Biophys. J. **49**, 269–279 (1986).

[9] E. H. Synge, "XXXVIII. A suggested method for extending microscopic resolution into the ultra-microscopic region," London, Edinburgh, Dublin Philos. Mag. J. Sci. **6**, 356–362 (1928).

[10] E. A. Ash and G. Nicholls, "Super-resolution Aperture Scanning Microscope," Nature **237**, 510–512 (1972).

[11] A. Bek, R. Vogelgesang, and K. Kern, "Apertureless scanning near field optical microscope with sub-10 nm resolution," Rev. Sci. Instrum. **77**, 43703 (2006).

[12] Z. Li, S. Yue, J. Chen, and Q. Gong, "Ultrafast spatiotemporal relaxation dynamics of excited electrons in a metal nanostructure detected by femtosecond-SNOM." Opt. Express **18**, 14232–14237 (2010).

[13] T. A. Klar, S. Jakobs, M. Dyba, A. Egner, and S. W. Hell, "Fluorescence microscopy with diffraction resolution barrier broken by stimulated emission." Proc. Natl. Acad. Sci. U. S. A. **97**, 8206–8210 (2000).

[14] T. A. Klar, E. Engel, and S. W. Hell, "Breaking Abbe's diffraction resolution limit in fluorescence microscopy with stimulated emission depletion beams of various shapes." Phys. Rev. **64**, 066613 (2001).

[15] R. M. Dickson, a. B. Cubitt, R. Y. Tsien, and W. E. Moerner, "On/off blinking and switching behaviour of single molecules of green fluorescent protein." Nature **388**, 355–358 (1997).

[16] R. Henriques, C. Griffiths, E. H. Rego, and M. M. Mhlanga, "PALM and STORM: Unlocking live-cell super-resolution," Biopolymers **95**, 322–331 (2011).

[17] E. Betzig, G. H. Patterson, R. Sougrat, O. W. Lindwasser, S. Olenych, J. S. Bonifacino, M. W. Davidson, J. Lippincott-Schwartz, and H. F. Hess, "Imaging intracellular fluorescent proteins at nanometer resolution." Science **313**, 1642–5 (2006).

[18] L. de Broglie, "Recherches sur la théorie des quanta (Researches on the quantum theory)," Ann. Phys. **3** (1925).

[19] E. Ruska and M. Knoll, "Die magnetische Sammelspule für schnelle Elektronenstrahlen. (The magnetic concentrating coil for fast electron beams.)," Z. Tech. Phys. **12**, 389–400 (1931).

[20] M. M. Freundlich, "Origin of the Electron Microscope," Science **142**, 185–188 (1963).

[21] A. Bogner, P. H. Jouneau, G. Thollet, D. Basset, and C. Gauthier, "A history of scanning electron microscopy developments: Towards "wet-STEM" imaging," Micron **38**, 390–401 (2007).

[22] K. W. Urban, "Is science prepared for atomic-resolution electron microscopy?" Nat. Mater. **8**, 260–2 (2009).

[23] B. Barwick, H. S. Park, O.-H. Kwon, J. S. Baskin, and A. H. Zewail, "4D Imaging of Transient Structures and Morphologies in Ultrafast Electron Microscopy," Science **322**, 1227 – 1231 (2008).

[24] A. H. Zewail, "Four-Dimensional Electron Microscopy," Science **328**, 187–193 (2010).

[25] T. Van Oudheusden, P. L. E. M. Pasmans, S. B. Van Der Geer, M. J. De Loos, M. J. Van Der Wiel, and O. J. Luiten, "Compression of subrelativistic space-charge-dominated electron bunches for single-shot femtosecond electron diffraction," Phys. Rev. Lett. **105**, 1–4 (2010).

[26] G. Binnig and H. Rohrer, "Scanning Tunneling Microscopy," IBM J. Res. Dev. **44**, 279 (1993).

[27] G. Binnig, C. F. Quate, and C. Gerber, "Atomic Force Microscope," Phys. Rev. Lett. **56**, 930–933 (1986).

[28] S. Weiss, D. F. Ogletree, D. Botkin, M. Salmeron, and D. S. Chemla, "Ultrafast scanning probe microscopy," Appl. Phys. Lett. **63**, 2567–2569 (1993).

[29] N. Khusnatdinov, T. Nagle, and G. Nunes, "Ultrafast scanning tunneling microscopy with 1 nm resolution," Appl. Phys. Lett. **77**, 4434–4436 (2000).

[30] T. Popmintchev, M.-C. Chen, P. Arpin, M. M. Murnane, and H. C. Kapteyn, "The attosecond nonlinear optics of bright coherent X-ray generation," Nat. Photonics **4**, 822–832 (2010).

[31] "A diagram of the electromagnetic spectrum, showing various properties across the range of frequencies and wavelengths by Inductiveload, NASA [GFDL (\url{http://www.gnu.org/copyleft/fdl.html) or CC-BY-SA-3.0 (http://creativecommons.org/licenses/by-sa/3.0/}," .

[32] D. H. Bilderback, P. Elleaume, and E. Weckert, "Review of third and next generation synchrotron light sources," J. Phys. B At. Mol. Opt. Phys. **38**, S773–S797 (2005).

[33] T. K. Sham and M. L. Rivers, "A brief overview of synchrotron radiation," Rev. Mineral. Geochemistry **49**, 117–147 (2002).

[34] J. D. Jackson, Classical Electrodynamics (Wiley & Sons, Hoboken, 1999), 3rd ed.

[35] D. J. Griffiths, Introduction to Electrodynamics (Prentice Hall, Upper Saddle River, 1999), 3rd ed.

[36] K. Willie, The Physics of Particle Accelerators, an Introduction (Oxford University Press, Oxford, 2000).

[37] D. Attwood, Soft X-Rays And Extreme Ultravioet Radiation Principles and Applications (Cambridge, New York, 1999).

[38] A. Zholents and M. Zolotorev, "Femtosecond X-Ray Pulses of Synchrotron Radiation," Phys. Rev. Lett. **76**, 912–915 (1996).

[39] R. W. Schoenlein, S. Chattopadhyay, H. H. W. Chong, T. E. Glover, P. A. Heimann, C. V. Shank, A. A. Zholents, and M. S. Zolotorev, "Generation of Femtosecond Pulses of Synchrotron Radiation," Science **287**, 2237–2240 (2000).

[40] T. C. Marshall, Free-Electron Lasers (Macmillan Publishing Co., New York, 1985).

[41] C. Brau, "Free-electron lasers," Science **239**, 1115–21 (1988).

[42] C. A. Brau, Free-Electron Lasers (Academic Press, Inc., San Diego, 1990).

[43] H. P. Freund and T. M. Antonsen-Jr., Principles of Free-Electron Lasers (Springer, New York, 1992).

[44] E. L. Saldin, E. Schneidmiller, and M. V. Yurkov, The Physics of Free Electron Lasers (Springer, Heidelberg, 2000).

[45] P. Schmuser, M. Dohlus, and J. Rossbach, Ultraviolet and Soft-Ray Free-Electron Lasers (Springer, Heidelberg, 2008).

[46] B. W. J. McNeil and N. R. Thompson, "X-ray free-electron lasers," Nat. Photonics **4**, 814–821 (2010).

[47] H. Motz, "Applications of the radiation from fast electron beams," J. Appl. Phys. **22**, 527–535 (1951).

[48] H. Motz, W. Thon, and R. N. Whitehurst, "Experiments on radiation by fast electron beams," J. Appl. Phys. **24**, 826–833 (1953).

[49] J. M. J. Madey, "Stimulated emission of bremsstrahlung in a periodic magnetic field," J. Appl. Phys. **42**, 1906–1913 (1971).

[50] L. R. Elias, W. M. Fairbank, J. M. J. Madey, H. A. Schwettman, and T. I. Smith, "Observation of stimulated emission of radiation by relativistic electrons in a spatially periodic transverse magnetic field," Phys. Rev. Lett. **36**, 717–720 (1976).

[51] D. A. G. Deacon, L. R. Elias, J. M. J. Madey, G. J. Ramian, H. A. Schwettman, and T. I. Smith, "First Operation of a Free-Electron Laser," Phys. Rev. Lett. **38**, 892–894 (1977).

[52] P. Emma, R. Akre, J. Arthur, R. Bionta, C. Bostedt, J. Bozek, a. Brachmann, P. Bucksbaum, R. Coffee, F.-J. Decker, Y. Ding, D. Dowell, S. Edstrom, a. Fisher, J. Frisch, S. Gilevich, J. Hastings, G. Hays, P. Hering, Z. Huang, R. Iverson, H. Loos, M. Messerschmidt, a. Miahnahri, S. Moeller, H.-D. Nuhn, G. Pile, D. Ratner, J. Rzepiela, D. Schultz, T. Smith, P. Stefan, H. Tompkins, J. Turner, J. Welch, W. White, J. Wu, G. Yocky, and J. Galayda, "First lasing and operation of an ångstrom-wavelength free-electron laser," Nat. Photonics **4**, 641–647 (2010).

[53] S. Roling and M. Wöstmann, "The free electron laser FLASH," (2015).

[54] D. L. Matthews, P. L. Hagelstein, M. D. Rosen, M. J. Eckart, N. M. Ceglio, A. U. Hazi, H. Medecki, B. J. MacGowan, J. E. Trebes, B. L. Whitten, E. M. Campbell, C. W. Hatcher, A. M. Hawryluk, R. L. Kauffman, L. D. Pleasance, G. Rambach, J. H. Scofield, G. Stone, and T. A. Weaver, "Demonstration of a soft x-ray amplifier," Phys. Rev. Lett. **54**, 110–113 (1985).

[55] J. J. Rocca, "Table-top soft x-ray lasers," Rev. Sci. Instrum. **70**, 3799 (1999).

[56] J. J. Rocca, V. Shlyaptsev, F. G. Tomasel, O. D. Cortzar, D. Hartshorn, and J. L. A. Chilla, "Demonstration of a discharge pumped table-top soft-x-ray laser," Phys. Rev. Lett. **73**, 2192–2195 (1994).

[57] S. Heinbuch, M. Grisham, D. Martz, and J. J. Rocca, "Demonstration of a desk-top size high repetition rate soft x-ray laser." Opt. Express **13**, 4050–4055 (2005).

[58] D. Alessi, Y. Wang, B. M. Luther, L. Yin, D. H. Martz, M. R. Woolston, Y. Liu, M. Berrill, and J. J. Rocca, "Efficient Excitation of Gain-Saturated Sub-9-nm-Wavelength Tabletop Soft-X-Ray Lasers and Lasing Down to 7.36 nm," Phys. Rev. X **1**, 1–6 (2011).

[59] J. Bokor, P. H. Bucksbaum, and R. R. Freeman, "Generation of 355-nm coherent radiation," Opt. Lett. **8**, 217 (1983).

[60] A. McPherson, G. Gibson, H. Jara, U. Johann, T. S. Luk, I. a. McIntyre, K. Boyer, and C. K. Rhodes, "Studies of multiphoton production of vacuum-ultraviolet radiation in the rare gases," J. Opt. Soc. Am. B **4**, 595 (1987).

[61] P. B. Corkum, "Plasma perspective on strong field multiphoton ionization," Phys. Rev. Lett. **71**, 1994–1997 (1993).

[62] M. Lewenstein, P. Balcou, M. Y. Ivanov, A. L'Huillier, and P. B. Corkum, "Theory of high-harmonic generation by low-frequency laser fields," Phys. Rev. A **49**, 2117–2132 (1994).

[63] T. Popmintchev, M.-C. Chen, D. Popmintchev, P. Arpin, S. Brown, S. Alisauskas, G. Andriukaitis, T. Balciunas, O. D. Mücke, A. Pugzlys, A. Baltuska, B. Shim, S. E. Schrauth, A. Gaeta, C. Hernández-García, L. Plaja, A. Becker, A. Jaron-Becker, M. M. Murnane, and H. C. Kapteyn, "Bright coherent ultrahigh harmonics in the keV x-ray regime from mid-infrared femtosecond lasers," Science **336**, 1287–91 (2012).

[64] J. Seres, E. Seres, A. J. Verhoef, G. Tempea, C. Streli, P. Wobrauschek, V. Yakovlev, A. Scrinzi, C. Spielmann, and F. Krausz, "Laser technology: Source of coherent kiloelectronvolt X-rays," Nature **443**, 596 (2005).

[65] D. E. Spence, P. N. Kean, and W. Sibbett, "60-fsec pulse generation from a self-mode-locked Ti:sapphire laser." Opt. Lett. **16**, 42–44 (1991).

[66] A. L. Lytle, "Phase Matching and Coherence of High-Order Harmonic Generation in Hollow Waveguides," Ph.D. thesis, University of Colorado (2001).

[67] J. Zhou, I. P. Christov, G. Taft, C.-P. Huang, M. M. Murnane, and H. C. Kapteyn, "Pulse evolution in a broad-bandwidth Ti:sapphire laser," Opt. Lett. **19**, 1149–1151 (1994).

[68] M. Pessot, P. Maine, and G. Mourou, "1000 Times Expansion/Compression of Optical Pulses for Chirped Pulse Amplification," Opt. Commun. **62**, 419–421 (1987).

[69] P. Maine, D. Strickland, P. Bado, M. Pessot, and G. Mourou, "Generation of Ultrahigh Peak Power Pulses By Chirped Pulse Amplification." IEEE J. Quantum Electron. **24**, 398–403 (1988).

[70] D. Müller, S. Backus, K. Read, M. Murnane, and H. Kapteyn, "Very high-peakpower lasers: cryogenic cooling multiplies ti:sapphire output," Laser Focus World **41**, 1–6 (2005).

[71] D. Strickland and G. Mourou, "Compression of amplified chirped optical pulses," Opt. Commun. **56**, 219–221 (1985).

[72] S. Backus, C. G. Durfee, M. M. Murnane, and H. C. Kapteyn, "High power ultrafast lasers," Rev. Sci. Instrum. **69**, 1207–1223 (1998).

[73] S. Backus, R. Bartels, S. Thompson, R. Dollinger, H. C. Kapteyn, and M. M. Murnane, "High-efficiency, single-stage 7-kHz high-average-power ultrafast laser system," Opt. Lett. **26**, 465–467 (2001).

[74] M. D. Seaberg, "Nanoscale EUV Microscopy on a Tabletop: A General Transmission and Reflection Mode Microscope Based on Coherent Di ractive Imaging with High Harmonic Illumination," Ph.D. thesis, University of Colorado (2014).

[75] H. C. Kapteyn, M. M. Murnane, and I. P. Christov, "Extreme nonlinear optics: Coherent X rays from lasers," Phys. Today **58**, 39–44 (2005).

[76] G. Ndabashimiye, S. Ghimire, M. Wu, D. A. Browne, K. J. Schafer, M. B. Gaarde, and D. A. Reis, "Solid-state harmonics beyond the atomic limit," Nature **534**, 520–523 (2016).

[77] U. Teubner and P. Gibbon, "High-order harmonics from laser-irradiated plasma surfaces," Rev. Mod. Phys. **81**, 445–479 (2009).

[78] J. Zhou, J. Peatross, M. Murnane, H. Kapteyn, and I. Christov, "Enhanced High-Harmonic Generation Using 25 fs Laser Pulses," Phys. Rev. Lett. **76**, 752–755 (1996).

[79] Z. Chang, A. Rundquist, H. Wang, M. Murnane, and H. Kapteyn, "Generation of Coherent Soft X Rays at 2.7 nm Using High Harmonics," Phys. Rev. Lett. **79**, 2967–2970 (1997).

[80] C. Durfee, A. Rundquist, S. Backus, C. Herne, M. Murnane, and H. Kapteyn, "Phase Matching of High-Order Harmonics in Hollow Waveguides," Phys. Rev. Lett. **83**, 2187–2190 (1999).

[81] A. Rundquist, C. G. Durfee III, Z. Chang, C. Herne, S. Backus, M. M. Murnane, and H. C. Kapteyn, "Phase-Matched Generation of Coherent Soft X-rays," Science **280**, 1412–1415 (1998).

[82] R. A. Bartels, A. Paul, H. Green, H. C. Kapteyn, M. M. Murnane, S. Backus, I. P. Christov, Y. Liu, D. Attwood, and C. Jacobsen, "Generation of Spatially Coherent Light at Extreme Ultraviolet Wavelengths," Science **297**, 376–378 (2002).

[83] A. Paul, E. a. Gibson, X. Zhang, A. Lytle, T. Popmintchev, X. Zhou, M. M. Murnane, I. P. Christov, and H. C. Kapteyn, "Phase-matching techniques for coherent soft X-ray generation," IEEE J. Quantum Electron. **42**, 14–26 (2006).

[84] M. C. Chen, P. Arpin, T. Popmintchev, M. Gerrity, B. Zhang, M. Seaberg, D. Popmintchev, M. M. Murnane, and H. C. Kapteyn, "Bright, coherent, ultrafast soft x-ray harmonics spanning the water window from a tabletop light source," Phys. Rev. Lett. **105**, 1–4 (2010).

[85] C. Ding, W. Xiong, T. Fan, D. D. Hickstein, T. Popmintchev, X. Zhang, M. Walls, M. M. Murnane, and H. C. Kapteyn, "High flux coherent super-continuum soft X-ray source driven by a single-stage, 10mJ, Ti:sapphire amplifier-pumped OPA." Opt. Express **22**, 6194–202 (2014).

[86] A. L'Huillier, K. J. Schafer, and K. C. Kulander, "Theoretical aspects of intense field harmonic generation," J. Phys. B At. Mol. Opt. Phys. **24**, 3315–3341 (1999).

[87] G. Sansone, E. Benedetti, F. Calegari, C. Vozzi, L. Avaldi, R. Flammini, L. Poletto, P. Villoresi, C. Altucci, R. Velotta, S. Stagira, S. De Silvestri, and M. Nisoli, "Isolated Single-Cycle Attosecond Pulses," Science **314**, 443–446 (2006).

[88] I. Christov, M. Murnane, and H. Kapteyn, "High-Harmonic Generation of Attosecond Pulses in the Single-Cycle Regime," Phys. Rev. Lett. **78**, 1251–1254 (1997).

[89] M.-C. Chen, C. Mancuso, C. Hernández-García, F. Dollar, B. Galloway, D. Popmintchev, P.-C. Huang, B. Walker, L. Plaja, A. A. Jaroń-Becker, A. Becker, M. M. Murnane, H. C. Kapteyn, and T. Popmintchev, "Generation of bright isolated attosecond soft X-ray pulses driven by multicycle midinfrared lasers." Proc. Natl. Acad. Sci. U. S. A. **111**, E2361–7 (2014).

[90] S. Wilkins, T. Gureyev, D. Gao, A. Pogany, and A. Stevenson, "Phase-contrast imaging using polychromatic hard X-rays," Nature **384**, 335–384 (1996).

[91] A. Snigirev, V. Kohn, I. Snigireva, and B. Lengeler, "A compound refractive lens for focusing high-energy X-rays," Nature **384**, 49–51 (1996).

[92] A. Snigirev, V. Kohn, I. Snigireva, A. Souvorov, and B. Lengeler, "Focusing high-energy x rays by compound refractive lenses." Appl. Opt. **37**, 653–662 (1998).

[93] A. Schropp, R. Hoppe, V. Meier, J. Patommel, F. Seiboth, H. J. Lee, B. Nagler, E. C. Galtier, B. Arnold, U. Zastrau, J. B. Hastings, D. Nilsson, F. Uhlén, U. Vogt, H. M. Hertz, and C. G. Schroer, "Full spatial characterization of a nanofocused x-ray free-electron laser beam by ptychographic imaging." Sci. Rep. **3**, 1633 (2013).

[94] F. Seiboth, A. Schropp, R. Hoppe, V. Meier, J. Patommel, H. J. Lee, B. Nagler, E. C. Galtier, B. Arnold, U. Zastrau, J. B. Hastings, D. Nilsson, F. Uhlén, U. Vogt, H. M. Hertz, and C. G. Schroer, "Focusing XFEL SASE pulses by rotationally parabolic refractive x-ray lenses," J. Phys. Conf. Ser. **499**, 1–10 (2014).

[95] A. A. Snigirev, "Refractive lenses allow compact, precision focusing of x-rays," SPIE Newsroom (2011).

[96] P. Horowitz and J. A. Howell, "A scanning x-ray microscope using synchrotron radiation." Science **178**, 608–611 (1972).

[97] I. McNulty, J. Kirz, C. Jacobsen, E. H. Anderson, M. R. Howells, and D. P. Kern, "High-Resolution Imaging by Fourier Transform X-ray Holography." Science **256**, 1009–1012 (1992).

[98] S. Eisebitt, J. Luning, W. Schlotter, M. Lorgen, O. Hellwig, W. Eberhardt, and J. Stohr, "Lensless imaging of magnetic nanostructures by X-ray spectro-holography," Nature **432**, 885–888 (2004).

[99] P. Kirkpatrick and A. V. Baez, "Formation of optical images by X-rays." J. Opt. Soc. Am. **38**, 766–774 (1948).

[100] I. A. Artioukov, X.-r. O. Group, K. M. Krymski, and M. Region, "Schwarzschild objective for soft x-rays," Opt. Eng. **39**, 1–8 (2000).

[101] I. A. Artyukov, "Schwarzschild objective and similar two-mirror systems," Short-Wavelength Imaging Spectrosc. Sources, Proc. SPIE **8678**, 86780A (2012).

[102] A. Budano, F. Flora, and L. Mezi, "Analytical design method for a modified Schwarzschild optics." Appl. Opt. **45**, 4254–4262 (2006).

[103] S. Bollanti, P. Di Lazzaro, F. Flora, L. Mezi, D. Murra, and a. Torre, "Conventional and modified Schwarzschild objective for EUV lithography: Design relations," Appl. Phys. B Lasers Opt. **85**, 603–610 (2006).

[104] S. Matsuyama, H. Nakamori, T. Goto, and T. Kimura, "Nearly diffraction-limited X-ray focusing with variable-numerical- aperture focusing optical system based on four deformable mirrors," Sci. Rep. **6**, 24801 (2016).

[105] H. Mimura, S. Handa, T. Kimura, H. Yumoto, D. Yamakawa, H. Yokoyama, S. Matsuyama, K. Inagaki, K. Yamamura, Y. Sano, K. Tamasaku, Y. Nishino, M. Yabashi, T. Ishikawa, and K. Yamauchi, "Breaking the 10nm barrier in hard-X-ray focusing," Nat. Phys. **6**, 122–125 (2010).

[106] H. C. Kang, H. Yan, R. P. Winarski, M. V. Holt, J. Maser, C. Liu, R. Conley, S. Vogt, A. T. MacRander, and G. B. Stephenson, "Focusing of hard x-rays to 16 nanometers with a multilayer Laue lens," Appl. Phys. Lett. **92** (2008).

[107] A. J. Morgan, M. Prasciolu, A. Andrejczuk, J. Krzywinski, A. Meents, D. Pennicard, H. Graafsma, A. Barty, R. J. Bean, M. Barthelmess, D. Oberthuer, O. Yefanov, A. Aquila, H. N. Chapman, and S. Bajt, "High numerical aperture multilayer Laue lenses." Sci. Rep. **5**, 9892 (2015).

[108] M. Prasciolu, a. F. G. Leontowich, J. Krzywinski, a. Andrejczuk, H. N. Chapman, and S. Bajt, "Fabrication of wedged multilayer Laue lenses," Opt. Mater. Express **5**, 748 (2015).

[109] C. Jacobsen, S. Williams, E. Anderson, M. Browne, C. Buckley, D. Kern, J. Kirz, M. Rivers, and X. Zhang, "Diffraction-limited imaging in a scanning transmission x-ray microscope," Opt. Commun. **86**, 351–364 (1991).

[110] A. L. D. Kilcoyne, T. Tyliszczak, W. F. Steele, S. Fakra, P. Hitchcock, K. Franck, E. Anderson, B. Harteneck, E. G. Rightor, G. E. Mitchell, A. P. Hitchcock, L. Yang, T. Warwick, and H. Ade, "Interferometer-controlled scanning transmission X-ray microscopes at the Advanced Light Source," Synchrotron Radiat. News **10**, 125–136 (2003).

[111] W. Chao, B. Harteneck, J. Liddle, E. Anderson, and D. Attwood, "Soft X-ray microscopy at a spatial resolution better than 15 nm," Nature **435**, 1210–1213 (2005).

[112] W. Chao, J. Kim, S. Rekawa, P. Fischer, and E. H. Anderson, "Demonstration of 12 nm resolution Fresnel zone plate lens based soft x-ray microscopy." Opt. Express **17**, 17669–17677 (2009).

[113] W. Chao, P. Fischer, T. Tyliszczak, S. Rekawa, E. Anderson, and P. Naulleau, "Real space soft x-ray imaging at 10 nm spatial resolution," Opt. Express **20**, 9777 (2012).

[114] F. Döring, a. L. Robisch, C. Eberl, M. Osterhoff, a. Ruhlandt, T. Liese, F. Schlenkrich, S. Hoffmann, M. Bartels, T. Salditt, and H. U. Krebs, "Sub-5 nm hard x-ray point focusing by a combined Kirkpatrick-Baez mirror and multilayer zone plate," Opt. Express **21**, 19311–19323 (2013).

[115] M. D. De Jonge, B. Hornberger, C. Holzner, D. Legnini, D. Paterson, I. McNulty, C. Jacobsen, and S. Vogt, "Quantitative phase imaging with a scanning transmission X-ray microscope," Phys. Rev. Lett. **100**, 1–4 (2008).

[116] A. Sakdinawat and D. Attwood, "Nanoscale X-ray imaging," Nat. Photonics **4**, 840–848 (2010).

[117] X. Huang, H. Miao, J. Steinbrener, J. Nelson, D. Shapiro, A. Stewart, J. Turner, and C. Jacobsen, "Signal-to-noise and radiation exposure considerations in conventional and diffraction x-ray microscopy." Opt. Express **17**, 13541–13553 (2009).

[118] R. W. Gerchberg and W. O. Saxton, "A Practical Algorithm for the Determination of Phase from Image and Diffraction Plane Pictures," Optik (Stuttg). **35**, 237–246 (1972).

[119] J. Fienup, "Reconstruction of an object from the modulus of its Fourier transform," Opt. Lett. **3**, 27–29 (1978).

[120] J. R. Fienup, "Phase retrieval algorithms: a comparison." Appl. Opt. **21**, 2758–69 (1982).

[121] J. R. Fienup, "Phase retrieval algorithms: a personal tour [Invited]." Appl. Opt. **52**, 45–56 (2013).

[122] J. Cederquist, J. Fienup, C. Marron, and R. Paxman, "Phase retrieval from experimental far-field speckle data," Otpics Lett. **13**, 619 (1988).

[123] M. J. Pérez-Ilzarbe, M. Nieto-Vesperinas, and R. Navarro, "Phase retrieval from experimental far-field intensity data," J. Opt. Soc. Am. A **7**, 434 (1990).

[124] I. K. Robinson, J. L. Libbert, I. a. Vartanyants, J. a. Pitney, D. M. Smilgies, D. L. Abernathy, and G. Grübel, "Coherent x-ray diffraction imaging of silicon oxide growth," Phys. Rev. B **60**, 9965–9972 (1999).

[125] J. Miao, P. Charalambous, J. Kirz, and D. Sayre, "Extending the methodology of X-ray crystallography to allow imaging of micrometre-sized non-crystalline specimens," Nature **400**, 342–344 (1999).

[126] H. Mimura, S. Matsuyama, H. Yumoto, H. Hara, K. Yamamura, Y. Sano, M. Shibahara, K. Endo, Y. Mori, Y. Nishlno, K. Tamasaku, M. Yabashi, T. Ishikawa, and K. Yamauchi, "Hard X-ray diffraction-limited nanofocusing with kirkpatrick-baez mirrors," Jpn. J. Appl. Phys. **44**, L539 – L542 (2005).

[127] I.-B. Sohn, M. S. Ahsan, Y.-C. Noh, H.-K. Choi, J.-T. Kim, and M.-J. Ko, "Fabrication of Fresnel zone plate lens in fused silica glass using femtosecond laser lithography technology," Opt. Eng. **53**, 055107 (2014).

[128] H. N. Chapman and K. A. Nugent, "Coherent lensless X-ray imaging," Nat. Photonics **4**, 833–839 (2010).

[129] J. Miao, R. L. Sandberg, and C. Song, "Coherent X-ray diffraction imaging," IEEE J. Sel. Top. Quant. Electron **18**, 399–410 (2011).

[130] D. Sayre, "Some implications of a theorem due to Shannon," Acta Crystallogr. **5**, 843–843 (1952).

[131] C. E. Shannon, "Communication in the Presence of Noise," Proc. IEEE **86**, 447–457 (1998).

[132] V. Elser, "Phase retrieval by iterated projections," J. Opt. Soc. Am. A **20**, 40–55 (2003).

[133] S. Marchesini, H. He, H. N. Chapman, S. P. Hau-Riege, A. Noy, M. R. Howells, U. Weierstall, and J. C. H. Spence, "X-ray image reconstruction from a diffraction pattern alone," Phys. Rev. B **68**, 140101 (2003).

[134] D. R. Luke, "Relaxed Averaged Alternating Reflections for Diffraction Imaging," Inverse Probl. **37**, 13 (2004).

[135] S. T. Thurman and J. R. Fienup, "Phase retrieval with signal bias." J. Opt. Soc. Am. A. Opt. Image Sci. Vis. **26**, 1008–14 (2009).

[136] D. E. Adams, L. S. Martin, M. D. Seaberg, D. F. Gardner, H. C. Kapteyn, and M. M. Murnane, "A generalization for optimized phase retrieval algorithms," Opt. Express **20**, 24778 (2012).

[137] M. Seaberg, D. Adams, E. Townsend, D. Raymondson, W. Schlotter, Y. Liu, C. Menoni, L. Rong, C. Chen, J. Miao, H. Kapteyn, and M. Murnane, "Ultrahigh 22 nm resolution coherent diffractive imaging using a desktop 13 nm high harmonic source," Opt. Express **19**, 22470–9 (2011).

[138] J. W. Goodman, <u>Introduction to Fourier Optics</u> (Roberts and Company Publishers, Greenwood Village, 2005), 3rd ed.

[139] J. Miao and D. Sayre, "On possible extensions of X-ray crystallography through diffraction-pattern oversampling research papers On possible extensions of X-ray crystallography through diffraction-pattern oversampling," Acta Crystallogr. **A56**, 596–605 (2000).

[140] J. Miao, D. Sayre, and H. N. Chapman, "Phase retrieval from the magnitude of the Fourier transforms of nonperiodic objects," J. Opt. Soc. Am. A **15**, 1662 (1998).

[141] J. Miao, T. Ishikawa, E. Anderson, and K. Hodgson, "Phase retrieval of diffraction patterns from noncrystalline samples using the oversampling method," Phys. Rev. B **67**, 174104 (2003).

[142] C. Song, D. Ramunno-Johnson, Y. Nishino, Y. Kohmura, T. Ishikawa, C.-C. Chen, T.-K. Lee, and J. Miao, "Phase retrieval from exactly oversampled diffraction intensity through deconvolution," Phys. Rev. B **75**, 012102 (2007).

[143] W. Hoppe, "Beugung im inhomogenen Primärstrahlwellenfeld," Acta Crystallogr. Sect. A **25**, 495–515 (1969).

[144] J. M. Rodenburg, "Ptychography and related diffractive imaging methods," Adv. Imaging Electron Phys. **150**, 87–184 (2008).

[145] J. Rodenburg, "Ptychography: early history and 3D scattering effects," in "Proc. SPIE Short-Wavelength Imaging Spectrosc. Sources," , vol. 8678 (2012), vol. 8678, pp. 1–10.

[146] B. C. McCallum and J. M. Rodenburg, "Two-dimensional demonstration of Wigner phase-retrieval microscopy in the STEM configuration," Ultramicroscopy **45**, 371–380 (1992).

[147] H. Faulkner and J. Rodenburg, "Movable Aperture Lensless Transmission Microscopy: A Novel Phase Retrieval Algorithm," Phys. Rev. Lett. **93**, 023903 (2004).

[148] J. M. Rodenburg and H. M. L. Faulkner, "A phase retrieval algorithm for shifting illumination," Appl. Phys. Lett. **85**, 4795 (2004).

[149] P. Thibault, M. Dierolf, A. Menzel, O. Bunk, C. David, and F. Pfeiffer, "High-resolution scanning x-ray diffraction microscopy." Science **321**, 379–82 (2008).

[150] A. Maiden and J. Rodenburg, "An improved ptychographical phase retrieval algorithm for diffractive imaging," Ultramicroscopy **109**, 1256–62 (2009).

[151] J. Rodenburg and R. H. T. Bates, "The theory of super-resolution electron microscopy via Wigner-distribution deconvolution," Phil. Trans. R. Soc. Lond. A **336**, 521–553 (1992).

[152] M. Humphry, B. Kraus, a.C. Hurst, a.M. Maiden, and J. Rodenburg, "Ptychographic electron microscopy using high-angle dark-field scattering for sub-nanometre resolution imaging," Nat. Commun. **3**, 730 (2012).

[153] J. C. H. Spence, U. Weierstall, and M. Howells, "Coherence and sampling requirements for diffractive imaging." Ultramicroscopy **101**, 149–52 (2004).

[154] P. Thibault, M. Dierolf, O. Bunk, A. Menzel, and F. Pfeiffer, "Probe retrieval in ptychographic coherent diffractive imaging," Ultramicroscopy **109**, 338–43 (2009).

[155] X. Huang, H. Yan, R. Harder, Y. Hwu, I. K. Robinson, and Y. S. Chu, "Optimization of overlap uniformness for ptychography," Opt. Express **22**, 12634 (2014).

[156] M. Guizar-Sicairos and J. Fienup, "Phase retrieval with transverse translation diversity: a nonlinear optimization approach," Opt. Express **16**, 7264–7278 (2008).

[157] P. Thibault and M. Guizar-Sicairos, "Maximum-likelihood refinement for coherent diffractive imaging," New J. Phys. **14**, 1–20 (2012).

[158] C. T. Putkunz, J. N. Clark, D. J. Vine, G. J. Williams, M. A. Pfeifer, E. Balaur, I. McNulty, K. A. Nugent, and A. G. Peele, "Phase-diverse coherent diffractive imaging: High sensitivity with low dose," Phys. Rev. Lett. **106**, 1–4 (2011).

[159] J. R. Fienup, "Invariant error metrics for image reconstruction." Appl. Opt. **36**, 8352–8357 (1997).

[160] S. Marathe, S. S. Kim, S. N. Kim, C. Kim, H. C. Kang, P. V. Nickles, and D. Y. Noh, "Coherent diffraction surface imaging in reflection geometry," Opt. Express **18**, 7253–62 (2010).

[161] S. Roy, D. Parks, K. A. Seu, R. Su, J. J. Turner, W. Chao, E. H. Anderson, S. Cabrini, and S. D. Kevan, "Lensless X-ray imaging in reflection geometry," Nat. Photonics **5**, 243–245 (2011).

[162] T. Sun, Z. Jiang, J. Strzalka, L. Ocola, and J. Wang, "Three-dimensional coherent X-ray surface scattering imaging near total external reflection," Nat. Photonics **6**, 586 –590 (2012).

[163] T. Harada, M. Nakasuji, Y. Nagata, T. Watanabe, and H. Kinoshita, "Phase Imaging of Extreme-Ultraviolet Mask Using Coherent Extreme-Ultraviolet Scatterometry Microscope," Jpn. J. Appl. Phys. **52**, 06GB02 (2013).

[164] M. Zürch, C. Kern, and C. Spielmann, "XUV coherent diffraction imaging in reflection geometry with low numerical aperture," Opt. Express **21**, 21131–21147 (2013).

[165] D. F. Gardner, B. Zhang, M. D. Seaberg, L. S. Martin, D. E. Adams, F. Salmassi, E. Gullikson, H. Kapteyn, and M. Murnane, "High numerical aperture reflection mode coherent diffraction microscopy using off-axis apertured illumination," Opt. Express **20**, 19050–9 (2012).

[166] J. W. Cooley and J. W. Tukey, "An Algorithm for Machine Calculation of Complex Fourier Series," Math. Comput. **19**, 297–301 (1965).

[167] M. Frigo and S. G. Johnson, "The design and implementation of FFTW3," Proc. IEEE **93**, 216–231 (2005).

[168] B. Zhang, D. F. Gardner, M. D. Seaberg, E. R. Shanblatt, H. C. Kapteyn, M. M. Murnane, and D. E. Adams, "High contrast 3D imaging of surfaces near the wavelength limit using tabletop EUV ptychography," Ultramicroscopy **158**, 98–104 (2015).

[169] M. Seaberg, B. Zhang, D. Gardner, E. Shanblatt, M. Murnane, H. Kapteyn, and D. Adams, "Tabletop Nanometer Extreme Ultraviolet Imaging in an Extended Reflection Mode Using Coherent Fresnel Ptychography : supplementary material," Optica **1**, 1–4 (2014).

[170] F. Zhang, I. Peterson, J. Vila-Comamala, A. Diaz, F. Berenguer, R. Bean, B. Chen, A. Menzel, I. Robinson, and J. Rodenburg, "Translation position determination in ptychographic coherent diffraction imaging," Opt. Express **21**, 13592–13606 (2013).

[171] D. Shapiro, P. Thibault, T. Beetz, V. Elser, M. Howells, C. Jacobsen, J. Kirz, E. Lima, H. Miao, A. M. Neiman, and D. Sayre, "Biological imaging by soft x-ray diffraction microscopy." Proc. Natl. Acad. Sci. U. S. A. **102**, 15343–6 (2005).

[172] H. N. Chapman, A. Barty, S. Marchesini, A. Noy, S. P. Hau-riege, C. Cui, M. R. Howells, R. Rosen, H. He, J. C. H. Spence, U. Weierstall, T. Beetz, C. Jacobsen, and D. Shapiro, "High-resolution ab initio three-dimensional x-ray diffraction microscopy," J. Opt. Soc. Am. A **23** (2006).

[173] D. F. Gardner, M. Tanksalvala, E. R. Shanblatt, X. Zhang, B. R. Galloway, C. L. Porter, R. Karl-Jr., C. Bevis, D. E. Adams, H. C. Kapteyn, M. M. Murnane, and G. F. Mancini, "Subwavelength coherent imaging of periodic samples using a 13.5 nm tabletop high harmonic light source," Submitted (2016).

[174] P. Thibault, M. Dierolf, A. Menzel, O. Bunk, C. David, and F. Pfeiffer, "High-resolution scanning x-ray diffraction microscopy," Science **321**, 379–82 (2008).

[175] D. Sayre, "Prospects for long wavelength X-Ray microscopy and diffraction," in "Imaging Process. coherence Phys.", , vol. 112 (1980), vol. 112, pp. 229–235.

[176] R. W. Falcone and J. Bokor, "Dichroic beam splitter for extreme-ultraviolet and visible radiation," Opt. Lett. **8**, 21–23 (1983).

[177] Y. Nagata, Y. Nabekawa, and K. Midorikawa, "Development of high-throughput, high-damage-threshold beam separator for 13 nm high-order harmonics." Opt. Lett. **31**, 1316–1318 (2006).

[178] S. Ichimaru, M. Hatayama, T. Ohchi, E. M. Gullikson, and S. Oku, "Performance of a ruthenium beam separator used to separate soft x rays from light generated by a high-order harmonic light source," Appl. Opt. **55**, 984–988 (2016).

[179] E. R. Shanblatt, C. L. Porter, D. F. Gardner, G. F. Mancini, R. M. Karl, M. D. Tanksalvala, C. S. Bevis, V. H. Vartanian, H. C. Kapteyn, D. E. Adams, and M. M. Murnane, "Quantitative Chemically-Specific Coherent Diffractive Imaging of Buried Interfaces using a Tabletop EUV Nanoscope," Nano Lett. **19**, 5444–5450 (2016).

[180] B. L. Henke, E. M. Gullikson, and J. C. Davis, "X-Ray Interactions: Photoabsorption, Scattering, Transmission, and Reflection at E = 50-30,000 eV, Z = 1-92," At. Data Nucl. Data Tables **54**, 181–342 (1993).

[181] A. M. Maiden, M. J. Humphry, F. Zhang, and J. M. Rodenburg, "Superresolution imaging via ptychography." J. Opt. Soc. Am. A **28**, 604–612 (2011).

[182] M. Odstrcil, J. Bussmann, D. Rudolf, R. Bresenitz, J. Miao, W. S. Brocklesby, and L. Juschkin, "Ptychographic imaging with a compact gasdischarge plasma extreme ultraviolet light source," Opt. Lett. **40**, 5574–5577 (2015).

[183] P. Thibault and A. Menzel, "Reconstructing state mixtures from diffraction measurements." Nature **494**, 68–71 (2013).

[184] D. J. Batey, D. Claus, and J. M. Rodenburg, "Information multiplexing in ptychography," Ultramicroscopy **138**, 13–21 (2013).

[185] T. B. Edo, D. J. Batey, a. M. Maiden, C. Rau, U. Wagner, Z. D. Pešić, T. a. Waigh, and J. M. Rodenburg, "Sampling in x-ray ptychography," Phys. Rev. A - At. Mol. Opt. Phys. **87**, 1–8 (2013).

[186] D. J. Batey, T. B. Edo, C. Rau, U. Wagner, Z. D. Pesic, T. A. Waigh, and J. M. Rodenburg, "Reciprocal-space up-sampling from real-space oversampling in x-ray ptychography," Phys. Rev. A - At. Mol. Opt. Phys. **89**, 1–5 (2014).

[187] A. M. Maiden, M. J. Humphry, and J. M. Rodenburg, "Ptychographic transmission microscopy in three dimensions using a multi-slice approach." J. Opt. Soc. Am. A **29**, 1606–1614 (2012).

[188] T. M. Godden, R. Suman, M. J. Humphry, J. M. Rodenburg, and A. M. Maiden, "Ptychographic microscope for three-dimensional imaging," Opt. Express **22**, 12513–12523 (2014).

[189] A. Suzuki, S. Furutaku, K. Shimomura, K. Yamauchi, Y. Kohmura, T. Ishikawa, and Y. Takahashi, "High-resolution multislice X-ray ptychography of extended thick objects," Phys. Rev. Lett. **112**, 1–5 (2014).

[190] K. Shimomura, A. Suzuki, M. Hirose, and Y. Takahashi, "Precession x-ray ptychography with multislice approach," Phys. Rev. B - Condens. Matter Mater. Phys. **91**, 1–5 (2015).

[191] K. M. Hoogeboom-Pot, J. N. Hernandez-Charpak, E. H. Anderson, X. Gu, R. Yang, M. M. Murnane, H. C. Kapteyn, and D. Nardi, "A new regime of nanoscale thermal transport: collective diffusion counteracts dissipation inefficiency," PNAS **112**, 4846–4851 (2015).

[192] D. D. Hickstein, F. Dollar, J. A. Gaffney, M. E. Foord, G. M. Petrov, B. B. Palm, K. E. Keister, J. L. Ellis, C. Ding, S. B. Libby, J. L. Jimenez, H. C. Kapteyn, M. M. Murnane, and W. Xiong, "Observation and control of shock waves in individual nanoplasmas," Phys. Rev. Lett. **112**, 1–5 (2014).

[193] S. Mathias, C. La-O-Vorakiat, J. M. Shaw, E. Turgut, P. Grychtol, R. Adam, D. Rudolf, H. T. Nembach, T. J. Silva, M. Aeschlimann, C. M. Schneider, H. C. Kapteyn, and M. M. Murnane, "Ultrafast element-specific magnetization dynamics of complex magnetic materials on a table-top," J. Electron Spectros. Relat. Phenomena **189**, 164–170 (2013).

[194] E. Turgut, C. La-O-Vorakiat, J. M. Shaw, P. Grychtol, H. T. Nembach, D. Rudolf, R. Adam, M. Aeschlimann, C. M. Schneider, T. J. Silva, M. M. Murnane, H. C. Kapteyn, and S. Mathias, "Controlling the competition between optically induced ultrafast spin-flip scattering and spin transport in magnetic multilayers," Phys. Rev. Lett. **110**, 197201 (2013).

[195] M. Murnane and J. Miao, "Optics: Ultrafast X-ray photography," Nature **460**, 1088–90 (2009).

[196] H. N. Chapman, S. P. Hau-Riege, M. J. Bogan, S. Bajt, A. Barty, S. Boutet, S. Marchesini, M. Frank, B. W. Woods, W. H. Benner, R. a. London, U. Rohner, A. Szöke, E. Spiller, T. Möller, C. Bostedt, D. a. Shapiro, M. Kuhlmann, R. Treusch, E. Plönjes, F. Burmeister, M. Bergh, C. Caleman, G. Huldt, M. M. Seibert, and J. Hajdu, "Femtosecond time-delay X-ray holography." Nature **448**, 676–9 (2007).

[197] A. A. Khorshad, K. Hassani, and M. T. Tavassoly, "Nanometer displacement measurement using Fresnel diffraction." Appl. Opt. **51**, 5066–72 (2012).

[198] S. Carbajo, I. D. Howlett, F. Brizuela, K. S. Buchanan, M. C. Marconi, W. Chao, E. H. Anderson, I. Artioukov, a. Vinogradov, J. J. Rocca, and C. S. Menoni, "Sequential single-shot imaging of nanoscale dynamic interactions with a table-top soft x-ray laser." Opt. Lett. **37**, 2994–6 (2012).

[199] A. Barty, S. Boutet, M. J. Bogan, S. Hau-Riege, S. Marchesini, K. Sokolowski-Tinten, N. Stojanovic, R. Tobey, H. Ehrke, A. Cavalleri, S. Düsterer, M. Frank, S. Bajt, B. W. Woods, M. M. Seibert, J. Hajdu, R. Treusch, and H. N. Chapman, "Ultrafast single-shot diffraction imaging of nanoscale dynamics," Nat. Photonics **2**, 415–419 (2008).

[200] a. Ravasio, D. Gauthier, F. R. N. C. Maia, M. Billon, J. P. Caumes, D. Garzella, M. Géléoc, O. Gobert, J. F. Hergott, a. M. Pena, H. Perez, B. Carré, E. Bourhis, J. Gierak, A. Madouri, D. Mailly, B. Schiedt, M. Fajardo, J. Gautier, P. Zeitoun, P. H. Bucksbaum, J. Hajdu, and H. Merdji, "Single-shot diffractive imaging with a table-top femtosecond soft X-ray laser-harmonics source," Phys. Rev. Lett. **103**, 028104 (2009).

[201] K. W. DeLong, R. Trebino, J. Hunter, and W. E. White, "Frequency-resolved optical gating with the use of second-harmonic generation," J. Opt. Soc. Am. B **11**, 2206 (1994).

[202] Q. Li, K. Hoogeboom-Pot, D. Nardi, M. M. Murnane, H. C. Kapteyn, M. E. Siemens, E. H. Anderson, O. Hellwig, E. Dobisz, B. Gurney, R. Yang, and K. A. Nelson, "Generation and control of ultrashort-wavelength two-dimensional surface acoustic waves at nanoscale interfaces," Phys. Rev. B - Condens. Matter Mater. Phys. **85**, 195431 (2012).

[203] K. M. Hoogeboom-Pot, E. Turgut, J. N. Hernandez-Charpak, J. M. Shaw, H. C. Kapteyn, M. M. Murnane, and D. Nardi, "Nondestructive Measurement of the Evolution of Layer-Specific Mechanical Properties in Sub-10 nm Bilayer Films," Nano Lett. **16**, 4773–4778 (2016).

[204] J. H. Underwood and T. W. Barbee, "Layered synthetic microstructures as Bragg diffractors for X rays and extreme ultraviolet: theory and predicted performance," Appl. Opt. **20**, 3027 (1981).

[205] O. Kfir, P. Grychtol, E. Turgut, R. Knut, D. Zusin, D. Popmintchev, T. Popmintchev, H. Nembach, J. M. Shaw, A. Fleischer, H. Kapteyn, M. Murnane, and O. Cohen, "Generation of bright phase-matched circularly-polarized extreme ultraviolet high harmonics," Nat. Photonics pp. 1–7 (2014).

[206] D. D. Hickstein, F. J. Dollar, P. Grychtol, J. L. Ellis, R. Knut, C. Hernández-García, D. Zusin, C. Gentry, J. M. Shaw, T. Fan, K. M. Dorney, A. Becker, A. Jaroń-Becker, H. C. Kapteyn,

M. M. Murnane, and C. G. Durfee, "Non-collinear generation of angularly isolated circularly polarized high harmonics," Nat. Photonics **9** (2015).

[207] A. Tripathi, J. Mohanty, S. H. Dietze, O. G. Shpyrko, E. Shipton, E. E. Fullerton, S. S. Kim, and I. McNulty, "Dichroic coherent diffractive imaging." Proc. Natl. Acad. Sci. U. S. A. **108**, 13393–8 (2011).

[208] C. Donnelly, V. Scagnoli, M. Guizar-Sicairos, M. Holler, F. Wilhelm, F. Guillou, A. Rogalev, C. Detlefs, A. Menzel, J. Raabe, and L. J. Heyderman, "High Resolution Hard X-ray Magnetic Imaging with Dichroic Ptychography," Phys. Rev. B **064421**, 1–5 (2016).

[209] S. Zayko, E. Mönnich, M. Sivis, D.-D. Mai, T. Salditt, S. Schäfer, and C. Ropers, "Coherent diffractive imaging beyond the projection approximation: waveguiding at extreme ultraviolet wavelengths," Opt. Express **23**, 19911 (2015).

[210] S. O. Kim, H. H. Solak, M. P. Stoykovich, N. J. Ferrier, J. J. De Pablo, and P. F. Nealey, "Epitaxial self-assembly of block copolymers on lithographically defined nanopatterned substrates." Nature **424**, 411–4 (2003).

[211] B. Zhang, D. F. Gardner, M. D. Seaberg, E. R. Shanblatt, C. Porter, R. Karl-Jr., C. Mancuso, H. C. Kapteyn, M. M. Murnane, and D. E. Adams, "Ptychographic Hyperspectral Spectromicroscopy with an Extreme Ultraviolet High Harmonic Comb," Opt. Express **24**, 18745 (2016).

[212] R. Karl, C. Bevis, R. Lopez-Rios, J. Reichanadter, D. Gardner, C. Porter, E. Shanblatt, M. Tanksalvala, G. F. Mancini, M. Murnane, H. Kapteyn, and D. Adams, "Spatial, spectral, and polarization multiplexed ptychography," Opt. Express **23**, 30250–30258 (2015).

[213] A. Fleischer, O. Kfir, T. Diskin, P. Sidorenko, and O. Cohen, "Spin angular momentum and tunable polarization in high-harmonic generation," Nat. Photonics **8**, 543–549 (2014).

[214] X. Shi, P. Fischer, V. Neu, D. Elefant, J. C. T. Lee, D. A. Shapiro, M. Farmand, T. Tyliszczak, H. W. Shiu, S. Marchesini, S. Roy, and S. D. Kevan, "Soft x-ray ptychography studies of nanoscale magnetic and structural correlations in thin SmCo5 films," Appl. Phys. Lett. **108** (2016).

[215] B. Zhang, D. F. Gardner, M. D. Seaberg, E. R. Shanblatt, C. Porter, R. Karl-Jr., C. Mancuso, H. C. Kapteyn, M. M. Murnane, and D. E. Adams, "Ptychographic Hyperspectral Spectromicroscopy with an Extreme Ultraviolet High Harmonic Comb," Opt. Express **24**, 98–104 (2016).

[216] U. O. Edinburgh, "Topic 2: Scalar Diffraction," http://www2.ph.ed.ac.uk/~wjh/teaching /mo/slides/scalar/scalar.pdf **Autumn Ter**.

[217] J. M. Cowley, <u>Diffraction Physics</u> (Elsevier Science B.V., New York, 1995), 3rd ed.

Appendix A

From Maxwell to Fraunhofer

In coherent diffractive imaging (CDI), it is assumed the diffracted light collected on the detector is proportional to the Fourier Transform of the object. In this appendix, the assumptions and their applicability are discussed. Starting with Maxwell's equations in vacuum, the wave equation is derived. Then using a Green's function approach, the outline of a derivation is given to model the diffraction from an aperture. In the end, an expression for Fresnel and Fraunhofer diffraction is given with comments on their appropriate use. [1]

A.1   The Wave Equation from Maxwell's Equations

Due to EUV absorption by atmosphere, the EUV imaging demonstrations are in vacuum (10^{-6} Torr) in the absence of free charge, thus simplifying Maxwell's equations to

$$\nabla \times \vec{E} = -\mu_0 \frac{\partial \vec{H}}{\partial t} \tag{A.1}$$

$$\nabla \times \vec{H} = \epsilon_0 \frac{\partial \vec{E}}{\partial t} \tag{A.2}$$

$$\nabla \cdot \epsilon_0 \vec{E} = 0 \tag{A.3}$$

$$\nabla \cdot \mu_0 \vec{H} = 0 \tag{A.4}$$

---

[1] The notation and derivation presented here closely follows Goodman [138]

where $\vec{E}$ is the electric field, $\vec{H}$ is the magnetic field, μ_0 is the permeability of free space, and ϵ_0 is the permittivity of free space. Applying the curl operator ($\nabla\times$) to Eq. A.1 and switching the order of the time and space derivatives yields

$$\nabla \times \nabla \times \vec{E} = -\mu_0 \frac{\partial(\nabla \times \vec{H})}{\partial t}. \tag{A.5}$$

The application of the vector identity $\nabla \times (\nabla \times \vec{E}) = \nabla(\nabla \cdot \vec{E}) - \nabla^2\vec{E})$ and substituting in Eq. A.2 gives the following wave equation

$$\nabla^2\vec{E} - \frac{1}{c^2}\frac{\partial^2\vec{E}}{\partial t^2} = 0 \tag{A.6}$$

where c is the speed of light given by

$$c = \frac{1}{\sqrt{\mu_0\epsilon_0}}. \tag{A.7}$$

The same procedure can be done with the magnetic field resulting in

$$\nabla^2\vec{H} - \frac{1}{c^2}\frac{\partial^2\vec{H}}{\partial t^2} = 0. \tag{A.8}$$

In a vacuum, the medium is linear, isotropic, homogeneous, and non-dispersive, therefore each x, y and z component of the electric and magnetic fields can be described by single scalar wave equation:

$$\nabla^2 u - \frac{1}{c^2}\frac{\partial^2 u}{\partial t^2} = 0. \tag{A.9}$$

The solution is

$$u = Re[U(P)e^{-i2\pi\nu t}] \tag{A.10}$$

where $Re[\ ]$ signifies the real part and $U(P)$ is a complex function of position given by

$$U(P) = A(P)e^{i\phi(P)} \tag{A.11}$$

where ν is the frequency, $A(P)$ is the amplitude, and $\phi(P)$ is the phase. Both $A(P)$ and $\phi(P)$ are functions of position, P. Writing the solution using U(P) allows spatial and temporal dependence to be separated. Plugging in Eq. A.10 into Eq. A.9 yields the Helmholtz equation:

$$(\nabla^2 + k^2)U = 0 \tag{A.12}$$

with

$$k = 2\pi\frac{\nu}{c} = \frac{2\pi}{\lambda} \tag{A.13}$$

where λ is the wavelength. The monochromatic plane wave, $U = U_0 e^{i(kx-\omega t)}$, is a solution, with $\omega = 2\pi\nu$, but a more complex solution is needed to describe the diffraction from an arbitrary waveform through an arbitrary planar screen.

A.2   Diffraction by a Planar Screen

To calculate the diffraction by a planar screen, Green's theorem is used and is stated as follows:

$$\int\int\int_V (U\nabla^2 G - G\nabla^2 U)dv = \int\int_S \left(U\frac{\partial G}{\partial n} - \frac{\partial U}{\partial n}\right)ds \tag{A.14}$$

where V is a volume, S is a closed surface, $\partial/\partial n$ points in the outward normal direction, and G is an auxiliary function, or Green s function, which needs to be carefully chosen. The first Green function considered is the free space Green's function,

$$G_K = \frac{e^{ikr_{01}}}{r_{01}}, \tag{A.15}$$

which used by Kirchhoff to solve for the diffraction from a point source through an aperture in a planar screen, where r_{01} is the magnitude of the vector $\vec{r}_{01}$ that points from P_0 to P_1 (see Fig. A.1).

Using the free space Green's function leads internal inconsistencies in the boundary conditions. To avoid inconsistencies, Rayleigh-Sommerfeld used the following Green's functions:

$$G_- = \frac{e^{ikr_{01}}}{r_{01}} - \frac{e^{ik\tilde{r}_{01}}}{\tilde{r}_{01}} \tag{A.16}$$

$$G_+ = \frac{e^{ikr_{01}}}{r_{01}} + \frac{e^{ik\tilde{r}_{01}}}{\tilde{r}_{01}} \tag{A.17}$$

In these Green's functions a mirror point is used on the opposite side of the screen from P_0 (see Fig. A.2) with $\tilde{r}_{01}$ is the length of the vector from $\tilde{P}_0$ to P_1.
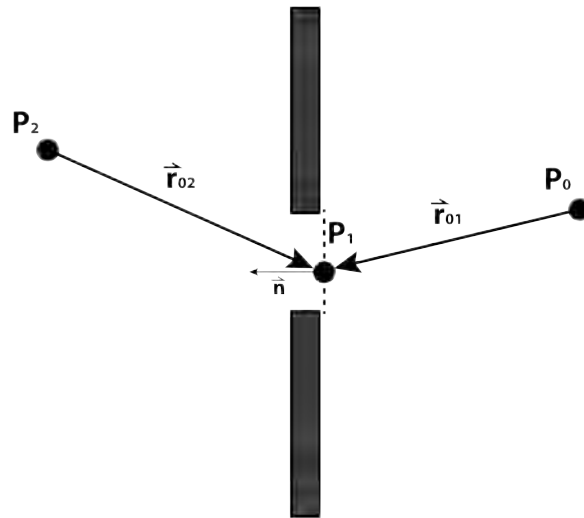
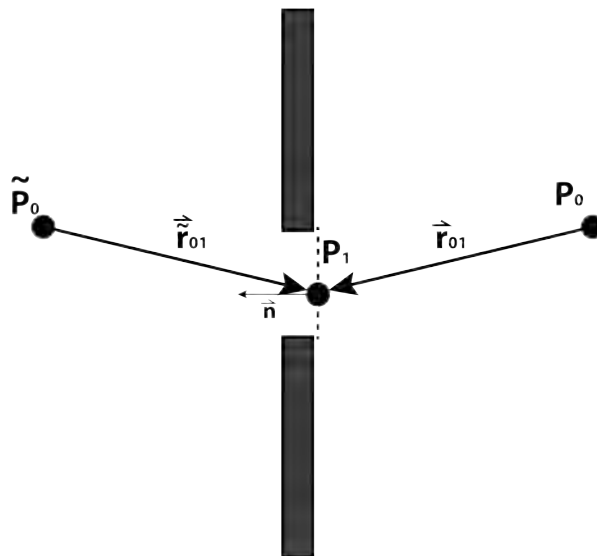Figure A.1: **Diffraction from Planar Screen from a Point Source**

Figure A.2: **Mirror Point Source**

Using Green's Theorem (Eq. A.14) and the above choices of Green's functions leads to

$$U(P_0) = \frac{A}{i\lambda} \int \int_{\Sigma} \frac{e^{ik(r_{21}+r_{01})}}{r_{21}r_{01}} \Psi ds \tag{A.18}$$

where A is the amplitude of the point source, and Σ is the open area in the screen, and Ψ is the obliquity factor and depends of the choice of green function. Using the free space Green's function, as used in the Kirchhoff approach, results in

$$\Psi = \frac{1}{2}\Big(\cos(\vec{n}, \vec{r}_{01}) - \cos(\vec{n}, \vec{r}_{21}) \Big) \tag{A.19}$$

while using the Rayleigh-Sommerfeld Green's function results in

$$\Psi = \cos(\vec{n}, \vec{r}_{01}) \tag{A.20}$$

and

$$\Psi = -\cos(\vec{n}, \vec{r}_{21}) \tag{A.21}$$

for the G_- and G_+, respectively. As long as the wave is observed many wavelengths away from the aperture, and the aperture is is much greater than the wavelength, there is negligible difference between the obliquity factors. Instead of point sources, attention is turned towards an arbitrary wavefront incident on the aperture.

A.3   Huygens Principle

With inspiration from Huygens principle - each point of a wavefront can be described by a spherically expanding wave - the wavefront incident on the screen at the opening can be described by a superposition of spherically expanding waves. As discussed above, the obliquity factors are nearly identical if we are far enough away from the aperture, thus we chose the obliquity factor from the use of the G_- Green's function. Huygens principle is given by

$$U(P_0) = \frac{1}{i\lambda} \int \int_{\Sigma} U(P_1) \frac{e^{ikr_{01}}}{r_{01}} \cos\theta ds \tag{A.22}$$

where $U(P_1)$ is given by Eq. A.11. For numerical calculations, it's easier to work in Cartesian coordinates. Following Fig. A.3, the diffracting screen is placed in the (ξ, η) plane and perpendicular
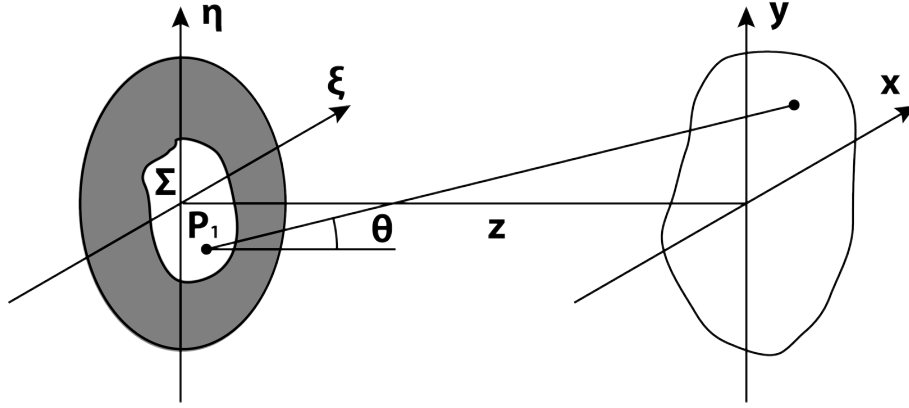
Figure A.3: **Diffraction Geometry in Cartesian Coordinates**

to the z axis. The detection plane lies in the (x, y) plane and we assume the light is incident from the left. With this geometry the cosine term is given by

$$\cos \theta = \frac{z}{r_{01}} \tag{A.23}$$

and Huygens Eq. A.22 can be written as

$$U(P_0) = \frac{z}{i\lambda} \int \int_\Sigma U(\xi, \eta) \frac{e^{ikr_{01}}}{r_{01}^2} d\xi d\eta \tag{A.24}$$

where the distance between P_1 and P_0 is

$$r_{01} = \sqrt{z^2 + (x - \xi)^2 + (y - \eta)^2}. \tag{A.25}$$

A.4 The Fresnel Approximation

In the Fresnel approximation, r_{01} is approximated with a binomial expansion resulting in

$$r_{01} \approx z \left[1 + \frac{1}{2} \left(\frac{x - \xi}{z} \right)^2 + \frac{1}{2} \left(\frac{y - \eta}{z} \right)^2 \right]. \tag{A.26}$$

Plugging in the approximation of r_{01} into Eq. A.24 and assuming no light is transmitted outside of the aperture Σ yields the Fresnel diffraction integral:

$$U(x, y) = \frac{e^{ikz}}{i\lambda z} e^{i\frac{k}{2z}(x^2 + y^2)} \int \int_{-\infty}^{+\infty} \left\{ U(\xi, \eta) e^{i\frac{k}{2z}(\xi^2 + \eta^2)} \right\} e^{-i\frac{2\pi}{\lambda z}(x\xi + y\eta)} d\xi d\eta. \tag{A.27}$$

This equation can be written in a more illuminating fashion as follows

$$U(x,y) = A(x,y)\hat{F}\Big[B(\xi,\eta)U(\xi,\eta)\Big] \tag{A.28}$$

where $\hat{F}$ is the Fourier transform with A and B multiplicative factors. This form of the Fresnel integral is particularly useful for computational techniques because the Fourier transform can be accomplished with the efficient, and discrete, Fast Fourier Transform routine [166, 167].

The accuracy of the Fresnel approximation depends on the contribution from higher order terms in the binomial expansion of Eq. A.25. A strict condition for accuracy is satisfied as long as

$$z^3 \gg \frac{\pi}{4\lambda}\big[(x-\xi)^2 + (y-\eta)^2\big]^2_{max} \tag{A.29}$$

A.5   Fraunhofer Diffraction

The Fraunhofer approximation is valid when observing the diffraction in the far-field such that the curvature of the wavefront incident on the screen is negligible. This is valid if

$$z \gg \frac{k(\xi^2 + \eta^2)_{max}}{2}. \tag{A.30}$$

When the approximation is valid, the multiplicative factor B in the Fresnel integral (Eq. A.28) goes to one, giving the Fraunhofer diffraction formula:

$$U(x,y) = A(x,y)\hat{F}\Big[U(\xi,\eta)\Big]. \tag{A.31}$$

Fraunhofer diffraction is the Fourier Transform of the of the field at the aperture, evaluated at frequencies $f_x = x/\lambda z$ and $f_y = y/\lambda z$, again allowing the use of the Fast Fourier Transform routine (CITE).

A.6   Angular Spectrum of Plane Waves

The angular spectrum of plane wave propagation method is used to discribe the diffraction between two planes, as shown in Fig. A.4. In this method, the Helmholtz equation is applied to the Fourier transform of the waveform and a propagator is defined. [2]

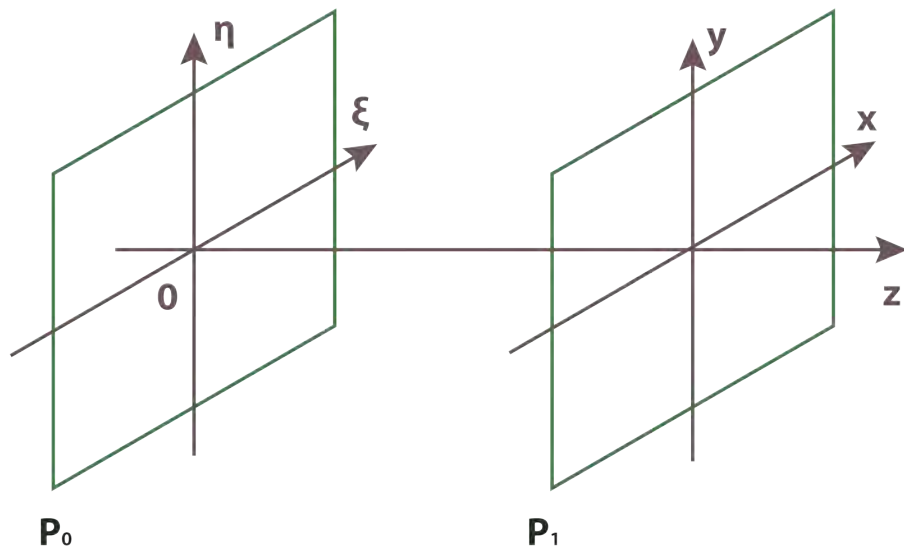[2] The derivation and notation here closely follows Ref. [216]

Figure A.4: **Angular Spectrum Propagation Between Two Planes**

To begin, it is assumed the wavefront at the $z = 0$ plane $(u_0(\xi, \eta))$ is known. The Fourier Transform at the unknown plane is taken, given by

$$U_1(u, v, z) = \int \int u_1(x, y, z)e^{-i2\pi(ux+vy)}dxdy \tag{A.32}$$

with the inverse transform given by

$$u_1(x, y, z) = \int \int U_1(u, v, z)e^{i2\pi(ux+vy)}dudv \tag{A.33}$$

From Eq. A.33, and Fourier transform theory, it is seen that $u_1(x, y, z)$ is composed of a linear combination of $U_1(u, v, z)e^{i2\pi(ux+vy)}$, which must also be a solution to the Helmholtz equation, Eq. A.12, and results in the following expression (again with $k = 2\pi/\lambda$):

$$\left(\nabla^2 + k\right)U_1(u, v, z)e^{i2\pi(ux+vy)} = 0 \tag{A.34}$$

Application of the Laplace operator results in

$$\frac{\partial^2 U_1}{\partial z^z} + (2\pi\gamma)^2 U_1 = 0 \tag{A.35}$$

with

$$\gamma = \sqrt{\frac{1}{\lambda^2} - u^2 - v^2}. \tag{A.36}$$

This differential equation can be solved with the initial condition of U_0 given by

$$U_0(u, v, 0) = \int \int u_0(\xi, \eta, 0)e^{-i2\pi(\xi u+\eta v)}d\xi d\eta = F[u_0]. \tag{A.37}$$

Using the initial condition, the solution to Eq. A.35 is

$$U_1(u, v, z) = F[u_0]e^{i2\pi\gamma z}. \tag{A.38}$$

Now taking the inverse Fourier transform

$$u_1(x, y, z) = \int \int F[u_0]e^{i2\pi\gamma z}e^{i2\pi(ux+vy)}dudv, \tag{A.39}$$

which can be written as

$$u_1(x, y, z) = F^{-1}\left[F[u_0]e^{i2\pi\gamma z}\right]. \tag{A.40}$$

From this expression, the field at the second plane, P_1, can be calculated from the first plane P_0 using Fourier Transforms and a propagation function in frequency space:

$$H(u, v, z) = e^{i2\pi\gamma z}. \tag{A.41}$$

At large z distances, the propagation function becomes highly oscillatory an cannot be sampled properly for numerical calculations. The angular spectrum of plane wave method is best for near field calculations.

A.7   Propagation Applicability and the Fresnel Number

In this appendix, three methods of wavefront propagation have been discussed. The applicability of each, in practice, can be characterized by the Fresnel number, given by

$$F = \frac{a^2}{L\lambda} \tag{A.42}$$

where a is the characteristic size of the aperture, L is the distance from the diffracting screen to the observation plane, and λ is the wavelength. When $F \gg 1$, the near-field, use the angular spectrum of plane wave method. When $F \sim 1$ use Fresnel propagation. And when $F \ll 1$, use the far-field approximation of Fraunhofer.

Appendix B

Tilted Plane Correction

When collecting diffraction patterns from a sample at high numerical aperture, there is a non-linear mapping of frequencies onto the detector. If the sample normal is not parallel to the incident beam, then the mapping is also asymmetrical. The tilted plane correction algorithm re-maps the collected diffraction patterns such that the frequencies are sampled on a linear grid. The re-mapping allows the use of the Fast Fourier Transform algorithms [166, 167] to propagate between the object and detector plane greatly increasing the reconstruction speed of the phase retrieval algorithms [165, 168, 169, 179].

B.1   Normal Incidence Geometry

Before considering the non-normal geometry, normal incidence illumination is described first. Figure B.1a shows the coordinate system used. The sample, S, lies in the (x', y') plane with the incident illumination pointing in the $\hat{z}'$ direction. The normal vector of the sample, $\hat{n}_s$ also points in the $\hat{z}'$ direction. Points within the sample plane are described with polar coordinates: $\vec{r}'$ and ϕ.

The detector, D, is parallel to the sample plane, and lies in the (x, y) plane. The normal vector of the detector, $\hat{n}_D$ points in the negative $\hat{z}$ direction. The distance from the center of the sample to the center of the detector is given by R. The origin of the detector coordinate system is at the center of the sample.
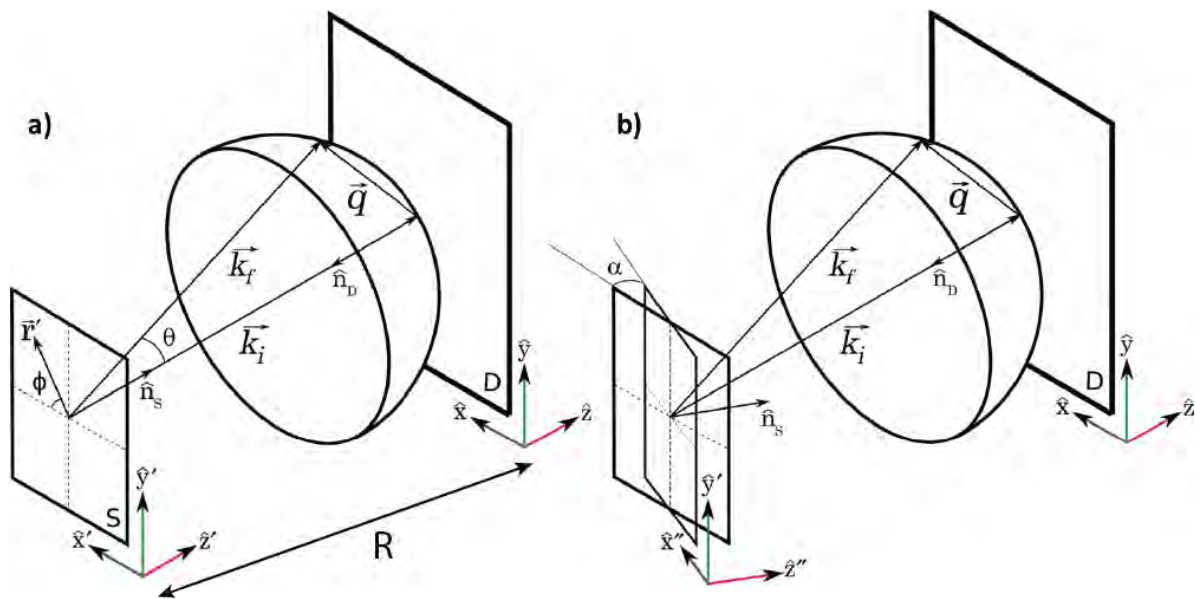
Figure B.1: **Coordinate Definitions** a) The coordinate system used for a normally incident illumination. b) The coordinate system used for a non-normal incident illumination. Figure adapted from Gardner et al. [165]

B.2 Scattering with Normal Incidence Illumination

The far-field diffracted pattern, $f(\vec{q})$, can be described by the first Born appropriation,

$$f(\vec{q}) = \frac{\mu}{4\pi} \int \Phi(\vec{r}')e^{-2\pi i \vec{q} \cdot \vec{r}'} d\vec{r}' \tag{B.1}$$

where μ describes the strength of the interaction with the potential Φ, and $\vec{q}$ is the momentum transfer vector [217]. The momentum transfer vector is the incident wave vector subtracted from the scattered vector: $\vec{q} = \vec{k}_f - \vec{k}_i$. The angle between $\vec{k}_f$ and $\vec{k}_i$ is θ.

Due to conversation of momentum, and the assumed elastic scattering, the magnitude of $\vec{k}_f$ and $\vec{k}_i$ are the same, $|\vec{k}| = 2\pi/\lambda = k_0$, where λ is the wavelength of illumination. Therefore, the scattered light lies on a spherical surface, which is called the Ewald sphere (see Fig. B.1). The mapping of the Ewald sphere onto a flat detector is the origin of the non-linear mapping, which becomes more evident with increasing numerical aperture.

The momentum transfer vector, when $\vec{k}_i = k_0 \hat{z}$, is written in the detector coordinate system as

$$\vec{q}(x, y, z) = k_0 \big[\cos \phi \sin \theta \hat{x} + \sin \phi \sin \theta \hat{y} + (\cos \theta - 1)\hat{z} \big]. \tag{B.2}$$

If the diffraction is collected at low NA, the small angle approximation can be used for theta, giving

$$\vec{q} = k_0 \big[\cos \phi \hat{x} + \sin \phi \hat{y} \big]. \tag{B.3}$$

and results in a linear mapping of $\vec{q}$ onto the detector plane as shown in Fig. B.2. On the other hand, if high NA data is collected, then the mapping is linear in $sin\theta$ (Eq. B.2) as shown in Fig. B.3.

In order to remap the diffraction pattern into linear frequency, $\vec{q}$ is written in detector Cartesian coordinates.

$$\vec{q} = k_0 \left[\frac{x}{\sqrt{x^2 + y^2 + R^2}}\hat{x} + \frac{y}{\sqrt{x^2 + y^2 + R^2}}\hat{y} + \left(\frac{R}{\sqrt{x^2 + y^2 + R^2}} - 1 \right)\hat{z} \right] \tag{B.4}$$

With this equation, the non-linear mapping can be reversed using an interpolation routine.

In addition to the interpolation, the radiation at the edges of the Ewald sphere have propogated further than the radiation at the center. The intensity of the diffracted light on the dector should be corrected as follows:

$$I_{scaled}(x, y, z) = \left(1 + \frac{x^2 + y^2}{R^2}\right) I_0(x, y, z) \tag{B.5}$$

where I_0 is the raw recorded diffraction pattern.

B.3   Tilted Plane Correction

Thus far we have considered a sample plane parallel to the detector. For reflection geometry imaging, unless the detector has a hole in it, the sample plane will be at some non-zero angle. To describe the tilted sample, a rotation matrix is applied to $\vec{q}$. In our experiment, the sample is rotated about the y-axis, so the following rotation matrix is used,

$$R_y(\alpha) = \begin{bmatrix} -\cos\alpha & 0 & sin\alpha \\ 0 & -1 & 0 \\ -\sin\alpha & 0 & -\cos\alpha \end{bmatrix} \tag{B.6}$$

where α is the angle of rotation as depicted in Fig. B.1b. The rotated sample plane now lies in the (x'', y, z'') plane. The application of the rotation matrix to $\vec{q}$ yields

$$\vec{q}(x'', y, z'') = R_y(\alpha)\vec{q}(x, y, z) \tag{B.7}$$

$$\vec{q}(x'', y, z'') = (-q_x \cos\alpha + q_z \sin\alpha)\hat{x} - q_y\hat{y} - (q_x \sin\alpha + q_z \cos\alpha)\hat{z}. \tag{B.8}$$

This results in a non-linear and asymmetrical mapping of the diffraction pattern onto the detector plane as depicted in Fig. B.4. Again, using an interpolation routine, this non-linear mapping can be re-sampled onto a linearly spaced gird.
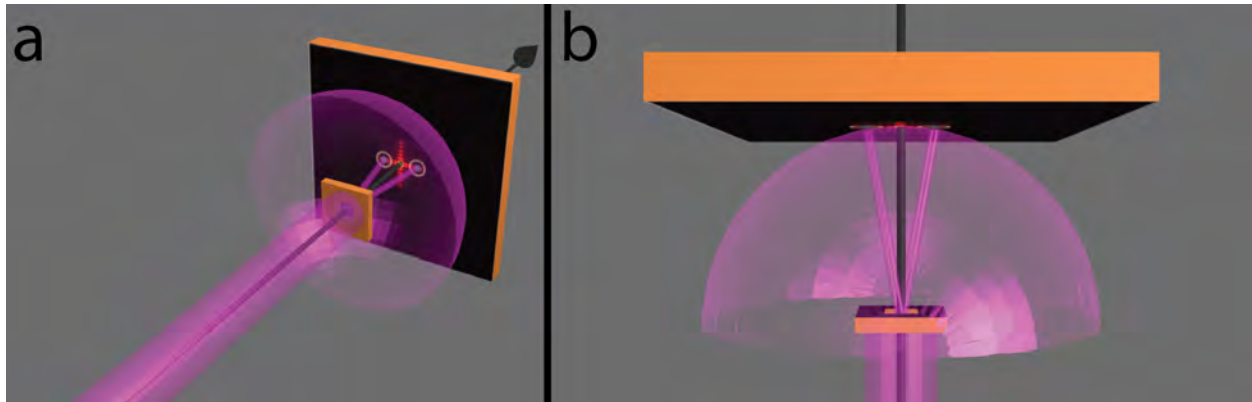
Figure B.2: **Low NA with Normal Incidence** a) Side-view. The circles on the detector highlight the same spatial frequency. b) Bird's eye view.)
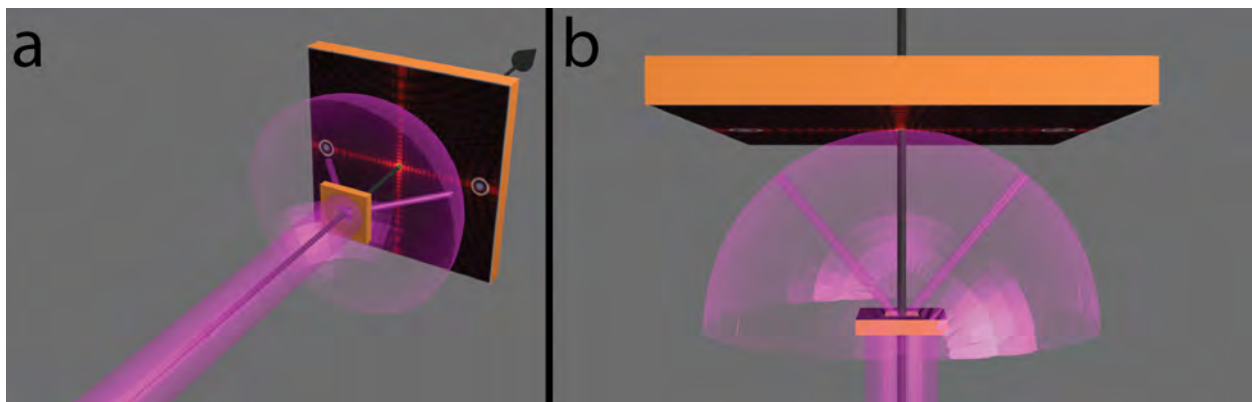

Figure B.3: **High NA with Normal Incidence** a) Side-view. The circles on the detector highlight the same spatial frequency. b) Bird's eye view.)
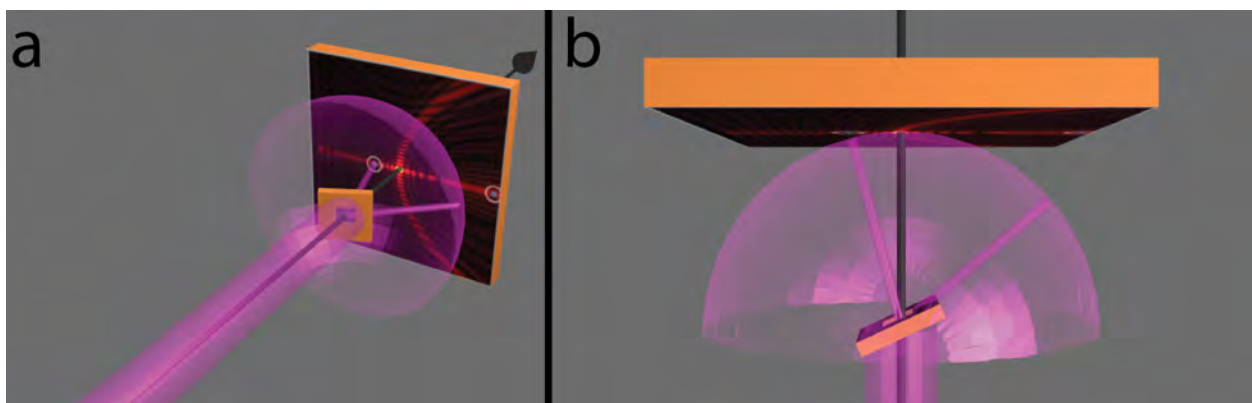

Figure B.4: **High NA with Non-Normal Incidence** a) Side-view. The circles on the detector highlight the same spatial frequency. b) Bird's eye view.)

Appendix C

Near-Wavelength Resolution CDI in Reflection with EUV: supplemental figures
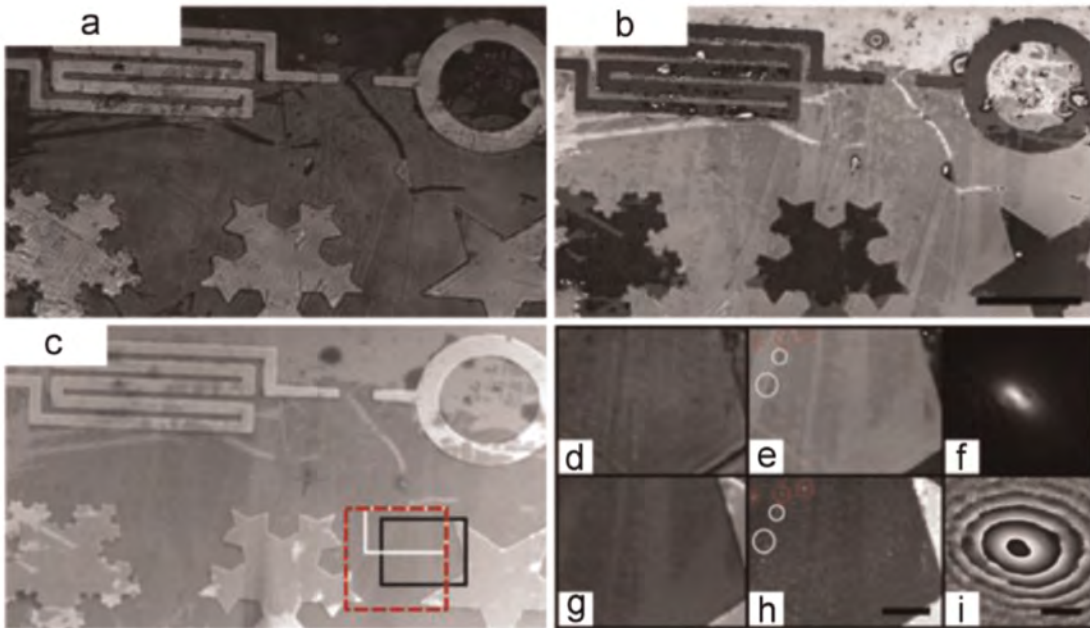
Figure C.1: **Full-Field, high-contrast, ptychographic imaging with high-harmonic generation** a) Amplitude and b) phase reconstructions using ptychography. c) An SEM image for comparison. A zoom-in of the d) amplitude and e) phase of ptychographic reconstruction. The zoom-in area is enclosed by the black rectangle in (c). g) The corresponding SEM zoom-in. h) AFM image in the same zoom-in region. The retrieved f) amplitude and i) phase of the probe. The white circles highlight dust contamination. The dashed rectangle is the area used for the calculation of the Modulation Transfer Function. The area enclosed by the white rectangle is used in the AFM comparison. The scale bar in (b) and (i) corresponds to 10 μm. The scale bar in (h) corresponds to 1 μm. Figure adapted from Zhang, Gardner et al. [168].
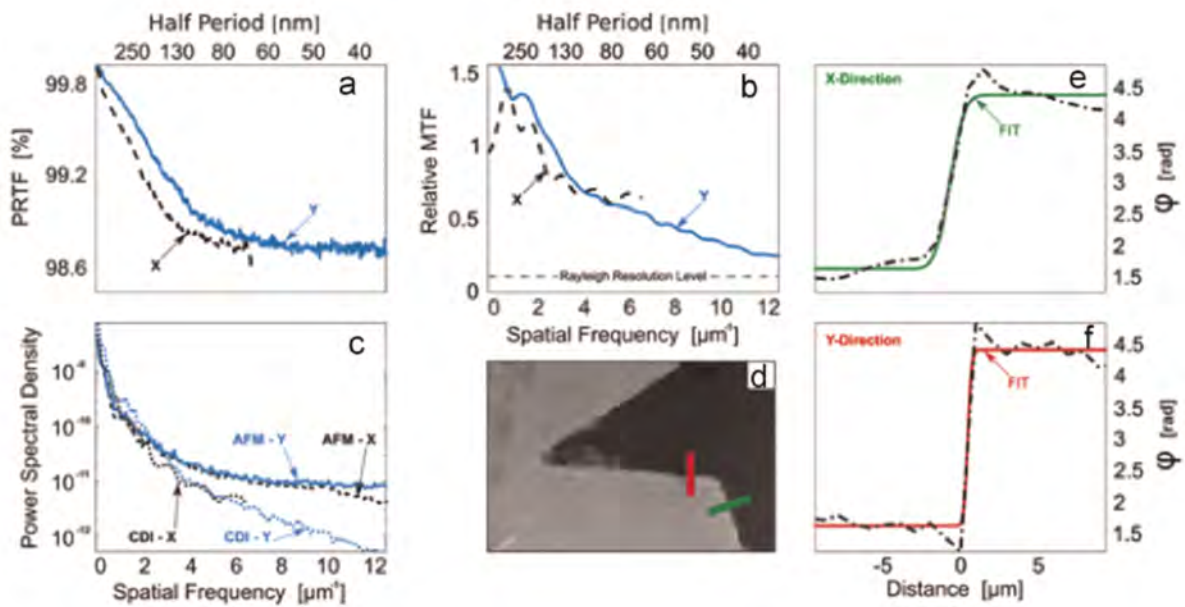
Figure C.2:   **Later Resolution Characterization** a) Phase retrieval transfer function. b) Relative modulation transfer function with an AFM image as the "true image. c) Power spectral densities of the CDI and AFM image, as labeled. d) The location of the knife-edge tests shown in (e) and (f). The profile across the e) x-direction and f) y-direction (dashed lines). An error-function is fitted to the profiles with R^2 better than 0.99 (solid lines). Figure adapted from Zhang, Gardner et al. [168].
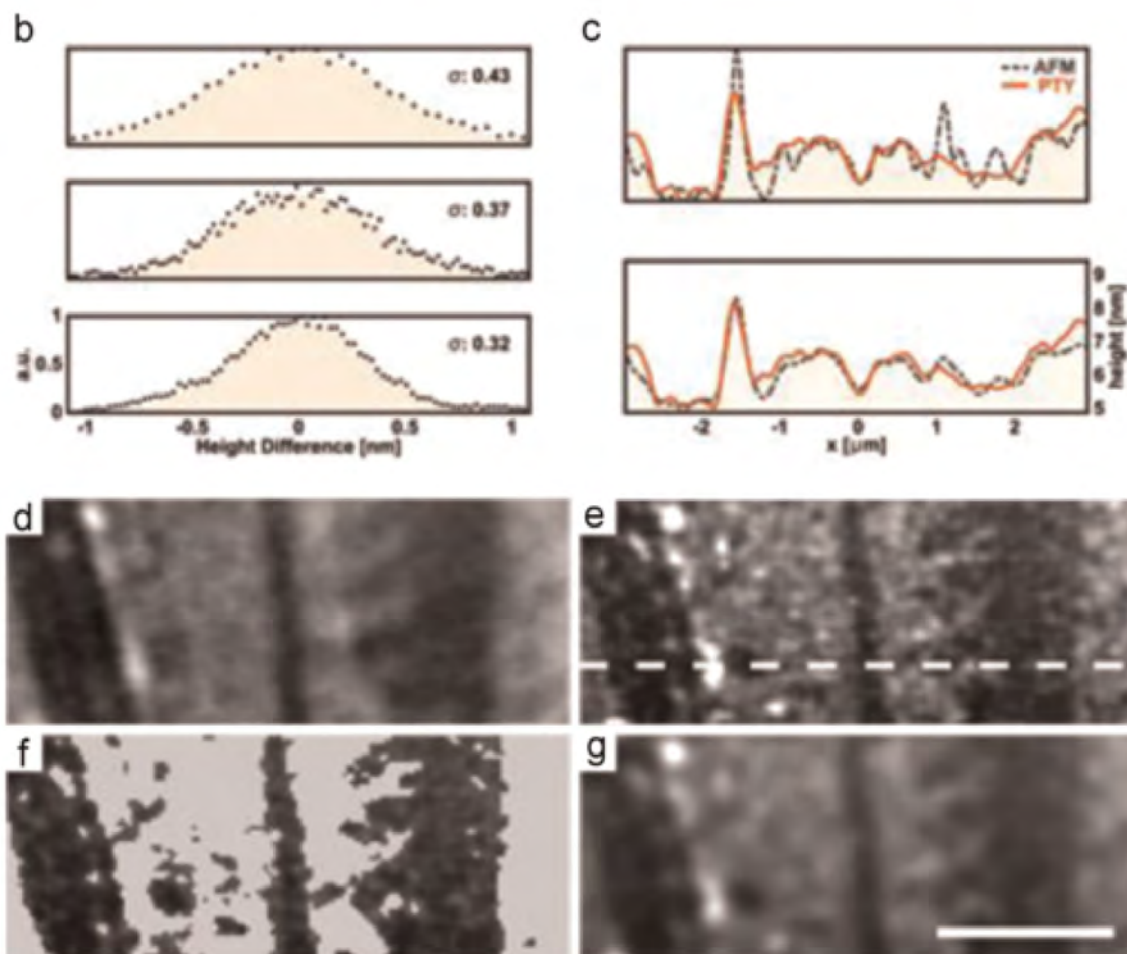
Figure C.3: **Axial Resolution Characterization** a) Histogram distributions of the height differences between the calculated height using the phase reconstruction and an AFM image. The top panel, no filtering and compares (c) and (d) directly. Middle panel only compares trench features, (c) and (e). The bottom panel compares a smoothed version of the AFM image, (c) and (f). (b) Comparative profiles taken along the white dashed line in (d). The top panel is no filtering, (c) and (d), and the bottom panel compares (c) and (f). (c) The calculated height from the ptychographic phase reconstruction. (d) The AFM image. (e) Only the trench features of the AFM image. (f) A Gaussian blurred image of the AFM to match the resolution of the CDI reconstruction. The scale bar in (f) corresponds to 2 μm and is shared with (c) (e). Figure adapted from Zhang, Gardner et al. [168].

Appendix D

Sub-wavelength coherent imaging of periodic samples: supplemental figures

D.1   Full ptychographic reconstruction of the zone plate sample

The full ptychographic reconstruction, covering an area of 11.3 μm × 11.3 μm, is shown in Fig. D.1. Only the reconstruction using the novel MEP constraint is shown. Degraded zone plate features are seen in the upper right quadrant, but this is not an artifact of the reconstruction because the same degradation is seen in the scanning electron microscope image in the inset of Fig. 8.1.
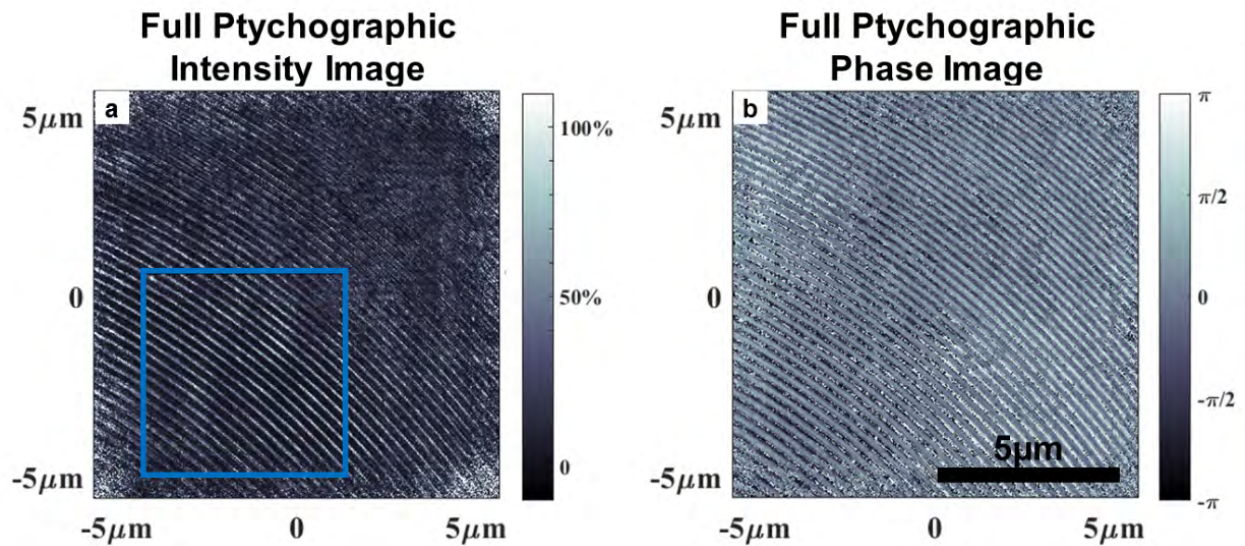

Figure D.1: **Full ptychographic image of the zone plate sample with MEP** The full, complex, ptychographic image of the zone plate sample, with MEP, where a) is the intensity and b) is the phase. The area highlighted by the blue box in (a) is the region shown in Fig. 8.3 and Fig. D.2. The 5μm scale bar in (b) is shared with (a).

D.2   Phase images with and without the MEP constraint

Phase images, corresponding to the intensity images shown in Figs. 8.3b,c, are displayed in Fig. D.2. The phase image without the MEP constraint, Fig. D.2b, suffers from artifacts such as ringing and striping compared to the MEP reconstruction, shown in Fig. D.2a, where the phase of the PMMA is smooth and continuous. In between the PMMA features, there are discontinues in the phase image corresponding phase wrapping.
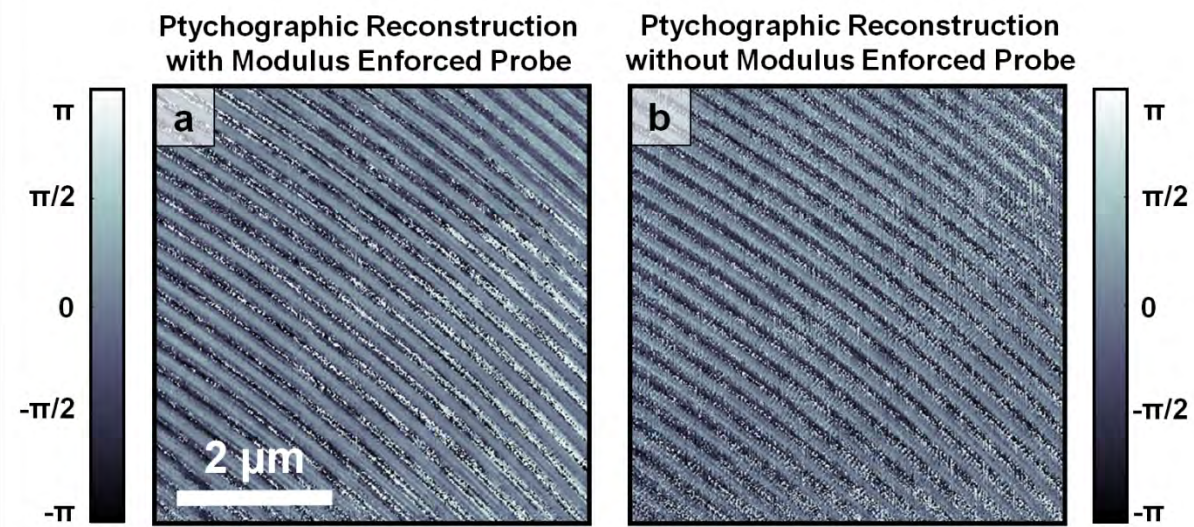

Figure D.2: **Phase images of the zone plate sample** Phase images of the zone plate sample (a) with the MEP constraint and b) without MEP. The 2μm scale bar in (a) is shared with (b).

D.3   Random Initial Probe Guess Simulations

As long as the diffraction patterns are properly sampled, no information about the probe is needed for the MEP algorithm to converge. On the other hand, without the MEP constraint, the algorithm will not converge using random probe guesses.
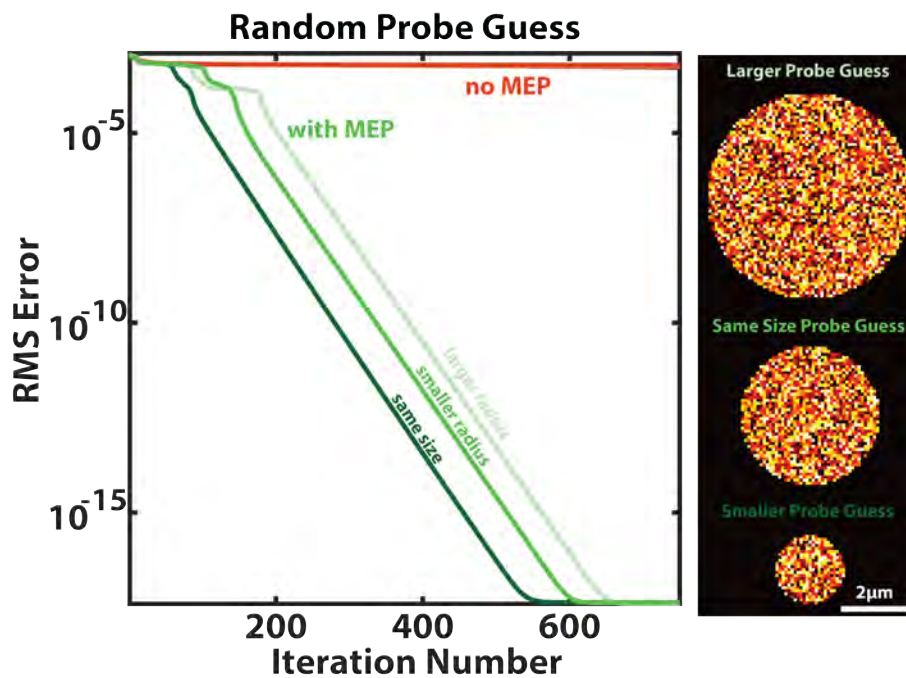

Figure D.3: **Random Initial Probe Guess Simulation Results** The MEP constrained ptychography algorithm is able to converge with random probe guesses. Without the constraint, the algorithm did not converge.

D.4   White Gaussian Noise Simulations

Additive white Gaussian noise is added to the data at 100 dB signal-to-noise (SNR) and 50 dB SNR. The ptychography algorithm with the MEP constraint converges to a lower root-mean-square (RMS) error in both cases.
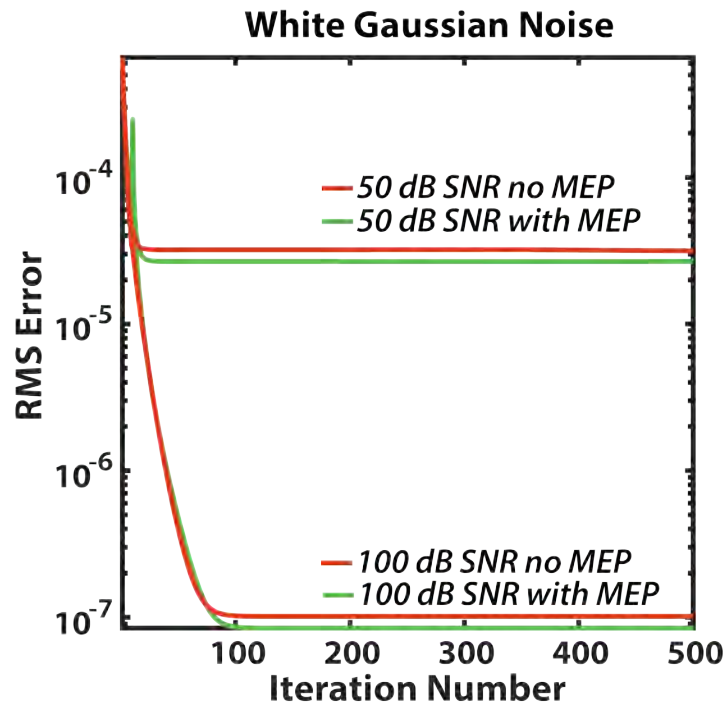

Figure D.4: **White Gaussian Noise Simulations** The MEP constrained ptychography algorithm reaches a lower error than the unconstrained algorithm